UNIVERSITÄT BONN
Physikalisches Institut

**Higgs production in Vector Boson Fusion
in the H → ττ → ℓℓ + 4ν final state
with ATLAS: a sensitivity study**

von
Martin Schmitz

A study of the expected sensitivity of the ATLAS experiment to discover the Standard Model Higgs boson produced via vector boson fusion (VBF) and its decay to $H \to \tau\tau \to \ell\ell + 4\nu$ is presented. The study is based on simulated proton-proton collisions at a centre-of-mass energy of 14 TeV. For the first time the discovery potential is evaluated in the presence of additional proton-proton interactions (pile-up) to the process of interest in a complete and consistent way. Special emphasis is placed on the development of background estimation techniques to extract the main background processes $Z \to \tau\tau$ and $t\bar{t}$ production using data. The $t\bar{t}$ background is estimated using a control sample selected with the VBF analysis cuts and the inverted b-jet veto. The dominant background process $Z \to \tau\tau$ is estimated using $Z \to \mu\mu$ events. Replacing the muons of the $Z \to \mu\mu$ event with simulated τ-leptons, $Z \to \tau\tau$ events are modelled to high precision. For the replacement of the Z boson decay products a dedicated method based on tracks and calorimeter cells is developed. Without pile-up a discovery potential of 3σ to 3.4σ in the mass range $115\,\mathrm{GeV} < M_H < 130\,\mathrm{GeV}$ is obtained assuming an integrated luminosity of $30\,\mathrm{fb}^{-1}$. In the presence of pile-up the signal sensitivity decreases to 1.7σ to 1.9σ mainly caused by the worse resolution of the reconstructed missing transverse energy.

Angefertigt mit Genehmigung der Mathematisch-Naturwissenschaftlichen Fakultät der Rheinischen Friedrich-Wilhelms-Universität Bonn

Contents

Chapter 1

Introduction

The Standard Model of Particle Physics describes phenomena and interactions at the elementary particle level to high precision. Throughout the last decades it has been subjected to validation and tests which, although it may not be the final theory, it has mastered with great success.

Despite its success several questions are still unanswered. One of the most important fundamental questions is the explanation of massive elementary particles. Probably the most favoured solution is the Higgs mechanism to explain the electro-weak symmetry breaking. The existence of a neutral scalar particle, called the Higgs boson, is connected to this mechanism. Up to now the existence of the Higgs boson could not be proved by experiments. Direct searches at the LEP[1] and TEVATRON[2] experiments exclude a Higgs boson with a mass lighter than 114.4 GeV and also one with a mass in the range $158\,\text{GeV} < M_H < 175\,\text{GeV}$. However, high precision measurements of the Standard Model parameters favour a light Higgs boson ($M_H < 186\,\text{GeV}$) within the model.

With a centre-of-mass energy of up to 14 TeV the Large Hadron Collider (LHC) provides the possibility to reveal the existence of the Higgs boson for its entire allowed mass range. As earlier studies [1] show, the production of a Higgs boson via vector boson fusion (VBF) and its subsequent decay into a pair of τ-leptons is one of the most promising processes for a discovery of a light Higgs boson. In vector boson fusion the Higgs boson is accompanied by two jets, which have a large separation in pseudo-rapidity. Predominantly at least one of the jets is found in the forward region of the detector. Between these jets the production of additional jets is suppressed. This typical signature of jets in the VBF process provides a good discrimination against background processes.

In this thesis the potential of the ATLAS detector at the LHC to discover a Standard Model Higgs boson in the channel VBF $H \to \tau\tau$ with a subsequent decay of the τ-leptons into leptons is studied using Monte Carlo simulated events. The proton-proton collisions are simulated at a centre-of-mass energy of 14 TeV. Despite the small branching ratio the di-lepton channel, that means the decay $H \to \tau\tau \to \ell\ell + 4\nu$, provides a high signal sensitivity due to excellent trigger conditions and lepton reconstruction efficiencies.

---

[1]The Large Electron Positron Collider operated from 1989 till 2000 and provided electron-positron collisions up to a centre-of-mass energy of 209 GeV.

[2]TEVATRON is a proton-antiproton collider operating at a centre-of-mass energy of 1.96 TeV.

The luminosity provided by the LHC involves several proton-proton interactions per bunch crossing. These additional proton-proton interactions are often referred to as pile-up and might have a large influence on the event reconstruction. The effects of pile-up have often been neglected or are only partially considered in earlier studies. This thesis presents the first study of the VBF $H \to \tau\tau \to \ell\ell + 4\nu$ process considering pile-up in both the signal and background processes at the ATLAS experiment. Although in the current LHC schedule no collisions at a centre-of-mass energy of $14 \, \text{TeV}$ are planned for the next two years, the presented study gives important information for the preparation of the search strategies, which are defined now.

In order to discover the Higgs boson a precise knowledge of the background processes is crucial. Typically the background is estimated using Monte Carlo simulated events. The background estimation using Monte Carlo simulated events needs some validation and, due to miss-modelling, is often guided by large systematic uncertainties. In particular the special signature of jets in the signal process requires a precise knowledge and modelling of the jet kinematics of the background processes. This is difficult using exclusively Monte Carlo simulation and thus background estimation methods relying on collision data are preferred. In this thesis methods to estimate the main background processes using data are developed. They rely on the selection of control samples of high purity giving a precise description of the background processes.

Chapter 2

Theoretical Overview

Interactions and processes at the elementary-particle level are described to high precision using a theory called Standard Model [2–4]. It is based on a local gauge symmetry which describes three of the four fundamental interactions: electro-magenetic, weak and strong interactions. Gravity is not included in the Standard Model, because it is too weak at the energy scales reachable at present particle colliders. In order to allow the description of massive elementary particles the gauge symmetry is spontaneously broken. This implies the existence of a new particle, the so called Higgs boson. Up to now, direct searches have not proven that this particle exists.

This chapter presents a short review of the Standard Model and the Higgs Mechanism. It is based on [5] and [6].

2.1   The Standard Model

According to the Standard Model the world consists of different sorts of elementary point-like particles. Elementary particles with half-integer spin are called fermions. They are classified into quarks and leptons and are ordered in three generations:

$$
\begin{array}{ccc}
 & \text{Leptons} & \text{Quarks} \\[4pt]
\text{1. Generation:} & \left(\begin{array}{c} \nu_e \\ e^- \end{array} \right)_L, \, e_R^-, & \left(\begin{array}{c} u \\ d \end{array} \right)_L, \, u_R, \, d_R \\[12pt]
\text{2. Generation:} & \left(\begin{array}{c} \nu_\mu \\ \mu^- \end{array} \right)_L, \, \mu_R^-, & \left(\begin{array}{c} c \\ s \end{array} \right)_L, \, c_R, \, s_R \\[12pt]
\text{3. Generation:} & \left(\begin{array}{c} \nu_\tau \\ \tau^- \end{array} \right)_L, \, \tau_R^-, & \left(\begin{array}{c} b \\ t \end{array} \right)_L, \, t_R, \, b_R
\end{array}
$$

L (R) denotes left-handed (right-handed) fermions. The particles in the second and third generation are a copy of the particles in the first one with identical properties, differing only in their masses. In addition to each particle a corresponding anti-particle exits. Interactions between the fermions are mediated by integer spin particles called gauge bosons. The mass and electrical charge of the fundamental fermions and gauge bosons are listed in Table 2.1.

The strong interaction is described by the $SU(3)_C$ symmetry group. It is mediated by eight massless gauge boson called gluons. The C represents colour, which is the charge of the strong interaction. Three different types of colour charge exists, which are commonly called red, green and blue. Only quarks and gluons carry colour charge and take part in the strong interaction. The experimentally observed matter particles build up by quarks are called hadrons and are colourless.

The description of the electro-weak interaction is represented by the $SU(2)_L \otimes U(1)_Y$ symmetry group. The generator of the group $U(1)_Y$ is the hypercharge Y, the corresponding gauge field is B_μ. The group $SU(2)_L$ represents the weak isospin with corresponding gauge fields $W_\mu^{1,2,3}$. Its generators T_a are proportional to the 2×2 Pauli matrices and are given by $T_a = \frac{1}{2}\sigma_a$. The subscript L of the weak isospin group refers to its the left-handed character. In particular, left-handed Fermions form an isospin doublet, whereas the right-handed Fermions are isospin singlets. The hypercharge and the weak isospin are associated to the electro-magnetic charge Q,

$$Q = \frac{Y}{2} + I_3 \ .$$

The charged gauge bosons $W_\mu^\pm$ are obtained from the fields $W_\mu^{1,2}$ by

$$W_\mu^\pm = \frac{1}{\sqrt{2}} \left(W_\mu^1 \mp W_\mu^2 \right) \ .$$

Since the $W^\pm$ bosons are purely a combination of the weak isospin field, they only interact with left-handed fermions (or right-handed anti-fermions). The neutral gauge boson Z and the photon are derived from a combination of the fields W_μ^3 and B_μ:

$$\begin{pmatrix} A_\mu \\ Z_\mu \end{pmatrix} = \begin{pmatrix} \cos\theta_w & \sin\theta_w \\ -\sin\theta_w & \cos\theta_w \end{pmatrix} \begin{pmatrix} B_\mu \\ W_\mu \end{pmatrix} \ .$$

The Weinberg angle θ_w defines the rotation in the neutral sector. θ_w can be expressed using the $SU(2)_L$ and $U(1)_Y$ coupling constants g and g' according to $\cos\theta_w = \frac{g}{\sqrt{g^2 + g'^2}}$.

The interactions in the electro-weak sector are described by the Lagrangian

$$\begin{aligned} \mathcal{L} = &- \frac{1}{4}\vec{W}_{\mu\nu}\vec{W}^{\mu\nu} - \frac{1}{4}B_{\mu\nu}B^{\mu\nu} \\ &+ \bar{L}\gamma^\mu \left[i\partial_\mu - g\vec{T} \cdot \vec{W}_\mu - g'\frac{Y}{2}B_\mu \right] L \\ &+ \bar{R}\gamma^\mu \left[i\partial_\mu - g'\frac{Y}{2}B_\mu \right] R \ . \end{aligned}$$

L denotes a left-handed fermion isospin doublet, R the corresponding right-handed isospin singlet. $\vec{T}$ and $\vec{W}_\mu$ are triplets in SU(2) space and represent the three generators T_a and the three fields $W_\mu^{1,2,3}$ respectively. The last two lines represent the fermion Lagrangian, which describes the kinetic energy of the fermions and their interactions with the $W^\pm$, Z and the photon. The terms in the first line describes the kinetic energy and interactions of the gauge fields. The field-strength tensors are:

$$\begin{aligned} B_{\mu\nu} &= \partial_\mu B_\nu - \partial_\nu B_\mu \\ \vec{W}_{\mu\nu} &= \partial_\mu \vec{W}_\nu - \partial_\nu \vec{W}_\mu + g\vec{W}_\mu \times \vec{W}_\nu \end{aligned}$$

Particle		Electric charge [e]	Mass
ν_e	electron-neutrino	0	$< 2\,\text{MeV}$
e	electron	-1	$0.511\,\text{MeV}$
u	up quark	$\frac{+2}{3}$	$1.7 - 3.3\,\text{MeV}$
d	down quark	$\frac{-1}{3}$	$4.1 - 5.8\,\text{MeV}$
ν_μ	muon-neutrino	0	$< 0.19\,\text{MeV}$
μ	muon	-1	$106\,\text{MeV}$
c	charm quark	$\frac{+2}{3}$	$1.27\,\text{GeV}$
s	strange quark	$\frac{-1}{3}$	$101\,\text{MeV}$
ν_τ	tau-neutrino	0	$< 18.2\,\text{MeV}$
τ	tau	-1	$1.777\,\text{GeV}$
t	top quark	$\frac{+2}{3}$	$172\,\text{GeV}$
b	bottom quark	$\frac{-1}{3}$	$4.2\,\text{GeV}$
γ	photon	0	$0\,\text{eV}$
g	gluon	0	$0\,\text{eV}$
$W^\pm$	W boson	± 1	$80.4\,\text{GeV}$
Z	Z boson	0	$91.2\,\text{GeV}$

Table 2.1: *Masses and electric charge of the fundamental fermions and bosons [9].*

The Lagrangian is invariant under local gauge transformations. The gauge invariance ensures, under certain conditions, that the theory is renormalisable [7,8]. Renormalisation allows to absorb divergencies, which occur in higher order calculations with bosonic or fermionic loops, using a redefinition of physical quantities like charge and mass. The ability of the Standard Model being renormalisable guarantees its predictive power and allows the accurate calculation of physical quantities.

In order to not spoil the local gauge invariance of the Lagrangian the fermions and gauge boson have to be massless, which is in contradiction to experimental observations.

2.2 Spontaneous Symmetry Breaking and the Higgs Mechanism

To overcome the restriction of the Standard Model to massless particles the Higgs mechanism [10–12] is employed which utilises the concept of spontaneous symmetry breaking. The spontaneous symmetry breaking of a global symmetry results in the appearance of massless spinless particles, the so called Goldstone bosons [13,14]. If a local gauge symmetry is spontaneously broken the degrees of freedom of the Goldstone bosons are transformed to a longitudinal degree of freedom of the massless gauge bosons. That means the gauge bosons become massive. The number of vector bosons that acquire mass is exactly equal to the number of Goldstone bosons.

In contrast to the $W^\pm$ and the Z boson, the photon is required to be massless. Considering this, the spontaneous symmetry breaking pattern in the electro-weak sector must be: $SU(2)_L \otimes U(1)_Y \rightarrow U(1)_{em}$. The simplest way of providing this condition is adding to
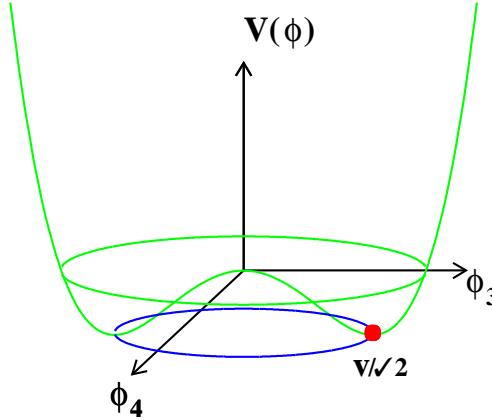
Figure 2.1: *Sketch of the Higgs potential as a function of two out of four components.*

the Lagrangian $\mathcal{L}$ the term

$$\mathcal{L}_{Higgs} = (D_\mu \Phi)^\dagger (D^\mu \Phi) - V(\Phi) \ . \tag{2.1}$$

D_μ denotes the covariante derivative

$$D_\mu = \partial_\mu - ig\vec{T} \cdot \vec{W}_\mu - \frac{1}{2} ig' Y B_\mu \ , \tag{2.2}$$

and $V(\Phi)$ is the Higgs potential

$$V(\Phi) = \mu^2 \Phi^\dagger \Phi + \lambda (\Phi^\dagger \Phi)^2 \ , \ \mu^2 < 0 \ . \tag{2.3}$$

To break the $SU(2)_L \times U(1)_Y$ symmetry the choice of Φ must have a non-vanishing hypercharge and weak isospin. To make the $W^\pm$ and Z gauge bosons massive at least three Goldstone bosons are needed. The simplest choice is

$$\Phi = \begin{pmatrix} \Phi^+ \\ \Phi^0 \end{pmatrix} = \frac{1}{\sqrt{2}} \begin{pmatrix} \Phi_1 + i\Phi_2 \\ \Phi_3 + i\Phi_4 \end{pmatrix} \ , \ \Phi_i \text{ are real fields.} \tag{2.4}$$

The hypercharge of Φ is $Y = 1$ and its weak isospin is $I = \frac{1}{2}$. To restrict the potential $V(\Phi)$ to a lower bound the parameter λ needs to be larger than zero. By choosing $\mu^2 < 0$ an infinite number of minima of the potential $V(\Phi)$ exist.

$$\Phi^\dagger \Phi = \frac{1}{2} \left(\Phi_1^2 + \Phi_2^2 + \Phi_3^2 + \Phi_4^2 \right) = -\frac{\mu^2}{2\lambda} \ . \tag{2.5}$$

A sketch of the Higgs potential is shown in Figure 2.1. For a better illustration the Higgs potential is shown as a function of two out of four components. These minima correspond to an infinite no. of degenerate vacua. The breaking of the $SU(2)_L \times U(1)_Y$ symmetry occurs once a particular minimum is chosen. As usual the simplest choice is taken:

$$\Phi_1 = \Phi_2 = \Phi_4 = 0 \ , \qquad \Phi_3^2 = -\frac{\mu^2}{\lambda} \equiv v^2 \ .$$

This choice also guarantees that the $U(1)_{em}$ remains unbroken and hence the photon is massless.

To build the physical spectra small fluctuations around the minima are performed. They can be described using the parametrisation:

$$\Phi_{vac}(x) = e^{i\vec{\sigma}\cdot\vec{\theta}(x)/v} \begin{pmatrix} 0 \\ \frac{v+h(x)}{\sqrt{2}} \end{pmatrix} \ . \tag{2.6}$$

The three fields θ_1, θ_2 and θ_3, written as $\vec{\theta}$ are unphysical. To eliminate them the gauge transformation $\Phi \to e^{-i\vec{\sigma}\cdot\vec{\theta}(x)/v}\Phi$, which is often called unitary gauge, is applied. The field h in contrast corresponds to a physical scalar boson. By using equations (2.6) and (2.1) mass terms show up in the Lagrangian, which can be identified as the masses of the gauge bosons:

$$M_W \quad = \tfrac{1}{2}vg \tag{2.7}$$

$$M_Z \quad = \tfrac{1}{2}v\sqrt{g^2 + g'^2} \tag{2.8}$$

$$M_A \quad = 0 \tag{2.9}$$

$$M_H \quad = v\sqrt{2\lambda} \quad . \tag{2.10}$$

The strength of the weak interaction at low energies is effectively given by the Fermi constant G_F. This is connected to the vacuum expectation value v by

$$\frac{G_F}{\sqrt{2}} = \frac{g^2}{8M_W 2} = \frac{1}{2v^2} \ .$$

And therefore

$$v = \frac{1}{\sqrt{G_F\sqrt{2}}} = \frac{2M_W}{g} \simeq 246 \text{ GeV.}$$

The occurrence of the physical scalar boson can be explained by looking at the number of degrees of freedom (d.o.f.). Four d.o.f. are added by introducing the field Φ. Due to the symmetry breaking three of them are absorbed to get $W^{\pm}$, Z Bosons massive. The remaining d.o.f. forms a scalar boson, which is called the Higgs boson.

As for the gauge bosons the local gauge symmetry forbids explicit mass terms for fermions. To account for the masses of the fermions the same doublet Φ is sufficient. Therefore a Yukawa Lagrangian is needed:

$$\mathcal{L}_{Yukawa} = \lambda_e \bar{L}\Phi e_R + \lambda_d \bar{q}_L \Phi d_R + \lambda_u \bar{q}_L \tilde{\Phi} u_R + h.c.$$
$$+ \text{ second and third family.} \tag{2.11}$$

Here $L = \begin{pmatrix} \nu_e \\ e^- \end{pmatrix}_L$, $q_L = \begin{pmatrix} u \\ d \end{pmatrix}_L$ and $\tilde{\Phi} = i\sigma_2\phi^*$. The λ_f are called Yukawa couplings. The masses of the leptons are then given by:

$$M_f = v\frac{\lambda_f}{\sqrt{2}} \ .$$

Since the masses of the fermions are well measured the couplings depending on the Higgs boson mass M_H can be determined. The coupling of the Higgs boson to fermions and gauge boson is

$$g_{Hf\bar{f}} = \frac{gM_f}{2M_W} \ ; \quad g_{HW^+W^-} = gM_W \ ; \quad g_{HZZ} = \frac{g}{\cos\theta_w}M_Z \ . \tag{2.12}$$

The Higgs mechanism provides a method to introduce mass terms in the Standard Model Lagrangian while conserving the local gauge symmetry and the renormalisability of the theory. The only unknown parameter is the mass of the Higgs boson.

2.3 Bounds on the Higgs Boson Mass

2.3.1 Theoretical Bounds

Although the mass of the Higgs boson is an unknown parameter in the Standard Model, theoretical considerations and the requirement of consistency lead to constraints on M_H. A comprehensive summary can be found in [15].

The cross section for elastic scattering of longitudinally polarised W bosons, $W_L^- W_L^+ \to W_L^- W_L^+$, is divergent at high energies and leads to a violation of unitarity at an energy scale of $1 - 2\,\mathrm{TeV}$. By introducing a scalar particle like the Higgs boson the divergency cancels and unitarity is restored. From this requirement the Higgs boson mass is limited to $M_H \lesssim 1\,\mathrm{TeV}$ [16].

Further constraints on M_H can be derived from the energy scale Λ up to which the Standard Model is assumed to be valid. The coupling λ of the Higgs self-interaction is energy dependent due to quantum fluctuations. The Feynman graphs with the dominant contributions are shown in Fig. 2.2. Neglecting the top quark loop the renormalised coupling at one-loop level is given by

$$\lambda_R(Q^2) = \frac{\lambda_R(v^2)}{1 - \frac{3}{4\pi^2}\lambda(v^2)\log\frac{Q^2}{v^2}} \ . \tag{2.13}$$

For large energies, $Q^2 >> v^2$, the quartic coupling becomes infinite at the so called Landau pole. Requiring $\lambda(\Lambda)$ to remain finite an upper bound on the M_H can be derived:

$$M_H \leq \frac{8\pi^2 v^2}{3\log\frac{\Lambda^2}{v^2}} \ . \tag{2.14}$$

A lower bound on M_H can be derived taking into account loop corrections on λ involving the top-quark. If the M_H is too small the top-quark loop corrections become dominant and lead to small or even negative values of λ. This means that the ground state of the Higgs potential would no longer be stable. To avoid this M_H must exceed a minimal value depending on the top-quark mass and the energy scale Λ up to which the Standard Model is assumed to be valid.

The lower and upper bounds on M_H depending on the energy scale Λ up to which the Standard Model is assumed to be valid are shown in Fig. 2.3. Assuming new physics appear at an energy scale $\Lambda = 1\,\mathrm{TeV}$ the mass of the Higgs boson is constrained to the range $55\,\mathrm{TeV} < M_H < 700\,\mathrm{GeV}$ [15]. If the Standard Model is valid up to the Planck scale, masses of the Higgs boson in the range $130\,\mathrm{TeV} < M_H < 190\,\mathrm{GeV}$ are allowed.

2.3.2 Experimental Bounds

Direct searches for the Higgs boson at particle colliders have been made in the last decades. The searches carried out at the LEP collider exclude a Higgs boson with a mass lower
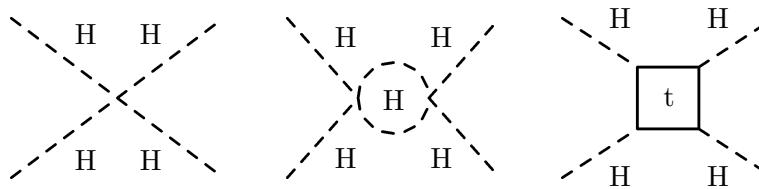
Figure 2.2: *Leading Feynman diagrams at tree and one-loop level for the Higgs self-coupling.*
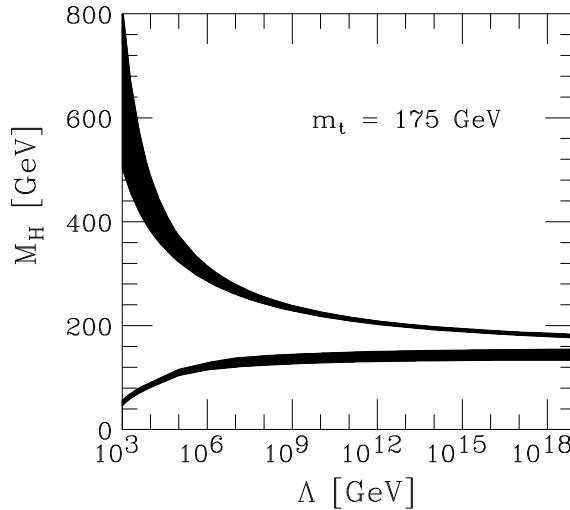

Figure 2.3: *Theoretical allowed region of M_H depending on the energy scale Λ up to which the Standard Model is assumed to be valid.*

than $M_H > 114.4$ GeV [17] with at least 95% confidence level. Direct searches at the TEVATRON experiments CDF [18] and D0 [19] excluded the mass range 158 GeV $< M_H < 175$ GeV [20] at 95% confidence level.

Indirect constraints on M_H are derived using high-precision measurements of Standard Model parameters. The Higgs boson is connected to these parameters via loop corrections. By fitting the precision measurements to their theoretical expectations constraints on the Higgs boson mass are obtained. In this context the mass of the top quark is important, since it contributes in quadrature to the calculation of M_H. As a result of the fit shown in Fig. 2.4 the Standard Model prefers a light Higgs boson. Considering theoretical uncertainties and including the limit of 114.4 GeV derived from LEP searches the mass of the Higgs boson is lower than 186 GeV at 95% confidence level [21].

2.4 Higgs Boson Production at the Large Hadron Collider

At the LHC a Standard Model Higgs boson is produced by four dominant production processes. Example Feynman graphs are shown in Fig. 2.6. The dependence of the production cross section on the mass of the Higgs boson is visualised in Fig. 2.6.

The dominant production process is the *gluon-gluon fusion* process $gg \to H$. The coupling of the gluons to the Higgs boson is mediated via a quark loop. The dominant contribution is provided by the top quark, since it is by far the heaviest and for this reason it has the
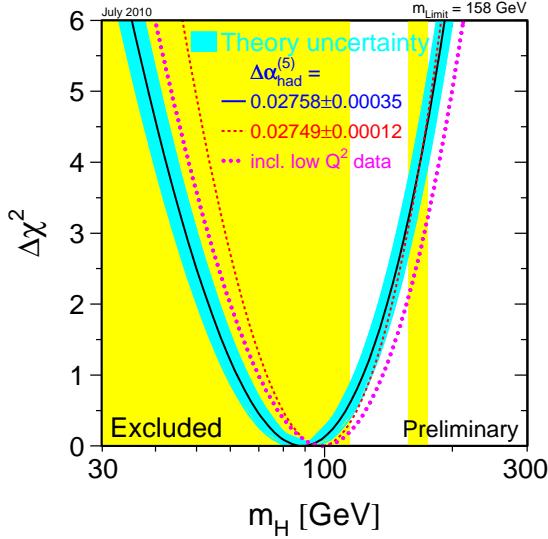
Figure 2.4: $\Delta\chi^2$ *distribution of a global fit of the Standard Model parameters depending on the assumed mass of the Higgs boson M_H [21]. The yellow shaded region is excluded by direct searches.*

strongest coupling to the Higgs boson among the fermions.

The production process with the second highest cross section is the *Vector Boson Fusion* (VBF) $qq \rightarrow qqH$. This production process is considered in this thesis. Each of the incoming partons radiates off a heavy vector boson W/Z. The vector bosons must have a minimum energy of $\mathcal{O}(\frac{1}{2}M_H)$ to produce the Higgs boson. The finale state quarks produce jets of which at least on is predominantly lying in the forward region of the detector. To be reconstructed as jets they need sufficient p_{T}. Since no colour charge is exchanged between the two quarks the production of additional jets is suppressed in the central detector region. This typical signature of jets in the VBF process differs from jet signatures in QCD processes and provides a good discrimination of background processes.

The remaining Higgs boson production processes, Higgsstrahlung and top quark associated production, have a significantly lower cross section. In the production through Higgsstrahlung the Higgs boson is radiated off a heavy vector boson W/Z. In the top quark associated production the Higgs boson is radiated off a pair of top quarks. Despite the small cross section of these two production processes recent studies show that they provide an important contribution to Higgs boson searches at low M_H using the decay $H \rightarrow b\bar{b}$.

2.5   Decay of the SM Higgs Boson

The couplings of the Higgs boson to gauge bosons and fermions are directly proportional to the masses of the particles. Therefore its decay to the heaviest particles is preferred if accessible by phase space. Fig. 2.7 shows the branching ratio depending on the mass of
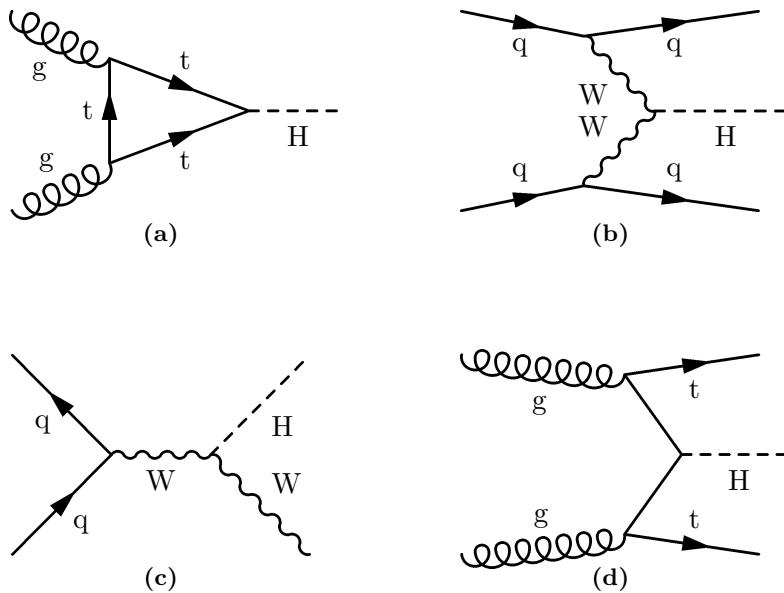
Figure 2.5: *Main production processes of a standard model Higgs boson at the LHC. a) gluon-gluon fusion, b) vector boson fusion, c) associated production with W/Z, d) associated production with top quark.*

the Higgs boson. At higher masses M_H the decay of the Higgs boson into vector bosons becomes dominant.

For a Higgs boson in the mass range $115\,\text{GeV} < M_H < 130\,\text{GeV}$, which is favoured by the Standard Model, the dominant decay channel is $H \to b\bar{b}$. Due to the large cross section of the QCD background processes at the Large Hadron Collider this decay channel is very difficult to handle. It has turned out that in this mass range the ATLAS experiment is sensitive to the decay $H \to \tau\tau$. Since the τ-lepton is not a stable particle the decay $H \to \tau\tau$ results in the final states:

- $H \to \tau\tau \to \ell\ell + 4\nu$ in 12.4%

- $H \to \tau\tau \to \ell h + 3\nu$ in 45.6%

- $H \to \tau\tau \to hh + 2\nu$ in 42%

h denotes a decay of the τ-lepton into hadrons, ℓ signifies the decay of the τ-lepton into a electron or muon. Because of the large cross section of the QCD background processes the decay channel $H \to \tau\tau \to hh + 2\nu$ is difficult to handle. Despite the smaller branching ratio compared to $H \to \tau\tau \to \ell h + 3\nu$, the decay channel $H \to \tau\tau \to \ell\ell + 4\nu$ has a clear signature of two leptons and a considerable amount of missing transverse energy due to the four neutrinos. This provides a large rejection factor for QCD background processes.
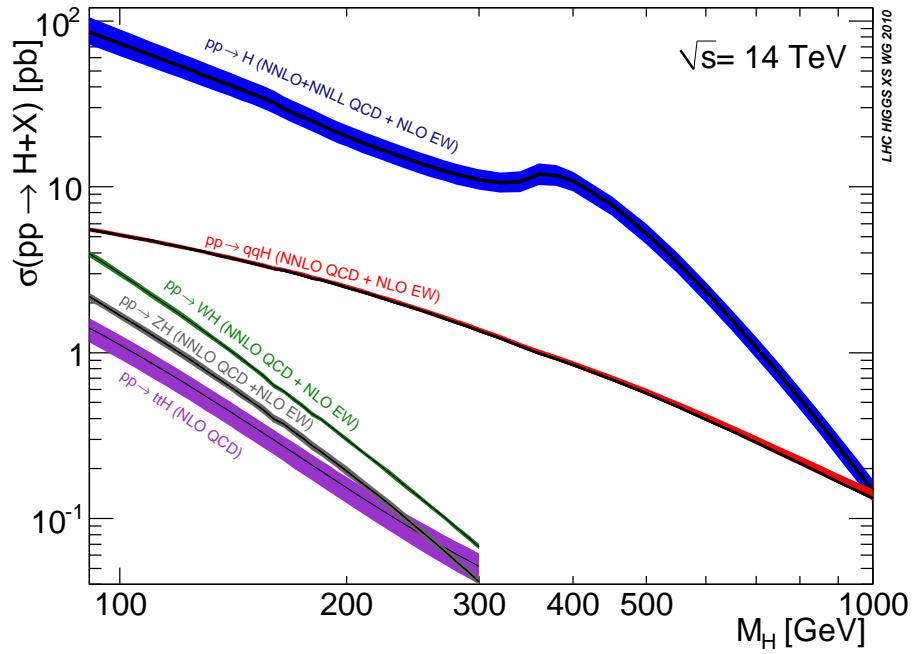
Figure 2.6: *Production cross section of a standard model Higgs boson depending on its assumed mass M_H [22].*
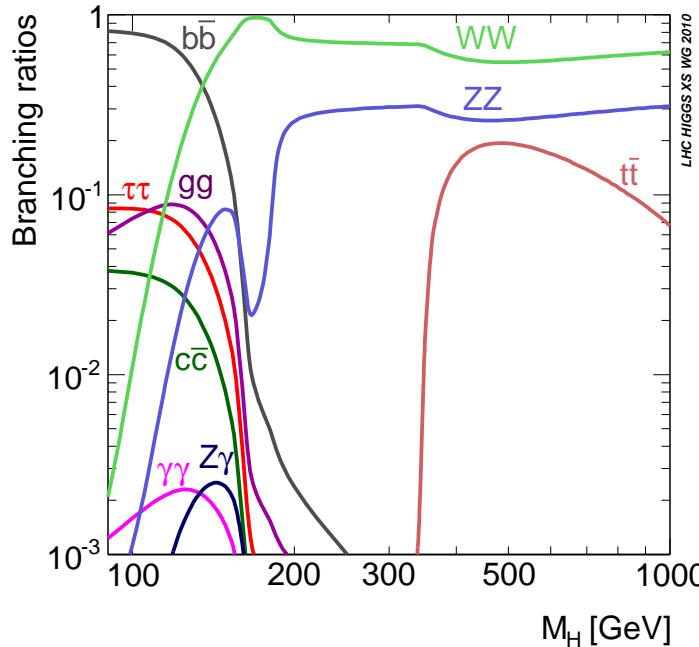

Figure 2.7: *Branching ratio of a standard model Higgs boson depending on its assumed mass M_H [22].*

Chapter 3

The LHC and the ATLAS Experiment

The chapter starts with a short introduction of the LHC. More details can be found in [23]. This is followed by a description of the ATLAS detector based on the detailed information in [24].

3.1 Large Hadron Collider

The Large Hadron Collider is a particle accelerator based at the European Centre for Particle Physics (CERN) near Geneva. The accelerator, arranged as a ring with a circumference of 27 km, is placed in the former tunnel of the LEP accelerator. The LHC has started operation in October 2008 and has been relaunched after a break for repairing in November 2009. It is currently operating at a centre-of-mass energy of 7 TeV and will stop for a shut down used for maintenance and upgrade at the end of 2012. The LHC is designed to accelerate protons (p) up to an energy of 7 TeV. Before injected into the LHC, the protons are accelerated to an energy of 450 GeV by a chain of accelerators: LINAC, BOOSTER, the Proton Synchrotron and the Super Proton Synchrotron. The protons are arranged in bunches each containing up to 10^{11} protons. The needed bending power to keep the proton beams on track are provided by 1232 dipole magnets with a maximal field strength of 8.33 T. To keep the beam diameter small 392 quadrupole magnets are used. The high field strength is provided by a superconducting magnet system operating at a temperature of 1.9 K. Once operating at the design parameters the proton bunches will collide every 25 ns at the interaction points and the LHC will provide a luminosity of $10^{34}\,\mathrm{cm}^{-2}\mathrm{s}^{-1}$. At this luminosity in average 23 proton collisions per bunch crossing are expected.
The LHC is also able to collide heavy ions. In November 2010 the first collisions of lead nuclei took place.
At four interaction points the experiments ALICE [25], ATLAS [26], CMS [27] and LHCb [28] are located. ATLAS and CMS are multi-purpose detectors designed to cover a wide range of Physics. ALICE studies heavy ion physics, while LHCb focuses on Physics of b-quarks.

3.2 The ATLAS Detector

ATLAS (A Toroidal LHC Apparatus) is a general purpose detector and has been built for p-p collisions. The high luminosity and energy provided by the LHC offers the possibility to test and to measure the Standard Model processes and to search for new-physics phenomena. In order to achieve these goals the design of ATLAS is lead by the following requirements:

- Due to the high luminosity and the high bunch crossing rate, the detector requires radiation-hard and fast electronics. High granularity of the detector elements is needed to deal with the high particle flux and overlapping events.

- The ability to trigger on low transverse momentum objects with sufficient background rejection.

- Good electromagnetic calorimeter for electron and photon identification and measurement. In addition a hadronic calorimeter is needed to provide a good jet finding and measurement. The calorimeter should provide high acceptance in pseudo-rapidity with full azimuthal coverage for an accurate determination of the missing transverse momentum.

- Good muon identification and momentum resolution with the ability of accurate charge determination.

- Good charged-particle momentum resolution and measurement in the inner detector. Ability to identify and reconstruct secondary vertices of τ-leptons and b-jets.

The layout of the ATLAS detector is shown in Fig. 3.1. It has a length of 44 m and is 25 m in height. The overall weight is about 7000 tonnes.

After the introduction of the coordinate system of ATLAS, a short description of the subdetector components is given.

3.2.1 Coordinate System

The right-handed Cartesian coordinate system of ATLAS is defined as follows: The beam direction defines the z-axis. The x-axis is pointing from the interaction point towards the centre of the LHC ring. The y-axis is directed upwards.

The azimuthal angle ϕ is measured around the beam axis, and the polar angle θ is defined as the angle towards the z-axis. Instead the polar angle θ the pseudo-rapidity

$$\eta = -\ln(\tan(\theta/2))$$

is often used. The distance ΔR in the η-ϕ plane is defined as

$$\Delta R = \sqrt{(\Delta\eta)^2 + (\Delta\phi)^2} \ .$$

The transverse momentum p_T, the transverse energy E_T and the missing transverse momentum $E_\mathrm{T}^\mathrm{miss}$ are defined in the x-y plane.
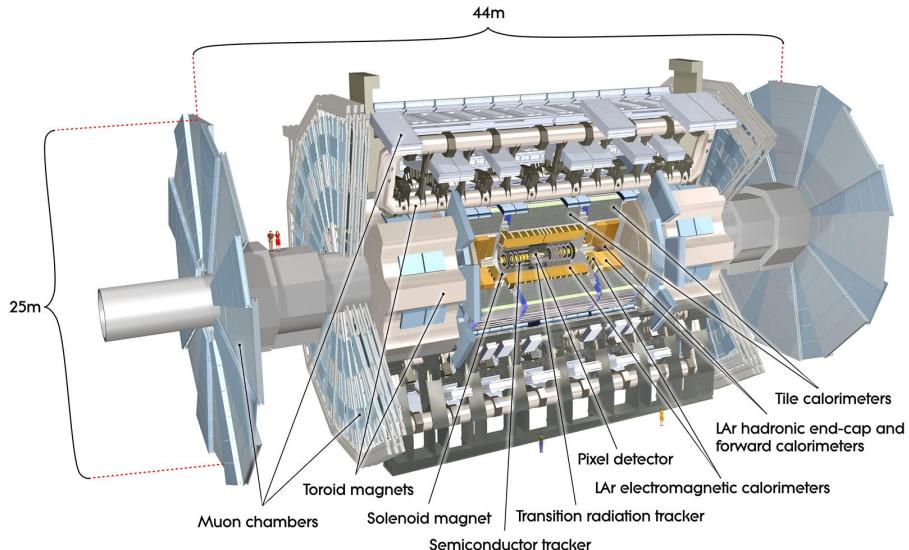
Figure 3.1: *Sketch of the ATLAS detector*

3.2.2 Inner Detector

The task of the inner detector is the identification and momentum measurement of charged particles. The tracks of charged particles are bent by a solenoidal magnetic field of up to 2 T produced by a superconducting magnet surrounding the inner detector.

In order to achieve the demanded momentum, impact parameter and vertex resolution semiconductor tracking detectors, pixel and silicon microstrip (SCT), are used. They cover the region up to $|\eta| < 2.5$. The semiconductor tracking detectors are surrounded by the straw tubes of the transition radiation tracker (TRT). The layout of the inner detector is shown in Fig. 3.2.

The pixel detector consists of 1744 identical pixel modules. They are arranged on three cylindrical layers in the barrel region and on three disks at each end-cap. The distance of the innermost layer to the beam pipe is about 5 cm. It enhances the secondary vertex measurement performance,. The pixel detector typically provides three high precision space points per track. The spatial resolution is about $10\,\mu$m in $R - \phi$ and about $115\,\mu$m in z.

The SCT detector consists of 4088 modules. Each SCT module has two pairs of identical silicon sensors glued back to back with a stereo angle of 40 mrad between them. The modules are arranged in four layers in the barrel region and nine disks in each end-cap region. In the barrel the strips of one of the pairs is aligned to be parallel to the beam direction. In the end-cap region one set of stripes is always running radially. The spatial resolution is about $17\,\mu$m in $R - \phi$ and about $580\,\mu$m in z.

The TRT detector consists of 4 mm diameter straw tubes filled with a gas mixture of 70% Xe, 27% CO_2 and 3% O_2. In each straw a tungsten wire is build-in and connected to a high positive voltage. In the barrel region the straws are parallel to the beam axis and are 1.44 m long. The straws in the end-cap region are arranged radially and are 0.37 m long. Between the straw tubes radiator material are inserted, which provide transition radiation

for electron identification. This radiation results in a higher signal level and improves the electron identification. On average a track creates 36 hits in the TRT. The TRT provides $R - \phi$ resolution of about $130\,\mu$m and covers the region up to $|\eta| < 2.0$.
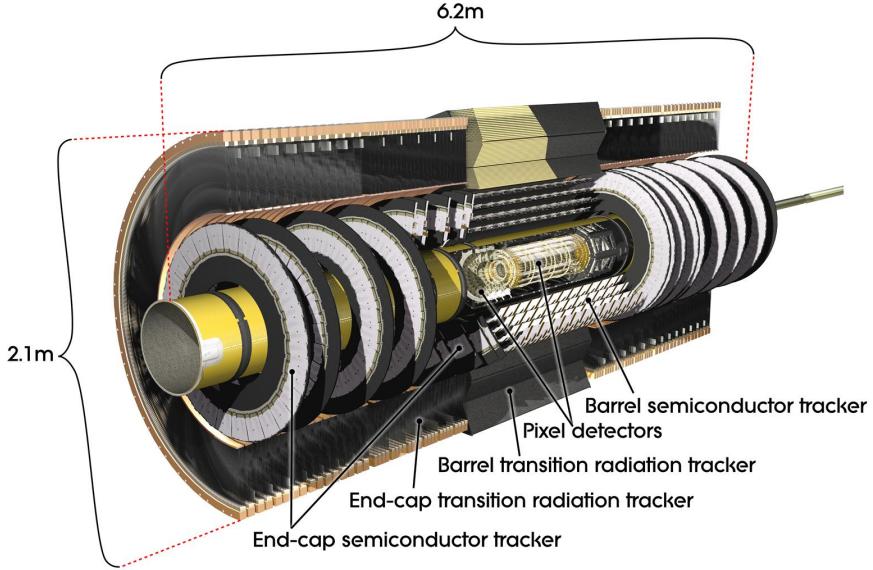
Figure 3.2: *Sketch of the inner detector.*

3.2.3   Calorimeter

The task of the calorimeter is to provide a precise measurement of the energy of particles, except muons and neutrinos. By having a full coverage over the azimuthal angle and a large acceptance in pseudo-rapidity up to $|\eta| < 4.9$, it is used to provide a measurement of the missing transverse energy.

The ATLAS calorimeter is divided into three parts, each using different techniques suited to the various requirements. A sketch of the calorimeter system is shown in Fig. 3.3.

Electromagnetic Calorimeter

The EM calorimeter consists of a barrel part ($|\eta| < 1.475$) and two end-cap components ($1.375 < |\eta| < 3.2$). It is a sampling calorimeter using liquid argon (LAr) as active material. The kapton electrodes and lead absorbers have an accordion shaped geometry, which provides a complete azimuthal coverage. The electrodes are placed in the middle of the gap between two absorbers. The size of the drift gap is $2.1\,$mm, corresponding to a drift time of $450\,$ns.

In the barrel the accordion waves are in beam direction and run in ϕ. The folding angle increases with increasing radius to keep the gap between the absorbers constant. In the end-cap the waves are in radial direction. To provide a constant gap between the absorbers the wave amplitude and folding angle increases with the radius.
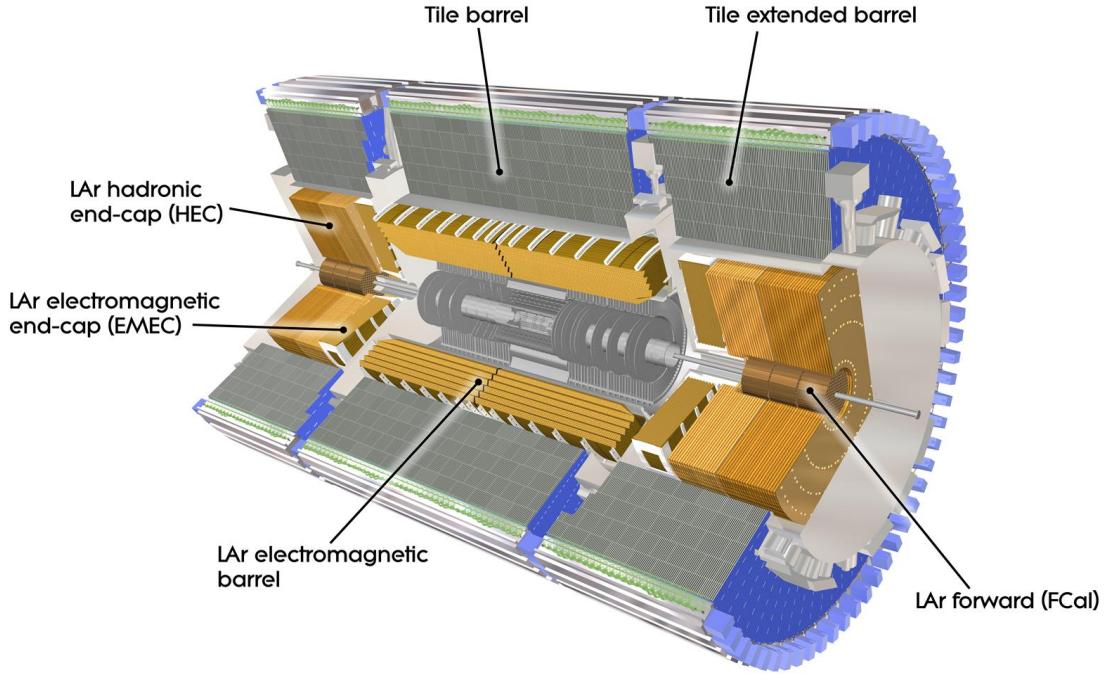
Figure 3.3: *Sketch of the calorimeter system.*

Up to $|\eta| < 2.5$ the calorimeter is segmented into three longitudinal sections with fine granularity. In the region $2.5 < |\eta| < 3.2$ the calorimeter is segmented into two longitudinal sections using a coarser granularity.

The material in front of the EM calorimeter sums up to a radiation length of about $22\,X_0$. To correct for the energy loss of particles started showering before the calorimeter, an active LAr layer called presampler, is placed in front of the calorimeter. In total the EM calorimeter has a radiation length of at least $22\,X_0$ in the barrel and $24\,X_0$ in the end-caps. The EM calorimeter is designed to reach an energy resolution for electrons and photons of [26]

$$\frac{\sigma(E)}{E} = \frac{0.1}{\sqrt{E}} \oplus 0.007 \ .$$

A summary of the EM calorimeter's main parameters is listed in Table 3.1.

Hadron Calorimeter

For the hadronic calorimeter various technologies are used to measure the energy. In the barrel a sampling calorimeter using steel as an absorber and plastic scintillator tiles as active material is placed. It is separated into a central barrel part $|\eta| < 1.0$ and two extended barrel parts $0.8 < |\eta| < 1.7$. The calorimeter is azimuthally segmented into 64 modules and longitudinally into three layers. In total it has a thickness of about 7.4 interaction lengths λ. Crossing ionising particles induce ultraviolet light in the scintillators. The light is

	Barrel		End-Cap	
Longitudinal segmentation and $|\eta|$ coverage				
Presampler	1 layer	$|\eta| < 1.52$	1 layer	$1.5 < |\eta| < 1.8$
Calorimeter	3 layer	$|\eta| < 1.35$	2 layer	$1.375 < |\eta| < 1.5$
	2 layer	$1.35 < |\eta| < 1.475$	3 layer	$1.5 < |\eta| < 2.5$
			2 layer	$2.5 < |\eta| < 3.2$
Granularity $\Delta\eta \times \Delta\varphi$ versus $|\eta|$				
Presampler	0.025×0.1	$|\eta| < 1.52$	0.025×0.1	$1.5 < |\eta| < 1.8$
Cal. 1st layer	$0.025/8 \times 0.025$	$|\eta| < 1.40$	0.050×0.1	$1.375 < |\eta| < 1.425$
	0.025×0.025	$1.40 < |\eta| < 1.475$	0.025×0.1	$1.425 < |\eta| < 1.5$
			$0.025/8 \times 0.1$	$1.5 < |\eta| < 1.8$
			$0.025/6 \times 0.1$	$1.8 < |\eta| < 2.0$
			$0.025/4 \times 0.1$	$2.0 < |\eta| < 2.4$
			0.025×0.1	$2.4 < |\eta| < 2.5$
			0.1×0.1	$2.5 < |\eta| < 3.2$
Cal. 2nd layer	0.025×0.025	$|\eta| < 1.40$	0.050×0.025	$1.375 < |\eta| < 1.425$
	0.075×0.025	$1.40 < |\eta| < 1.475$	0.025×0.025	$1.425 < |\eta| < 2.5$
			0.1×0.1	$2.5 < |\eta| < 3.2$
Cal. 3rd layer	0.050×0.025	$|\eta| < 1.35$	0.050×0.025	$1.5 < |\eta| < 2.5$

Table 3.1: *Main parameters of the electromagnetic calorimeter.*

converted into visible light by wavelength-shifter and is read out by photomultiplier tubes. The readout is grouped to cells which are almost projective in η towards the interaction region.

The hadronic end-cap calorimeter consists of two independent wheels per end-cap and covers the range $1.5 < |\eta| < 3.2$. Longitudinally it is segmented into two layers per wheel. It is a sampling calorimeter using copper as absorber and liquid argon as active material. The forward calorimeter consists of three modules on each end-cap. The first module is optimised for electromagnetic showers and uses cooper as absorber material, while the other two use tungsten. Liquid argon is used as active material. The forward calorimeter covers the region $3.1 < |\eta| < 4.9$ and is approximately ten radiation lengths thick. The hadronic calorimeter is designed to reach an energy resolution for jets of [26]

$$\frac{\sigma(E)}{E} = \frac{0.5}{\sqrt{E}} \oplus 0.03$$

in the barrel and end-cap region ($|\eta| < 3.2$), and about

$$\frac{\sigma(E)}{E} = \frac{1.0}{\sqrt{E}} \oplus 0.1$$

in the forward calorimeter ($|\eta| > 3.2$).

The main parameters of the hadronic calorimeter are summarized in Table 3.2.

3.2.4 Muon Spectrometer

The muon spectrometer ensures a precision measurement of muons exiting the calorimeter. A superconducting toroid magnet system provides the bending power to achieve an accuracy

LAr hadronic end-cap

$|\eta|$ coverage	$1.5 < |\eta| < 3.2$	
Number of layers	4	
Granularity $\Delta\eta \times \Delta\varphi$	0.1×0.1	$1.5 < |\eta| < 2.5$
	0.2×0.2	$2.5 < |\eta| < 3.2$

LAr forward calorimeter

$|\eta|$ coverage	$3.1 < |\eta| < 4.9$	
Number of layers	3	
Granularity $\Delta\eta \times \Delta\varphi$	FCal1: 3.0×2.6	$3.15 < |\eta| < 4.30$
	FCal1: $\sim$ four times finer	$3.10 < |\eta| < 3.15,$
		$4.30 < |\eta| < 4.83$
	FCal2: 3.3×4.2	$3.24 < |\eta| < 4.50$
	FCal2: $\sim$ four times finer	$3.20 < |\eta| < 3.24,$
		$4.50 < |\eta| < 4.81$
	FCal3: 5.4×4.7	$3.32 < |\eta| < 4.60$
	FCal3: $\sim$ four times finer	$3.29 < |\eta| < 3.32,$
		$4.60 < |\eta| < 4.75$

Scintillator tile calorimeter	**Barrel**	**Extended barrel**
$|\eta|$ coverage	$|\eta| < 1.0$	$0.8 < |\eta| < 1.7$
Number of layers	3	3
Granularity $\Delta\eta \times \Delta\varphi$	0.1×0.1	0.1×0.1
Last layer	0.2×0.14	0.2×0.1

Table 3.2: *Main parameters of the hadronic and the forward calorimeter.*

of 10% momentum resolution for a 1 TeV muon track.

The muon system consists of tree layers of precision tracking chambers. In the barrel region they are arranged on three concentric cylindrical layers, whereas in the end-cap region they form three wheels. The muon system covers the range $|\eta| < 2.7$. At the centre $\eta = 0$ a gap of up to $\Delta\eta < 0.08$ is left open to allow for services for the sub-detector systems.

The precision momentum measurement is performed by Monitored Drift Tubes (MDT) except for the inner-most end-cap layer. The drift tubes have a diameter of 3 cm and are filled with a gas mixture (Ar/CO_2). In each tube a tungsten-rhenium wire is inserted. A The MDTs consist of three to eight layers of drift tubes.

Because of the higher particle flux and muon-track density in the forward region, Cathode Strip Chambers (CSC) are used in the inner-most end-cap layer ($2.0 < |\eta| < 2.7$). CSCs are multiwired proportional chambers.

In addition to the precision chambers fast trigger chambers are used to allow to trigger on muon tracks. In the barrel region $|\eta| < 1.05$ tree layers of Resistive Plate Chambers complement the MDT layers. In the end-caps ($1.05 < |\eta| < 2.4$) Thin Gap Chambers are used. They are multiwired proportional chambers optimized for a quick response.
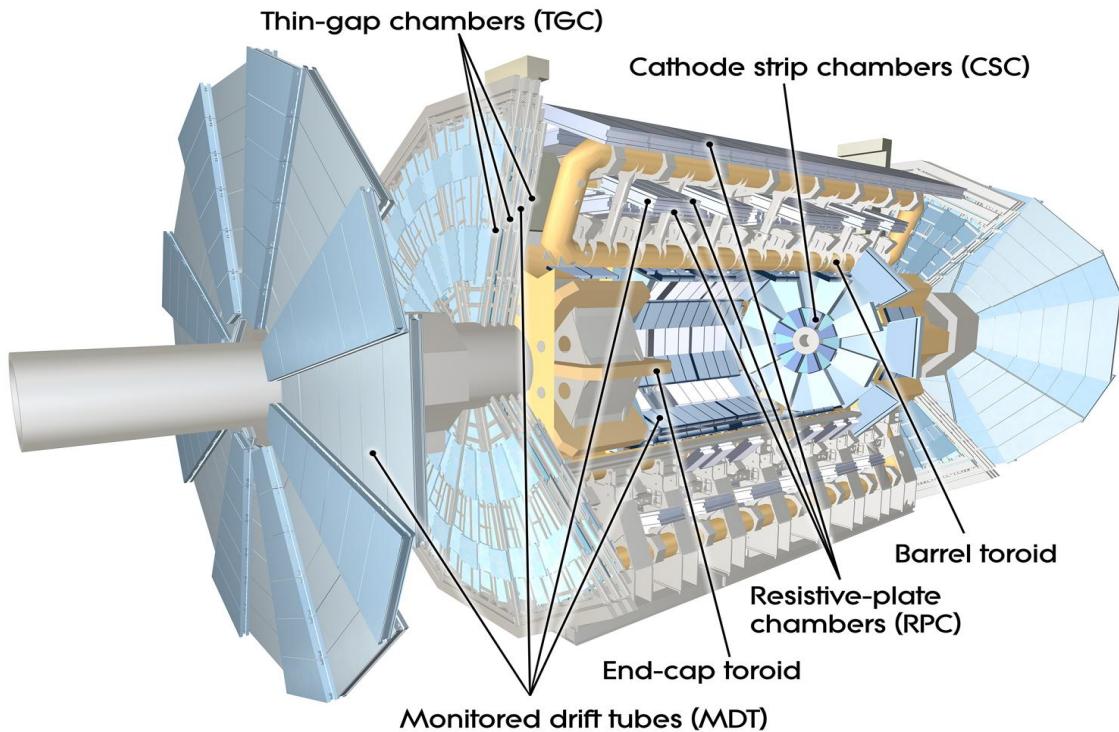
Figure 3.4: *Sketch of the muon system.*

3.2.5   Trigger

The proton-proton interaction rate at the design luminosity is about 40 MHz whereas the ability provided by the data recoding system is limited to a rate of 200 Hz. The huge rejection factor needed is realized by a three level trigger system. At the first trigger level (L1) the rate is reduced to 75 kHz by using a subset of the total detector. The event is searched for high transverse momentum objects and high missing or total transverse momentum. So called Regions-of-Interest (RoI) are defined, which are detector areas where interesting objects are found.

This information is passed to the second level trigger (L2). The RoI's are analysed using all detector components by full granularity. The L2 trigger reduces the event rate to approximately 3.5 kHz.

The third trigger level is called event filter. It analyses the full detector data by using offline analysis procedures and reduces the event rate to the required 200 Hz.

Chapter 4

Signal and Background Processes

The potential of the ATLAS experiment to discover the Standard Model Higgs boson is studied using simulated events assuming a centre-of-mass energy of 14 TeV. These events are produced using Monte Carlo generators, which simulate the physics processes taking place in the proton-proton collisions. A detector simulation is applied to the generated events to obtain the detector response. Since the simulation of each event is computationally very expensive, it takes about ten minutes, only a limited number of events can be simulated. Event filter are applied after the event generation to reduce the number of events which have to be simulated. They discard events that in any case will not be selected in the analysis.

For a Higgs boson in the mass range ($115\,\mathrm{GeV} < M_H < 130\,\mathrm{GeV}$) the dominant decay channel is $H \to b\bar{b}$. This decay channel is very difficult to handle, because of the large QCD background processes. For this reason the decay $H \to \tau\tau$ is considered. In particular the leptonic decays of the τ-leptons provide a clear signature of two isolated leptons and a considerable amount of missing transverse energy due to the four neutrinos. This signature offers a high rejection against QCD background processes, because the probability of a jet to be mis-identified as a jets is low[1]. Still the $H \to \tau\tau$ signal is confronted with a large background contributions from processes producing leptons, e.g. $Z \to \tau\tau \to \ell\ell + 4\nu$, $t\bar{t}$ production. These background processes are suppressed with the help of the characteristic signature of a Higgs boson produced in vector boson fusion.

In this chapter the topology of the signal and background processes are discussed. The Monte Carlo programs used for the event generation and the used cross section are presented. Finally a short description of the detector simulation is given.

4.1   Signal process: VBF Higgs $\to \tau\tau \to \ell\ell + 4\nu$

In the signal process the Higgs boson is produced by the fusion of two weak bosons. Feynman diagrams of t-, u-, and s-channel are shown in Fig. 4.1. The t- and u-channel diagrams

---

[1]The probability of a jet to be mis-identified as electron of medium (see Section 5.1) quality is 4.5^{-3} [1]. By requiring the electrons to be isolated the probability further decreases.
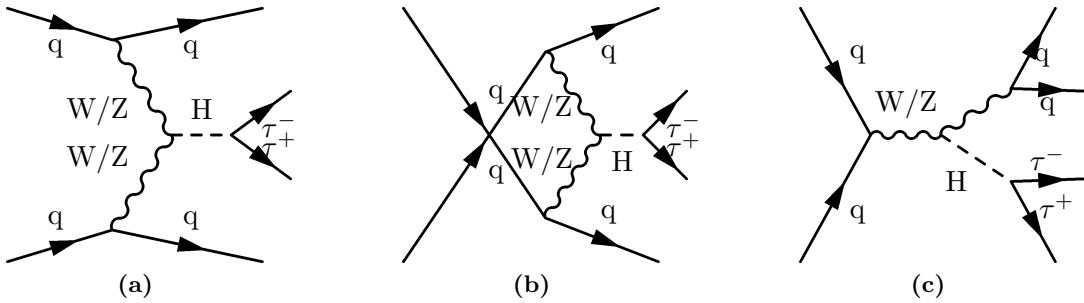
Figure 4.1: *Examples of leading order Feynman diagrams of a Higgs boson produced in vector boson fusion and its decay $H \to \tau\tau$. The left (t-channel) and middel (u-channel) are usually denoted as vector boson fusion, whereas the left (s-channel) is appropriately called Higgsstrahlung.*

are denoted as vector boson fusion, whereas the s-channel is called Higgsstrahlung. The weak bosons are emitted by two partons of the incoming protons. The scattered partons form jets, which have a large separation in pseudo-rapidity. Predominantly at least one of the jets is found in the forward region of the detector.

These jets are called tagging jets. Since no colour is exchanged between the partons, the production of additional jets between the tagging jets is suppressed.

In Fig. 4.2 the kinematic properties of the signal process are shown using generated (truth) quantities. The tagging jets are identified by matching the scattered outgoing partons from the hard interaction to truth jets. Truth jets are defined as jets created by the jet algorithm running on stable particles on the generator level, excluding muons and neutrinos. In the Figures 4.2b and 4.2c the distributions of the transverse momenta and pseudo-rapidity of the tagging jets are drawn. The tagging jets are clearly separated in η which results in a gap in the pseudo-rapidity distribution. Since the transverse momentum of the Higgs boson is balanced by the tagging jets, it has a considerable amount of transverse momentum, cf. Fig. 4.2a.

The decay of the Higgs boson into a pair of τ-leptons and their subsequent leptonic decay provides a clear signature of two isolated leptons and a considerable amount of missing transverse energy due to the four neutrinos from the τ-lepton decays. Figures 4.2e and 4.2f show the p_T distribution of the leptons from the decays of the τ-leptons and the amount of missing transverse energy caused by the neutrinos. The drop in the p_T distribution of the leptons at $5\,\mathrm{GeV}$ is caused by the application of an event filter. The few events with $p_\mathrm{T} < 5\,\mathrm{GeV}$ pass the event filter, because an additional lepton not originating from the Higgs boson decay was found in the event.

The Higgs boson production cross sections and branching ratios used in this study are taken from [29], cf. Tab. 4.1. The branching ratios of the Higgs boson have been determined using the programs *HDECAY* [30] and *PROPHECY4f* [31] with the addition of the full two-loop EW corrections evaluated in [32]. The given cross sections are inclusive, including next-to-leading order (NLO) QCD and EW corrections. The s-channel contributions are excluded, since their contributions are negligible when basic analysis requirement on the vector boson fusion topology [29] are applied.

The signal process has been generated using *HERWIG* [33] and does only consider the t-

M_H [GeV]	115	120	125	130
cross section $(qq \to qqH)$ [fb]	4436^{+156}_{-152}	4259^{+157}_{-143}	4100^{+151}_{-140}	3948^{+143}_{-133}
Br$(H \to \tau\tau$)	0.07386	0.06893	0.06203	0.05372

Table 4.1: *Higgs branching ratio and production cross section via VBF for a centre-of-mass energy of* 14 TeV*.*

channel and u-channel contributions. The τ-lepton decays are performed using *Tauola* [34], additional photon radiation is simulated using *Photos* [35]. The signal events are filtered using a lepton filter requiring at least two leptons (muons or electrons) with $p_T > 5$ GeV in $|\eta| < 2.7$.
The generated signal Monte Carlo datasets are summarised in Table 4.2.

4.2   Background processes

Processes resulting in two isolated leptons and two jets are potential background processes. As earlier studies (e.g. [1]) show, the dominant background processes in the channel $H \to \tau\tau \to \ell\ell + 4\nu$ are Z boson and $t\bar{t}$ production. The special signature of the signal process with two tagging jets and a suppressed jet activity in the central region demands a good description of jet activity in the background processes. For this reason Monte Carlo generators employing a matching between partons generated in matrix-element calculation and the parton-shower are utilised. In the following a detailed overview of the background processes and how the simulated events are generated is given.

	Cross section [fb]	Pile-Up	Events	Integrated Luminosity [fb^{-1}]
Herwig $H \to \tau\tau \to \ell\ell + 4\nu$ datasets				
$M_H = 115$ GeV	22.63	no	39074	1727
		yes	23725	1048
$M_H = 120$ GeV	20.39	no	49750	2440
		yes	41491	2035
$M_H = 125$ GeV	17.98	no	9750	542
		yes	18550	1032
$M_H = 130$ GeV	15.31	no	24340	1590

Table 4.2: *Overview of Signal Monte Carlo samples. The cross sections include the filter efficiencies.*

4.2.1 $Z(\to \mu\mu/ee/\tau\tau)$+jets

The production of a Z boson accompanied by jets is the main background process. To mimic the signal process two leptons and a certain amount of missing transverse energy are
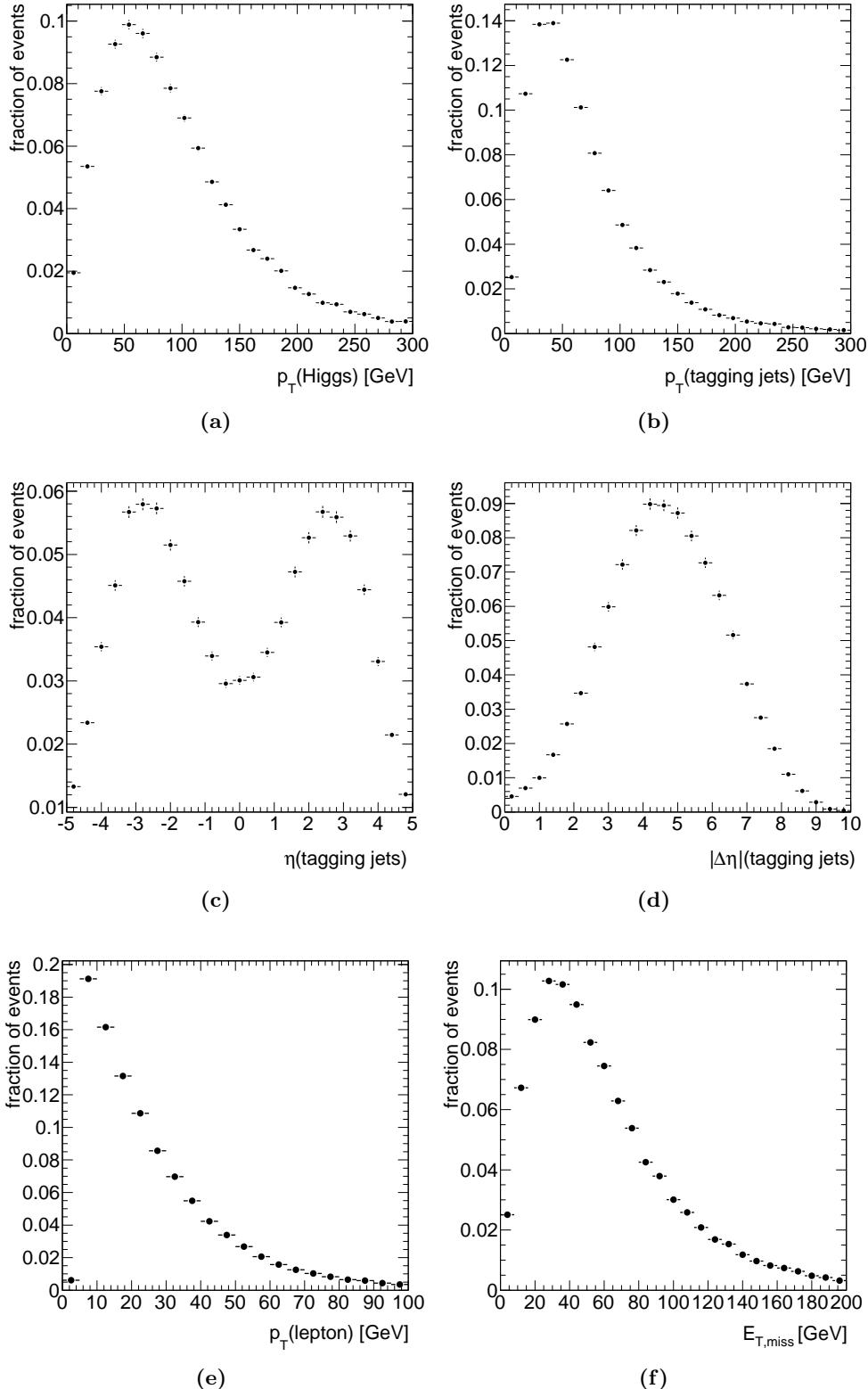
Figure 4.2: *Kinematic properties of the signal process. The quantities are derived using Monte-Carlo truth objects: a) transverse momentum of the Higgs boson, b) transverse momentum of the tagging jets, c) pseudo-rapidity of tagging jets, d) distance in pseudo-rapidity between the tagging jets, e) transverse momenta of the leptons from the $H \rightarrow \tau\tau \rightarrow \ell\ell + 4\nu$ decay, f) missing transverse energy of the neutrinos from the $H \rightarrow \tau\tau \rightarrow \ell\ell + 4\nu$ decay. The jets are selected by matching the scattered outgoing partons from the hard process to particle jets reconstructed using Monte-Carlo truth objects.*

needed. Accordingly the decay of the Z boson to hadrons and neutrinos do not contribute to the background, since no charged leptons are in the final state. The decay of the Z boson to electrons and muon has only a small contribution to the background. It can be suppressed by requiring a certain amount of missing transverse energy and by requiring the invariant di-lepton mass being below the Z peak. Accordingly, only the decay $Z \rightarrow \tau\tau \rightarrow \ell\ell + 4\nu$, providing two leptons and $E_{\mathrm{T}}^{\mathrm{miss}}$ due to the neutrinos, has a significant background contribution. It is an irreducible background, since the Higgs boson decay is exactly imitated.

The Z boson production is divided into two categories: parton-parton interaction without colour flow (EW) (Fig. 4.3a and 4.3b) and parton-parton interaction involving colour flow (QCD) (Fig. 4.3c).

The EW process is expected to be the dominant background process, because it is kinematically very similar to the signal process as it is described by similar Feynman diagrams. But it turns out that due to its large cross section the QCD process has the largest contribution. The main quantity to discriminate the EW background process from the signal process is the reconstructed mass $M_{\tau\tau}$. For details of its reconstruction see Chapter 6.1. The $Z \rightarrow \tau\tau \rightarrow \ell\ell + 4\nu$ QCD process differs from the signal process by its jet kinematics, and can be suppressed utilising the kinematic properties of the tagging jets.

For each of the processes $Z \rightarrow ee$ QCD, $Z \rightarrow \mu\mu$ QCD and $Z \rightarrow \tau\tau$ QCD the cross section is $(2036 \pm 60)\,\mathrm{pb}$ [36]. It has been calculated at NNLO accuracy using the program *FEWZ* [37,38] and contains a requirement on the invariant di-lepton mass of $M_{\ell\ell} > 60\,\mathrm{GeV}$. The cross section for the $Z \rightarrow \tau\tau$ EW process is $1.8\,\mathrm{pb}$ calculated using *Sherpa* [39] with LO accuracy.

Monte Carlo Event Generation

The generated Monte Carlo datasets are summarised in Table 4.4.

$Z(\rightarrow \mu\mu/ee/\tau\tau)$ **QCD**

> The QCD Z+jets events with the decays $Z \rightarrow \mu\mu$, $Z \rightarrow ee$ and $Z \rightarrow \tau\tau \rightarrow \ell\ell + 4\nu$ were produced using the *Alpgen* [40] Monte Carlo generator. The interference between Z and γ^* are included. A requirement on the invariant di-lepton mass $60\,\mathrm{GeV} < M_{\ell\ell} < 200\,\mathrm{GeV}$ was applied. *Alpgen* considers up to five jets in the matrix-element and employs the MLM matching [41] procedure between partons generated in matrix-element calculation and the parton-shower. The parton-shower and hadronisation are performed using *Jimmy* [42]. τ-lepton decays were performed using *Tauola*. Additional photon radiation is simulated using *Photos*. *Alpgen* does not take the pure electroweak (EW) production of Z+jets into account. Furthermore processes like $Z + b(b)$ are not included.
>
> Due to the large cross section of the $Z \rightarrow \ell\ell$ QCD process an event filter was applied after the event generation. In particular two leptons, muons or electrons, in $|\eta| < 2.7$ with $p_T > 10\,\mathrm{GeV}$ in the event were required. Furthermore a VBF forward jet filter was applied. This filter requires at least two jets with $|\eta| < 5.0$ and $p_T > 15\,\mathrm{GeV}$. The jets are built from final state truth particles excluding muons and neutrinos using a cone algorithm with cone parameter $R = 0.4$. Of all jet pairs which fulfil the

above conditions at least one must have an invariant mass of $M_{jj} > 300\,\text{GeV}$ and a difference in pseudo rapidity of $|\Delta\eta_{jj}| > 2.0$.

The Monte Carlo events, generated using *Alpgen*, are normalized to the NNLO cross section using a k-factor of 1.24.

$Z \to \tau\tau$ **EW**

The EW $Z \to \tau\tau$ +jets events are produced using *Sherpa* [39]. Up to three jets are considered in the matrix element. Sherpa uses the matrix-element generator *AMEGIC++* [43] and employs the CKKW [44] parton-shower and matrix-element matching technique. The interference between Z and γ^* are included. A requirement on the invariant di-lepton mass $M_{\ell\ell} > 60\,\text{GeV}$ was applied.

No event filter was applied.

$Z \to \tau\tau$ **QCD Sherpa**

Since the *Alpgen* Z+jets samples do not include processes like $Z + b(b)$ a dedicated $Z \to \tau\tau$ +jets QCD sample, generated using *Sherpa* and including processes like $Z + b(b)$, has been used. The interference between Z and γ^* are included. A requirement on the invariant di-lepton mass $M_{\ell\ell} > 60\,\text{GeV}$ was applied.

The *Sherpa* $Z \to \tau\tau$ +jets QCD events are filtered using lepton filter requiring at least one electron or muon in $|\eta| < 2.7$ with a transverse momentum of $p_T > 15\,\text{GeV}$.

The *Sherpa* $Z \to \tau\tau$ +jets QCD events are normalized to the NNLO cross section calculated using *FEWZ*.

The detector simulation of the *Sherpa* $Z \to \tau\tau$ +jets QCD events was performed using *ATLFAST-II* [45].

4.2.2   Top Quark Pair Production

The production of a pair of top quarks is the second most important background. An example Feynman diagram is shown in Fig. 4.3d. The leptonic decay of the W bosons, produced in the top quark decays, results in the final state of two leptons and missing transverse energy. The two jets from the b quarks are misidentified as tagging jets. In this way the $t\bar{t}$ process provides a final state similar to the signal process.

The top quark pair production with hadronically decaying W bosons is negligible, since the probability of a jet to be misidentified as a muon or electron is very low. Leptons resulting from the semi-leptonic decay of the b-jets are unlikely to be isolated.

The $t\bar{t}$ background can be suppresses utilising the special jet kinematics of the signal process. Furthermore, the $t\bar{t}$ process is a non-resonant background, which means the distribution of the reconstructed mass $M_{\tau\tau}$ is rather flat and provides good background rejection. Even though the kinematics of the $t\bar{t}$ background are very different compared to the signal process, its high cross section of about $(833 \pm 100)\,\text{pb}$ [36] makes it one of the main background sources. The cross section has been calculated using NLO accuracy including the resummation of the next-to-leading logarithms [46].

Monte Carlo Event Generation

The $t\bar{t}$ Monte Carlo events were generated using *MCAtNLO* [47]. *MCAtNLO* simulates the process including the full first higher-order corrections, that means a full NLO result is obtained. The parton-shower and the hadronisation were performed using *Jimmy*. In all cases of τ-lepton decays, the decay is performed using *Tauola* and additional photon radiation is simulated using *Photos*.
The $t\bar{t}$ events are filtered requiring at least one leptonic decay of the W boson from the top quark decay. The generated Monte Carlo datasets are summarised in Table 4.3.

4.2.3 W+jets

The production of a W boson accompanied by jets is a further background process. The leptonic decay of the W boson provides one lepton and missing transverse energy, due to the neutrino. Thus the second lepton must be a misidentified jet. Since the probability of a jet to be misidentified as a muon or an electrons is very low, this process is of minor importance. To mimic the signal process two or more additional jets are needed. An example of a Feynman diagram to produce a W boson in addition to three jets is shown in Fig. 4.3f.
The cross section of this process is $20460 \pm 615\,\mathrm{pb}$ [36]. It is calculated to NNLO accuracy using the program *FEWZ*. This background is of small relevance after the application of all analysis requirements.

Monte Carlo Event Generation

The W+jets Monte Carlo events were generated using *Alpgen*. The parton-shower was performed using *Jimmy*. A leptonic decay of the W boson is required. In all cases of τ-lepton decays, the decay is performed using *Tauola* and additional photon radiation is simulated using *Photos*.
A event filter was applied, requiring one muon or electron in $|\eta| < 2.7$ with $p_T > 10\,\mathrm{GeV}$. Furthermore a VBF forward jet filter was applied. This filter requires at least two jets with $|\eta| < 5.0$ and $p_T > 15\,\mathrm{GeV}$. Of all jet pairs which fulfil the above conditions at least one must have an invariant mass of $M_{jj} > 300\,\mathrm{GeV}$ and a difference in pseudo rapidity of $|\Delta\eta_{jj}| > 2.0$.
The Monte Carlo events are normalized to the NNLO cross section using a k-factor of 1.15. The generated Monte Carlo datasets are summarised in Table 4.5.

4.2.4 **Boson Pair Production**

The processes of the form WW, two ZZ and WZ with the leptonic decay of the bosons, can provide a signature similar to the signal. In the following they are referred to as di-boson background.
In Fig. 4.3e a Feynman diagram is shown, which produces a pair of W bosons and in addition two jets. In this example the two jets could provide a signature similar to the tagging jets in the signal process. The leptonic decay of both W bosons provide two leptons

and missing transverse energy.

However, as early studies show this background processes are of minor importance. Due to the low cross section the di-boson processes can be well suppressed by using the kinematic signature of the jets in the signal process.

The cross section of the di-boson Monte Carlo samples are $\sigma_{WW} = 111.6\,\mathrm{pb}$, $\sigma_{ZZ} = 14.8\,\mathrm{pb}$, $\sigma_{W^-Z} = 18.4\,\mathrm{pb}$ and $\sigma_{W^+Z} = 29.4\,\mathrm{pb}$ respectively [36]. They are calculated to NLO accuracy using *MCAtNLO*.

Monte Carlo Event Generation

The di-boson samples were generated using *MCAtNLO* while the parton-shower and the hadronisation were performed by *Jimmy*. In all cases of τ-lepton decays, the decay is performed using *Tauola* and additional photon radiation is simulated using *Photos*. No event filter was applied. The generated Monte Carlo datasets are summarised in Table 4.3.

(a) *Electroweak Z+jets production.*

(b) *Electroweak Z+jets production.*

(c) *QCD Z+jets production.*

(d) *Top quarks pair production.*

(e) *Vector boson pair production.*

(f) *W+jets production.*
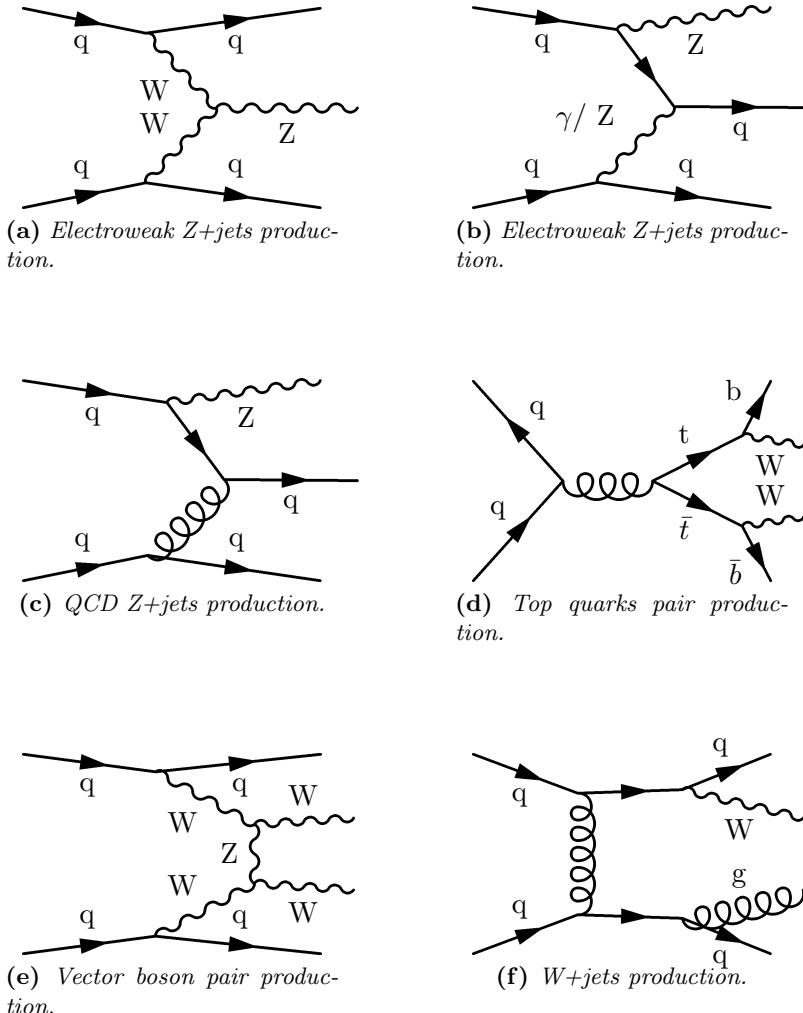
Figure 4.3: *Example Feynman diagrams for background processes to the VBF $H \to \tau\tau \to \ell\ell + 4\nu$ channel.*

4.3   Detector Simulation

The ATLAS detector simulation is part of the ATLAS software framework *Athena*[2]. Except for the *Sherpa* $Z \rightarrow \tau\tau$ +jets QCD events the whole analysis is based on events simulated using the full ATLAS detector simulation. The ATLAS detector simulation is part of the ATLAS software framework *Athena*.

The full ATLAS detector simulation is based on the program *Geant4* [48], which produces energy depositions in the detector material, called *Hits*. These *Hits* are the result of a precise simulation of the behaviour of particles inside the detector. This implies a precise description of the detector geometry and the used material is needed. In this analysis the detector description ATLAS-GEO-02-01-00 is used. This implies a displacement of the beam spot by 1.5/2.5/-9 mm in x/y/z.

By simulating the behaviour of the detector read out electronics the digitisation converts the energy depositions into read out signals. This implies a precise model of the charge collection, electronic noise and variations in detector response for each subdetector. The effects of pileup, cavern background, beam-halo and beam-gas are added in this step. The bunch-crossing and timing information are taken into account.

The detector simulation of the *Sherpa* $Z \rightarrow \tau\tau$ +jets QCD events was performed using the *ATLFAST-II*. It has the advantage of being computationally much faster using a less complex simulation of the calorimeter, while the inner detector and the muon spectrometer are based on the full ATLAS detector simulation. The used *ATLFAST-II* version is not capable to run a trigger and pile-up simulation.

4.4   Pile–Up

At the LHC design luminosity of $L = 10^{34} \, \mathrm{cm}^{-2}\mathrm{s}^{-1}$ in average 23 proton-proton interactions happen per bunch crossing. Whereas most of these interactions are QCD processes with low energetic jets, each interesting physics event is superimposed by these interactions. These overlaid events are called *in–time* pile-up events.

Due to the long response time of some subdetector systems, e.g. 500 ns for the LAr calorimeter, the detector is sensitive to interactions in previous and later bunch crossing than the bunch crossing that contains the physics event. Within ATLAS this is often called *out–of–time* pile-up.

The presence of pile–up has different impacts on the physical reconstructed objects, which will affect the analysis of the signal process. The additional interactions produce a large number of additional particles. The additional energy depositions in the calorimeter exacerbate the calibration and reconstruction of calorimeter based objects. In particular this has a large impact on the resolution of the missing transverse energy, which is degraded in the presence of pile-up. Furthermore, pile-up leads to an increase of the number of reconstructed jets and will affect the typical jet signature of the signal process. In particular the additional jets may show up between the tagging jets and degrade the central jet veto.

In this thesis pile-up conditions corresponding to a luminosity of $10^{33} \, \mathrm{cm}^{-2}\mathrm{s}^{-1}$ with a bunch

---

[2]Athena version 14.2.25 was used for the detector simulation and event reconstruction throughout this thesis.

spacing of 75 ns are considered. This corresponds to on average about seven proton-proton interactions per bunch crossing. In the event simulation pile-up is simulated by overlaying *Geant4* hits of *minimum bias* events with *Geant4* hits of the event of interest. The *Minimum bias* events are simulated as non-diffractive inelastic proton-proton interactions using *Pythia* [49]. Since no *minimum bias* events generated at a centre-of-mass energy of 14 TeV were available, *minimum bias* events generated at a centre-of-mass energy of 10 TeV were used.

In addition to pile-up, *cavern background* degrades the performance of the muon system. Thermal neutrons and low energy photons emerge due to activation of materials in the detector, its support structure, and the cavern. This results in a steady rate of compton electrons and spallation protons, which are observed in the muon system.
Furthermore, interactions resulting from gas present in the beam pipe and protons hitting parts of the detector or a collimator occur.

	Cross section section [pb]	Pile-Up	Events	Integrated Luminosity [fb^{-1}]
MCAtNLO $t\bar{t}$ Monte Carlo samples:				
	467	no	1861878	2.6
	467	yes	957113	1.5
MCAtNLO Di-Boson Monte Carlo datasets:				
WW	111.6	no	49767	0.3
		yes	49979	0.3
W-Z	18.4	no	49999	2.0
		yes	49999	2.0
W+Z	29.4	no	50000	1.2
		yes	40000	1.0
ZZ	14.8	no	49955	2.3
		yes	38877	1.7

Table 4.3: *Overview of the $t\bar{t}$ and di-boson background Monte Carlo samples. The filter efficiencies are included in the cross sections.*

		Cross section [pb]	Pile-Up	Events	Integrated Luminosity [fb^{-1}]
Alpgen QCD datasets:					
$Z \to \tau\tau \to \ell\ell$	+0 jets	0.39	no	59383	151
			yes	62879	160
	+1 jet	0.36	no	45500	128
			yes	45250	127
	+2 jets	0.43	no	338748	795
			yes	338498	795
	+3 jets	0.37	no	217011	586
			yes	216761	585
	+4 jets	0.23	no	33499	148
			yes	33286	147
	$\geq$ 5 jets	0.13	no	16000	121
			yes	16000	121
$Z \to \mu\mu$	+0 jets	9.2	no	39748	4.3
			yes	39748	4.3
	+1 jet	8.4	no	79999	9.5
			yes	79478	9.4
	+2 jets	9.4	no	98899	10.5
			yes	98753	10.5
	+3 jets	8.1	no	99750	12.3
			yes	99500	12.2
	+4 jets	4.7	no	48850	10.4
			yes	48881	10.4
	$\geq$ 5 jets	2.6	no	30000	11.5
			yes	29750	11.4
$Z \to ee$	+0 jets	14.9	no	39000	2.6
			yes	39000	2.6
	+1 jet	10.0	no	79999	8.0
			yes	74750	7.5
	+2 jets	10.9	no	104996	9.7
			yes	104746	9.7
	+3 jets	8.9	no	99998	11.2
			yes	99748	11.2
	+4 jets	5.1	no	50000	9.8
			yes	49750	9.7
	$\geq$ 5 jets	2.7	no	29954	11.2
			yes	29954	11.2
Sherpa dataset:					
$Z \to \tau\tau + \leq 3jets$:	EW	1.8	no	159269	89
	QCD	306.3	no	919270	3

Table 4.4: *Overview of the used Z+jets Monte Carlo samples. The cross sections include the filter efficiencies.*

		Cross section [pb]	Pile-Up	Events	Integrated Luminosity [fb^{-1}]	
$W \to \tau\tau$	+0 jets	25	no		10000	0.4
			yes		10000	0.4
	+1 jet	24	no		15000	0.6
			yes		15000	0.6
	+2 jets	25	no		50000	2.0
			yes		50000	2.0
	+3 jets	20	no		72700	3.6
			yes		72700	3.6
	+4 jets	12	no		35000	2.8
			yes		35000	2.8
	≥ 5 jets	7.7	no		15000	2.0
			yes		15000	2.0
$W \to \mu\mu$	+0 jets	0.39	no		59383	151
			yes		19999	0.1
	+1 jet	104	no		29949	0.3
			yes		29949	0.3
	+2 jets	109	no		98000	0.9
			yes		100000	0.9
	+3 jets	93	no		149748	1.6
			yes		149748	1.6
	+4 jets	53	no		69999	1.3
			yes		69999	1.3
	≥ 5 jets	31	no		29749	1.0
			yes		29749	1.0
$W \to ee$	+0 jets	182	no		19950	0.1
			yes		19950	0.1
	+1 jet	119	no		29998	0.3
			yes		29998	0.3
	+2 jets	119	no		99999	0.8
			yes		99999	0.8
	+3 jets	99	no		149997	1.5
			yes		149997	1.5
	+4 jets	54	no		29999	0.6
			yes		69956	1.3
	≥ 5 jets	31	no		29975	1.0
			yes		29975	1.0

Table 4.5: *Overview of the used W+jets Monte Carlo samples. The cross sections include the filter efficiencies.*

Chapter 5

Event Reconstruction

This chapter gives an overview of the reconstruction of the main Physics objects: electrons, muons, τ-leptons and jets. The overview is restricted to algorithms that are actually used in this thesis. It is based on [1, 24] and the ATLAS software framework *ATHENA* Release 14, recent improvements are not considered.

5.1   Electron Reconstruction

The ATLAS reconstruction software provides three electron reconstruction algorithms. One algorithm, dedicated to low energy electrons, is seeded by inner detector tracks and matches them to energy depositions in the EM calorimeter. Another algorithm to reconstruct electrons in the forward region ($2.5 < |\eta| < 4.9$), which is not covered by the inner detector, is based on topological calorimeter clusters [50].

The electrons used in this thesis are reconstructed by a cluster-based algorithm dedicated to isolated high energy electrons. The electron reconstruction is seeded using a sliding-window algorithm [50] with a window size corresponding to 5×5 cells ($\eta \times \phi$) in the middle layer of the electromagnetic calorimeter. The clusters are positioned to maximise the amount of energy within the cluster. The E_T threshold for an electron seed is $E_T > 3\,\mathrm{GeV}$. Using the seed a cluster of size 0.075×0.175 ($\Delta\eta \times \Delta\phi$) in the barrel region ($0.125 \times 0.125$ in the end-cap region) is reconstructed. This choice has been optimised to collect all energy deposited by the electron considering the radiation of hard bremsstrahlung, noise and pile-up.

A matching track is searched among all inner detector tracks which do not belong to photon conversion. It is required to match the cluster within $\Delta\eta \times \Delta\phi$ of 0.05×0.1. The ratio of the cluster energy divided by the momentum of the track has to be lower than 10.

The identification variables are then calculated combining inner detector and calorimeter quantities. Three different sets of requirements on the electron identification variables are defined: loose, medium and tight. These sets of requirements correspond to a different identification quality depending on identification efficiency and jet rejection. In this thesis *medium* class electron are used, which applies requirements on the hadronic leakage and on shower-shape variables, derived from the middle layer of the EM calorimeter. Furthermore,

shower-shape variables using the strip-layer of the EM calorimeter are used. Requirements on the number of pixel and SCT hits of the matched track are applied. Detailed information can be found in [1].

5.2   Muon Reconstruction

ATLAS has different strategies to reconstruct and identify muons. The straight forward approach is employed to reconstruct the so-called standalone muons. The algorithm used to do that is called *Muonboy* [51]. In the first step regions of activity are defined by hits in the trigger chambers. Seeded by these regions the hits in each muon station are combined to build track segments.
The second step links these track segments to form tracks starting in the middle and outer stations. The tracks are then extrapolated to the interaction point considering a detailed description of the detector geometry and magnetic field. The energy loss of muons is assigned based on the material they have crossed in the calorimeter.
The *Staco* [51] algorithm combines muon spectrometer tracks, reconstructed using *Muonboy*, with inner detector tracks to identify combined muons. The quality of the combination is expressed in the variable χ^2_{match}, defined as:

$$\chi^2_{match} = (T_{MS} - T_{ID})^T (C_{MS} - C_{ID})(T_{MS} - T_{ID}) \ .$$

Here T stands for a vector of five track parameters, and C is its covariance matrix. The subscripts ID and MS refer to the inner detector and the muon spectrometer. From all combinations only the one with the lowest χ^2_{match} is kept.
The combined track is obtained by a statistical combination of the inner detector track and the track in the muon spectrometer:

$$T = (C^{-1}_{MS} + C^{-1}_{ID})^{-1}(C^{-1}_{MS}T_{MS} + C^{-1}_{ID}T_{ID}) \ ,$$

with its covariance matrix:

$$C = (C^{-1}_{MS} + C^{-1}_{ID})^{-1} \ .$$

If the muon spectrometer track of a standalone muon is part of a combined muon, the standalone muon is not recorded. This avoids double counting between standalone and combined muons.

The spectrometer tagging algorithms *MuTag* is mainly aimed to complement *Muonboy* and *Staco* for low $p_{\rm T}$ muons. It starts by propagating all inner detector tracks with sufficient momentum, which are not used by *Staco*, to the first station of the muon spectrometer. Nearby segments not used by *Muonboy* and *Staco* are then combined. The muon kinematics are evaluated using the inner detector track only. Since *MuTag* makes only use of inner detector tracks and muon spectrometer segments not used by *Muonboy* and *Staco*, double counting is avoided.

5.3 τ-Lepton Reconstruction

τ-leptons are the heaviest leptons. Due to their short lifetime of about 290.6 fs [9] τ-leptons travel only a short distance before decaying and cannot be directly observed in the detector.

In about 35% of all cases [9] a τ-lepton decays into a lepton and the corresponding neutrino. Since the neutrinos leave any signal in the detector, they contribute to the missing transverse energy, cf. Section 5.5. The leptons are reconstructed using the corresponding lepton reconstruction algorithm. Since the leptonic decay of a τ-lepton can hardly be distinguished from a primary electron or muon no dedicated algorithm for its reconstruction is provided.

For this reason the τ-lepton reconstruction within ATLAS refers always to hadronically decaying τ-lepton. Detailed information of the reconstruction of τ-lepton decays into hadrons can be found in [1].

In this thesis only decays of τ-leptons into leptons are considered.

5.4   Jet Reconstruction

Several algorithms to reconstruct jets are available in the ATLAS software framework. Throughout this thesis a seeded fixed-cone algorithm is used. While other algorithms are preferable because they are collinear and infrared safe [52], jets reconstructed with the cone algorithm have the advantage of being well calibrated in the used ATLAS software release. Basically every object having a four momentum vector can be used as input to the jet finder, e.g. calorimeter cluster, particle tracks or Monte-Carlo truth objects. The jets used in this thesis are only calorimeter based objects. As input topological calorimeter clusters are used [50]. In the following a short review of the used jet finding algorithm, topological cluster and jet calibration is given.

Fixed Cone Jet Finder in ATLAS

The ATLAS implementation of the seeded fixed cone jet finder follows the algorithm description of [52]. All input objects above a certain seed threshold ($E_\mathrm{T} > 1\,\mathrm{GeV}$) are ordered by decreasing E_T. They serve as seeds for the jet finding procedure.

Starting with the highest E_T object all objects in a cone of $\Delta R = \sqrt{\Delta\eta^2 + \Delta\phi^2} < R_{cone}$ are combined with the seed. R_{cone} is a fixed cone radius. The two default values in ATLAS are $R_{cone} = 0.4$ and $R_{cone} = 0.7$. The combination is done by adding the four momenta of the objects. If the combined object is regarded as stable, i.e. the direction corresponds to the direction of the seed object within errors, it is called a protojet. Otherwise the new combined object serves as the new seed and the procedure is iterated. This continues until no more seeds are available.

The resulting protojets are overlapping, which means that they can share constituents. If two protojets share more than 50% of their transverse energy, they are merged by adding the four momenta. Otherwise the overlap is resolved by assigning each shared object to the nearest jet. After this merge/split procedure the protojets are called jets.

Topological Cell Cluster

Topological cell clusters are three-dimensional calorimeter clusters representing the energy depositions of particles entering the calorimeter. The cluster formation starts from seed

cells exceeding an energy significance of $\frac{|E_{cell}|}{\sigma_{noise}} > 4$. The noise threshold includes electronic and pile-up noise. All neighbouring cells are added. If the energy significance of an added cell is above a secondary seed threshold of $\frac{|E_{cell}|}{\sigma_{noise}} > 2$, this cell is regarded as a secondary seed and all neighbouring cells are added. This procedure is repeated until no further secondary seed is found. Finally all surrounding cells are added.

After the formation all topological clusters are analysed for local signal maxima. If more than one is found, the cluster is split along the line of local minima, which separates the maxima.

In this way three-dimensional calorimeter clusters of flexible size are built. Due to the noise threshold of the seed cells, topological clusters have an intrinsic noise suppression. Cells with low energy are unlikely to be added to clusters.

Jet Calibration

Before starting clustering and jet-finding algorithms the calorimeter cells are calibrated to the *electromagnetic energy scale*[1]. The needed calibration constants can be derived in data using e.g. $Z \to ee$ decays.

After the jet finding process the jets are still calibrated to the *electromagnetic energy scale.* Since the ATLAS calorimeter is not compensating, a correction to the hadronic energy scale is necessary for jets. This is based on a cell signal weighting similar to the approach developed in the H1 experiment [53].

The basic idea is that low signal densities in the cells indicate a hadronic signal, while high signal densities are more likely caused by an electromagnetic shower. The weighting is applied to all calorimeter cells associated to a jet. The weights ω depend on the cell location $\vec{X}_i$ in the calorimeter and on the cell signal density $\rho = \frac{E_i}{V_i}$. E_i is the energy of a cell at the electromagnetic scale, and V_i is the cell volume. The jet four momentum $(E_{cal}, \vec{p}_{cal})$ is then recalculated from the weighted cells, which are treated as massless four momenta $(E_i, \vec{p}_i)$:

$$(E_{cal}, \vec{p}_{cal}) = \left(\sum_i^{N_{cells}} \omega(\rho_i, \vec{X}_i) E_i, \ \sum_i^{N_{cells}} \omega(\rho_i, \vec{X}_i) \vec{p}_i \right) \ .$$

The weights are derived by minimising the resolution of the energy measured using seeded fixed cone calorimeter jets with respect to nearby Monte Carlo truth particle jets in simulated QCD jet events. In this way all detector effects, including missing signals caused by the bending of low-$p_{\rm T}$ particles by the magnetic field of the central solenoid, are taken into account.

The calibration weights depend on the choice of the jet finding algorithm and the selected input objects.

---

[1]The calibration to the electromagnetic energy scale means that the detector response is calibrated to the energy deposition of a corresponding electron.

5.5   Missing Transverse Energy

One of the crucial ingredients to perform this analysis is a precise measurement of the missing transverse energy $E_{\mathrm{T}}^{\mathrm{miss}}$. While the measurement of $E_{\mathrm{T}}^{\mathrm{miss}}$ is sensitive to the missing transverse momentum it is often called missing transverse energy.

The reconstruction of $E_{\mathrm{T}}^{\mathrm{miss}}$ is based on the measured energy in the calorimeter and the reconstructed muon tracks.

The $E_{\mathrm{T}}^{\mathrm{miss}}$ is calculated using all calorimeter cells belonging to topological clusters. To account for muons, which only deposit a small fraction of their energy in the calorimeter, the muon momenta are added. To not double count energy, only the muon momenta measured using the stand-alone muon spectrometer reconstruction by *Muonboy*, is used. To reduce the contribution of fake muons a matched inner detector track is required.

To overcome the inefficiency of the muon spectrometer in the crack regions muons reconstructed by *CaloTrkMuId*-muons [1] within $0 < |\eta_\mu| < 0.1$ and *MuTag*-muons in $1.0 < |\eta_\mu| < 1.3$ respectively are taken into account.

Further a correction for the energy loss of particles in the cyrostat between the EM Calorimeter and the hadronic tile calorimeter is applied.

The final step of the $E_{\mathrm{T}}^{\mathrm{miss}}$ reconstruction is the refined calibration of the calorimeter cells. Each calorimeter cell is associated with a reconstructed high-p_T object. To resolve assignments to more than one object the association is done in a carefully chosen order, namely electrons, photons, muons, hadronically decaying τ-leptons, b-jets and light jets. The calibration of the calorimeter cells is then replaced by the corresponding calibration of the reconstructed high-p_T object. Cells belonging to topological cluster and not being associated to any object are calibrated using a global calibration scheme.

5.6   b-tagging Algorithms

The techniques to identify jets originating from b-quarks are commonly called *b-tagging* algorithms. These algorithms utilise the characteristic properties of heavy flavour hadrons. The most important characteristic is the long lifetime of B–hadrons of about 1.5 ps. This results in a long flight path and thus a measurable distance between the production and the decay of the B–hadrons.

Tracks originating from the B–hadron decay show a significant difference in the distribution of their impact parameter with respect to the primary vertex. The impact parameter is a signed quantity, measuring the distance of closest approach of the track to the vertex. The sign is chosen negative for tracks crossing the jet axis behind the primary vertex.

The *b-tagging* algorithm used in this analysis is a combination of an impact parameter based (IP3D) and an secondary vertex based algorithm (SV1).

IP3D calculates a jet weight using a likelihood ratio method utilising the longitudinal and the transverse projection of the impact parameter significance. The reference distributions are derived by Monte Carlo studies.

The SV1 algorithm fits the inclusive secondary vertex of the B–hadron decay, including the products of a possible charm hadron decay. A jet weight is calculated using discriminating variables like vertex mass, number of tracks of the vertex, energy fraction of the tracks fitted to the vertex to all tracks associated to the jet and angle between the jet axis and

the B–hadron flight direction.

Detailed information about the *b-tagging* algorithms and their performance can be found in [1, 54].

Chapter 6

Event Selection

The small cross section of the signal process is confronted with an enormous cross section of background processes. In order to select signal events with a high efficiency and simultaneously achieve a high background rejection, the event selection exploits the characteristic signature of the signal process:

- Two isolated leptons from the $H \to \tau\tau$ decay of opposite charge.

- Considerable amount of missing transverse energy caused by the neutrinos of the τ-lepton decays.

- Two jets with a large separation in pseudo-rapidity (tagging jets).

- Suppressed production of jets between the tagging jets.

Based on earlier studies [1, 55, 56] selection criteria are chosen and are used as input to a cut based event selection.

This chapter is organised as follows. The first section describes the reconstruction of the Higgs boson mass using the so-called collinear approximation. After this the event selection criteria and the applied selection cuts are introduced. Finally the results of the event selection are presented.

6.1   Mass Reconstruction

In the signal process four neutrinos originating from the τ-lepton decays are present. Since they escape the detection of the ATLAS detector the mass of the Higgs boson cannot be reconstructed using its decay products. However, using the following assumptions the τ-leptons, and hence the Higgs boson, can be reconstructed:

- The momentum of the τ-lepton and its decay products are parallel. This assumption is called collinear approximation. Since the Higgs boson has sufficient mass and transverse momentum, cf. Fig. 4.2a, its decay products are strongly boosted. In
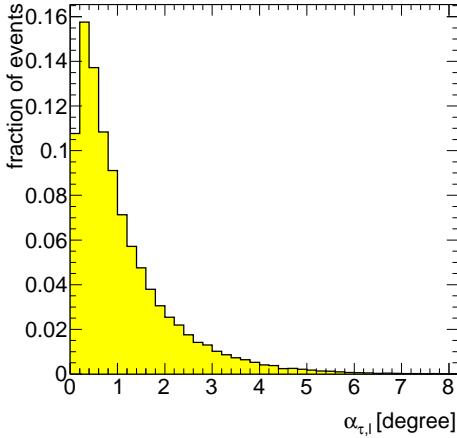
Figure 6.1: *Angle between the τ-lepton and its charged decay lepton for the signal process ($M_H = 120$ GeV).*
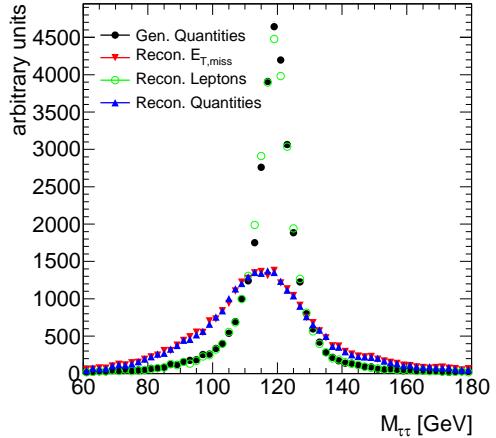
Figure 6.2: *Invariant di-τ-lepton mass $M_{\tau\tau}$ of a 120 GeV Higgs boson. $M_{\tau\tau}$ was reconstructed using the collinear approximation. To study the mass resolution generated momenta as well as reconstructed momenta are used as input to the mass calculation. The quantities $x_{1,2}$ are required to be in the range $0 \leq x_{1,2} \leq 1$*

Fig. 6.1 the angle between one of the τ-leptons and the lepton from its decay is shown. For 99% of the events the angle is smaller than 5° and thus is sufficiently small.

- The missing transverse energy is only produced by the neutrinos from the τ-lepton decays. Fig. 6.3 shows the difference in ϕ and in p_T between the generated missing transverse energy and the missing transverse energy caused by the four neutrinos of the τ-lepton decays. The deviations are caused by additionally neutrinos in the event.

- Since the momenta are higher than 10 GeV, the masses of muons and electrons can be safely neglected.

This method was first proposed in [57]. Using the assumptions above the only unknown parameters to reconstruct the τ-lepton momenta and hence the Higgs boson mass are the energies of the τ-leptons. In Fig. 6.4 a sketch of the Higgs boson decay in the transverse plane is shown. Momentum conservation in the transverse plane gives

$$\vec{p}_{T,\tau_1} + \vec{p}_{T,\tau_2} = \frac{\vec{p}_{T,lep_1}}{x_1} + \frac{\vec{p}_{T,lep_2}}{x_2} = \vec{p}_{T,lep_1} + \vec{p}_{T,lep_2} + \vec{E}_{T,miss} \tag{6.1}$$

x_1 and x_2 are the fractions of the lepton momentum to the corresponding τ-lepton momentum,

$$x_1 = \frac{E_{lep_1}}{E_{\tau_1}} \text{ and } x_1 = \frac{E_{lep_2}}{E_{\tau_2}} \ .$$
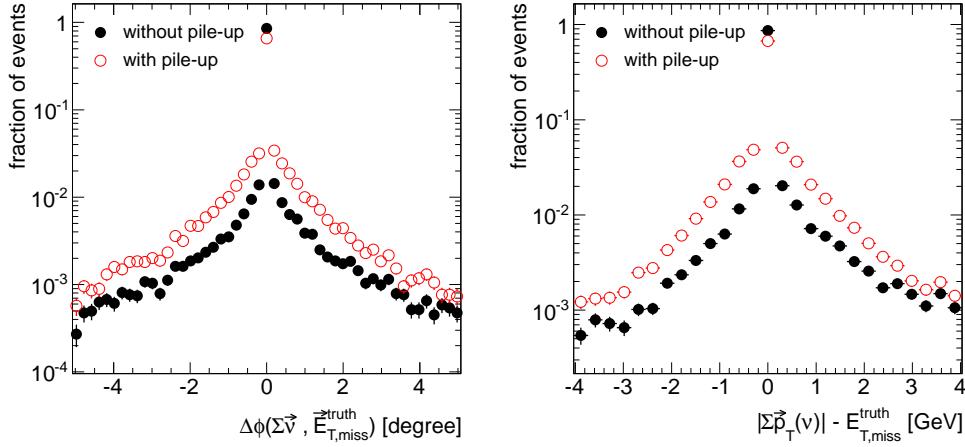
Figure 6.3: *Comparison between the sum of neutrinos $\sum_\nu \vec{p}_T$ from the Higgs boson ($M_H = 120\,\text{GeV}$) decay and the generated missing transverse energy $E_{\text{T,miss}}^{\text{truth}}$.*

Using equation 6.1 x_1 and x_2 can be calculated by:

$$x_1 = \frac{p_{x,lep_1}\,p_{y,lep_2} - p_{y,lep_1}\,p_{x,lep_2}}{p_{x,lep1}\,p_{y,lep_2} - p_{y,lep_1}\,p_{x,lep_2} + p_{y,lep_2}\,E_{x,miss} - p_{x,lep_2}\,E_{y,miss}}$$
$$x_2 = \frac{p_{x,lep_1}\,p_{y,lep_2} - p_{y,lep_1}\,p_{x,lep_2}}{p_{x,lep1}\,p_{y,lep_2} - p_{y,lep_1}\,p_{x,lep_2} + p_{x,lep_1}\,E_{y,miss} - p_{y,lep_1}\,E_{x,miss}} \tag{6.2}$$

As long as the lepton momenta are linearly independent ($\vec{p}_{T,lep_2} \neq \lambda \cdot \vec{p}_{T,lep_1}$), x_1 and x_2 can be solved unambiguously. Meaningful values of x_1 and x_2 are in the range from 0 to 1. Neglecting the mass of the τ-lepton, the invariant di-τ-lepton mass $M_{\tau\tau}$ is given by:

$$\begin{aligned} M_{\tau\tau}^2 &= (p_{\tau_1} + p_{\tau_2})^2 = 2(p_{\tau_1} \cdot p_{\tau_2} + m_\tau^2) \\ &\simeq \frac{M_{lep_1 lep_2}^2}{x_1 x_2} \ . \end{aligned} \tag{6.3}$$

The resolution of the reconstructed Higgs boson mass is dominated by the resolution of the reconstructed missing transverse energy. Fig. 6.2 compares the reconstructed mass using generated and reconstructed quantities for a simulated Higgs boson mass of $120\,\text{GeV}$. The quantities $x_{1,2}$ are required to be in the range $0 \leq x_{1,2} \leq 1$. Using the generated objects as input to the mass reconstruction results in a mass resolution of about $5\,\text{GeV}$. The impact of the lepton reconstruction on the mass resolution is small, whereas the reconstructed missing transverse energy decreases the resolution to about $12\,\text{GeV}$. Furthermore using reconstructed missing transverse energy shifts the $M_{\tau\tau}$ distribution to lower values by about $4\,\text{GeV}$. This shift is mainly caused by the displacement of the beam spot, which is not taken into account during calorimeter reconstruction. Switching the displacement off in the simulation removes the shift, cf. Fig 6.5.
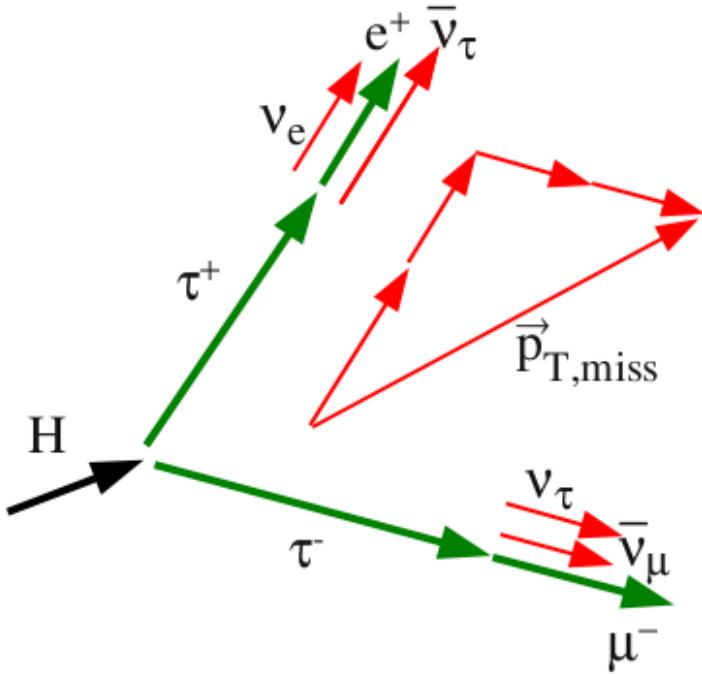
Figure 6.4: *Momentum diagram to illustrate the mass reconstruction using the collinear approximation. By decomposition of the missing transverse energy vector onto the lepton momentum vectors the τ-lepton momenta can be derived.*

6.2 Event Selection Criteria

The event selection is divided into two steps.

In the first step the physics objects, i.e. muons, electrons and jets, are selected. This is discussed in the first part of this section.

The selection criteria in the second step are focusing on the event topology. They are described in the second part of this section.

All distribution containing the signal process are derived using a generated Higgs boson mass of $M_H = 120\,\text{GeV}$.

The selection of the physics objects is based on recommendations of the ATLAS physics performance groups. For this reason they are excluded from the optimisation process. The selection criteria related to the event topology are optimised to give a good signal significance using $\frac{S}{\sqrt{B}}$ as a figure of merit. S and B denote the number of signal and background events in the mass window $105\,\text{GeV} < M_{\tau\tau} < 135\,\text{GeV}$. The selection criteria are optimised using the signal process and the background processes $Z \to ee$, $Z \to \mu\mu$, $Z \to \tau\tau \to \ell\ell + 4\nu$ and $t\bar{t}$ production. The optimisation was done using signal events generated with a Higgs boson mass of $M_H = 120\,\text{GeV}$. Due to the limited number of simulated events a *cut factorisation* method is used for the background processes $Z \to ee$, $Z \to \mu\mu$ and $t\bar{t}$ production. A detail description of the *cut factorisation* method is given in Section 6.3.

The background processes W+jets production and the di-boson production have been
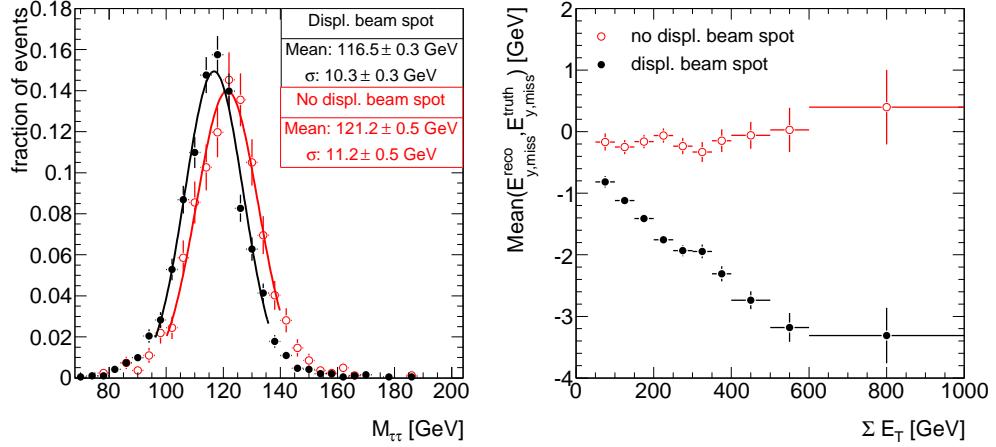
Figure 6.5: *Comparison of simulated Monte Carlo events with (black) and without (red) displaced beam spot using the process VBF $H \to \tau\tau \to \ell\ell + 4\nu$ ($M_H = 120\,\text{GeV}$) without pile-up. Left: invariant di-τ-lepton mass $M_{\tau\tau}$, right: mean value of $E_{y,miss}^{reco} - E_{y,miss}^{truth}$ depending on the total sum of E_T deposit in the calorimeter.*

ignored for the optimisation, because their contribution is expected to be small and the limited number of simulated events did not allow a estimation of the expected number of events in the mass window.

In the presence of pile-up the selection criteria related to the event kinematics have been re-optimized. Only three selection criteria have changed: central jet veto, missing transverse energy and the required separation of the tagging jets in pseudo-rapidity $\Delta\eta_{jj}$.

6.2.1 Pre-Selection

This pre-selection is only used for the comparisons shown in this chapter and is not part of the event selection.
Since all Monte-Carlo samples are filtered using different generator event filter, a meaningful comparison of the signal and background processes requires some pre-selection. Only a soft selection is chosen, because of the very limited event statistics. These selection requirements are:

- Exactly two reconstructed leptons ($e\mu, \mu\mu, ee$) with opposite charge and $p_T \geq 10\,\text{GeV}$ are required. Both are required to be isolated.

- At least two reconstructed jets with $p_T \geq 20\,\text{GeV}$ have to be found. The invariant mass M_{jj} of the two highest p_T jets has to be $M_{jj} > 300\,\text{GeV}$ and the jets need to be well separated $|\Delta\eta_{jj}| > 2.0$.

The detailed description of the selected objects are discussed in the following sections.
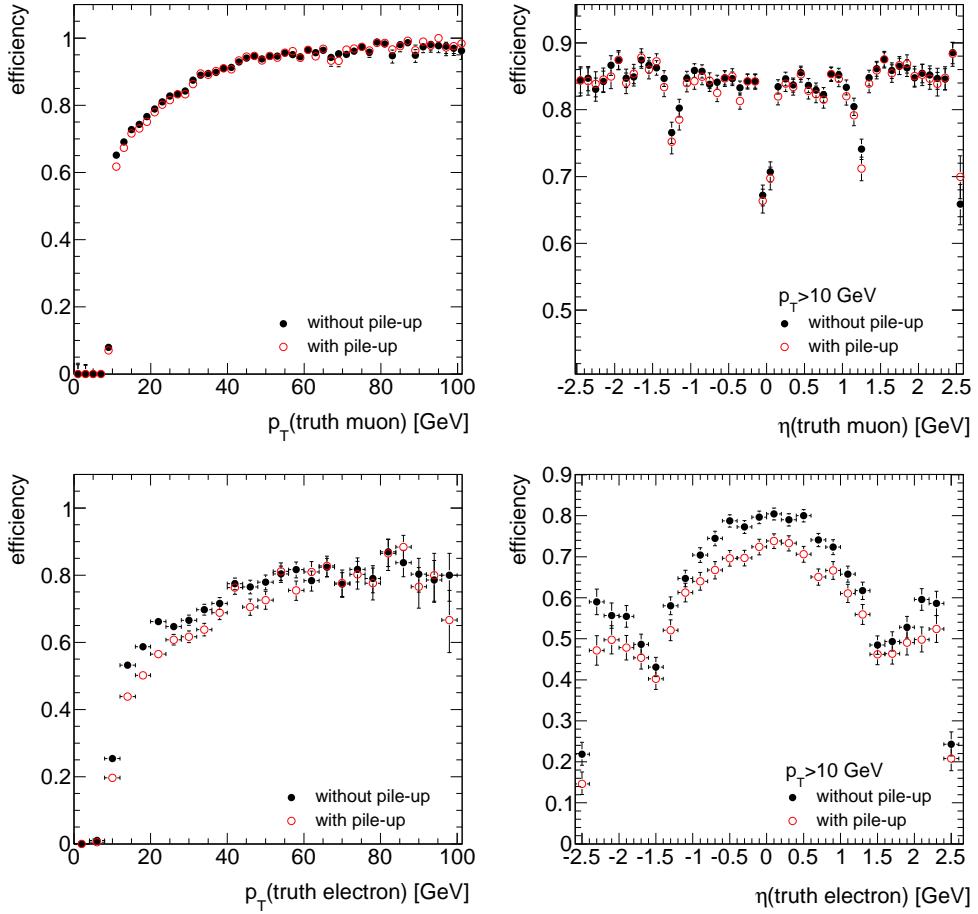
Figure 6.6: *Reconstruction and identification efficiency of muons and electrons without and with pile-up derived using the signal sample.*

6.2.2 Object Selection

Trigger and Lepton Selection:

The considered decay channel of the Higgs boson $H \rightarrow \tau\tau \rightarrow \ell\ell + 4\nu$ provides a clear signature with two isolated leptons[1] (electrons and muons) and missing transverse energy. The two leptons offer a good signature for the event trigger and allow the usage of single lepton as well as di-lepton triggers.
The following lepton triggers are used:

- A single electron trigger requiring an isolated electron of *medium* quality with $p_T \geq 25\,\text{GeV}$.

- A single muon trigger requiring an isolated muon with $p_T \geq 20\,\text{GeV}$.

---

[1]In this context the word lepton refers only to electrons and muons.

- A di-lepton trigger requiring two isolated electrons of *medium* quality with $p_T \geq 15\,\text{GeV}$.

- A di-lepton trigger requiring two isolated muons with $p_T \geq 10\,\text{GeV}$.

The event is selected if at least one of the trigger requirements is fulfilled. A mixed electron-muon trigger is not provided by the trigger simulation and therefore is not used.

Only muons and electrons fulfilling the following selection requirements are used:

Muon selection: Only muon candidates having at least a transverse momentum of $p_T \geq 10\,\text{GeV}$ are used. They are required to be combined muons having an inner detector and a muon spectrometer track. The χ^2_{match} of the combination of the inner detector track and the track reconstructed in the muon spectrometer is required to be $\chi^2_{match} < 100$, cf. Section 5.2. The muons need to be well isolated, which means that the summed E_T in the calorimeter in a radius ΔR of 0.2 around the muon is less than 10% of the muon p_T.

Electron selection: Only *medium* class electrons with a transverse momentum of at least $p_T \geq 10\,\text{GeV}$ are considered. Like in the muon selection an isolation condition is required: the summed E_T in the calorimeter in a radius ΔR of 0.2 around the electron is less than 10% of the electron p_T.

To reduce the number of background events only events with exactly two reconstructed leptons are retained. These leptons are required to be of opposite charge.
The applied transverse momentum requirement on the leptons is adapted depending on the fulfilled trigger requirement:

- double muon: two muons with $p_T \geq 15\,\text{GeV}$.

- double electron: two electrons with $p_T \geq 15\,\text{GeV}$.

- single muon: one muon with $p_T \geq 20\,\text{GeV}$.

- single electron: one electron with $p_T \geq 25\,\text{GeV}$.

The requirements are tested in the given order. If more than one trigger requirement is fulfilled, only one of the conditions needs to be satisfied.

Fig. 6.6 shows the overall reconstruction and identification efficiency of the leptons of the $H \rightarrow \tau\tau \rightarrow \ell\ell + 4\nu$ decay without and with pile-up. The efficiency is defined as :

$$\text{efficiency} = \frac{\text{number of reconstructed muons (electrons) matched to a truth muon (electron)}}{\text{number of truth muons (electrons)}}\,.$$

The reconstructed electrons and muons have to fulfil the requirements discussed above. Only the truth electrons and muons from the $H \rightarrow \tau\tau \rightarrow \ell\ell + 4\nu$ are considered. They are matched to the reconstructed ones, if the distance ΔR is less than 0.1. The efficiency for muons shows only little influence with pile-up, whereas the efficiency for electrons is degraded. The shape of the efficiency distribution depending on η is strongly influenced

by the structure of the ATLAS detector. The drop of the reconstruction and identification efficiency of electrons at $|\eta| \approx 1.5$ coincides with the transition region of the EM barrel calorimeter to the EM end-cap calorimeter. For the muons the drops of the efficiency are caused by the gap in the muon spectrometer at $\eta = 0$, which is used for detector services, and the detector support structure at $\eta = 1.2$.

Jet selection:

In the signal process the Higgs boson is accompanied by two jets called tagging jets. Therefore only events with at least two reconstructed jets are selected, N(jets)$\geq$ 2. The jets are required to have at least a transverse momentum of $p_\mathrm{T} > 20\,\mathrm{GeV}$. The jets are reconstructed using the seeded fixed cone jet finder (see Section 5.4) using a cone size of $\Delta R = 0.4$. The tagging jets have a considerable amount of transverse momentum in contrast to the jets contained in $Z \to \tau\tau$ QCD and $t\bar{t}$ background processes. For this reason the tagging jets are chosen as the two jets with the highest transverse momentum. The
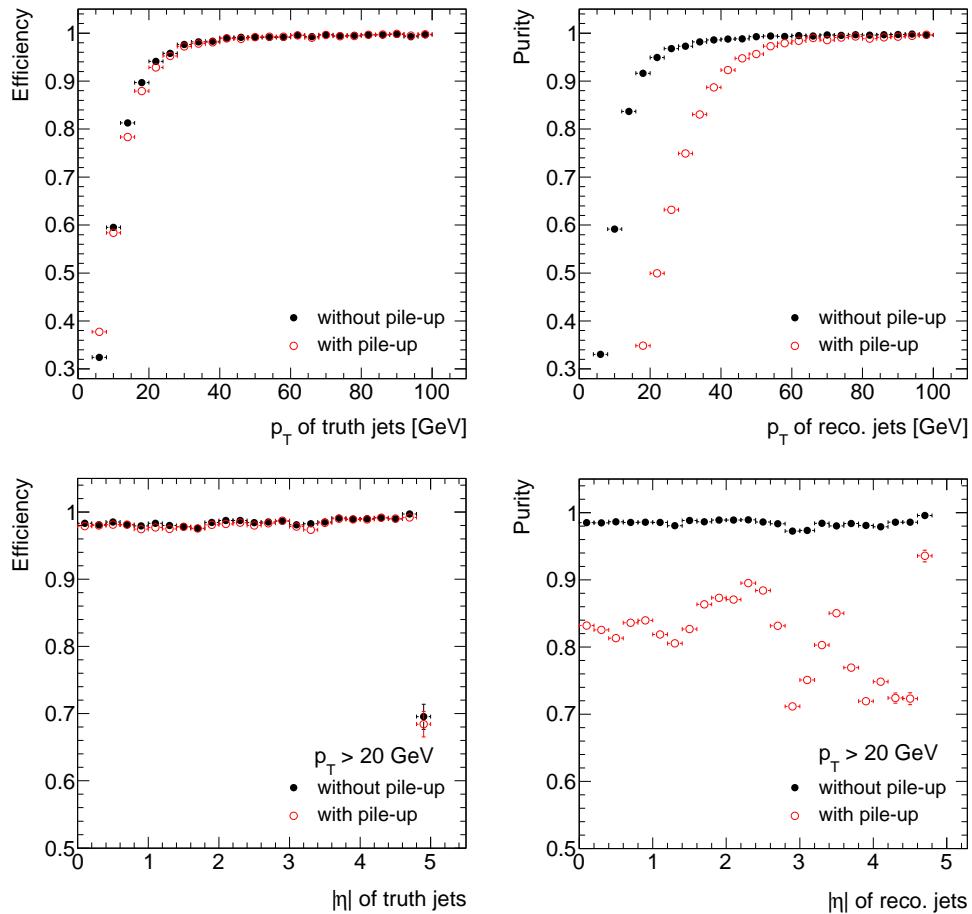
Figure 6.7: *Efficiency and purity for jets reconstructed using the cone jet algorithm for signal Monte Carlo sample with and without pile-up.*

leading jet should have a $p_T > 40\,\mathrm{GeV}$, whereas the second leading jet is required to have $p_T > 20\,\mathrm{GeV}$. Both jets should lie within $|\eta| < 4.8$.

Taking pile-up into account the jet multiplicity increases. For a comparison the jet multiplicity for the signal process without and with pile-up is shown in Fig. 6.12.

The jet identification efficiency is only little influenced by pile-up, contrary to the purity, cf. Fig. 6.7. The efficiency is defined as the fraction of truth jets found at the reconstruction level, and purity as the fraction of reconstructed jets that have a corresponding truth jet:

$$\text{Efficiency} \quad = \frac{\text{number of reconstructed jets matched to a truth jet}}{\text{number of truth jets}} \qquad (6.4)$$

$$\text{Purity} \quad = \frac{\text{number of reconstructed jets matched to a truth jet}}{\text{number of reconstructed jets}} \qquad (6.5)$$

In this context truth jets are defined as the jets create by the jet algorithm running on stable particles on the generator level, excluding muons and neutrinos.

In order to calculate the efficiency and purity the truth and reconstructed jets are matched to each other by requiring that the distance ΔR between a pair is less than $\Delta R < 0.25$. The matching is done in a p_T ordered way starting with the reconstructed jet of highest p_T. Every truth jet and every reconstructed jet can only be matched once. The efficiency and purity are calculated with respect to truth jets from the main interaction which do not take into account the true particles from the pile-up simulation.

The additional energy depositions due to pile-up do not degrade the jet identification, therefore the identification efficiency is almost not affected by pile-up. On the other hand jets, in particular with low transverse momentum, produced by the additional proton-proton interactions emerge. This effect reduces the purity significantly.

As a consequence pile-up has almost no affect on the reconstruction efficiency of the tagging jets, while the chance of selecting the correct tagging jets is reduced due to the higher number of jets.

Overlap Removal:

The ATLAS reconstruction software does not consider ambiguities, which means that an object can be reconstructed more than once. For example the energy depositions of an electron in the calorimeter may lead to its reconstruction as electron, but it can also be recognised as a jet by the jet finding algorithms. These ambiguities are removed by requiring a separation in space between the objects. Possible overlap is resolved in the following order of priority: muons, electrons, jets. The overlap between muons and electrons are removed using $\Delta R(e, \mu) > 0.1$; between jets and electrons (muons) a separation of $\Delta R(jet, e) > 0.2$ ($\Delta R(jet, \mu) > 0.2$) is required.

6.2.3 Event Topology Criteria

Tagging Jet Kinematics:

The scattered partons which form the tagging jets preferably have a large gap in pseudo-rapidity. Jets produced in QCD processes are primarily lying in the central region of the
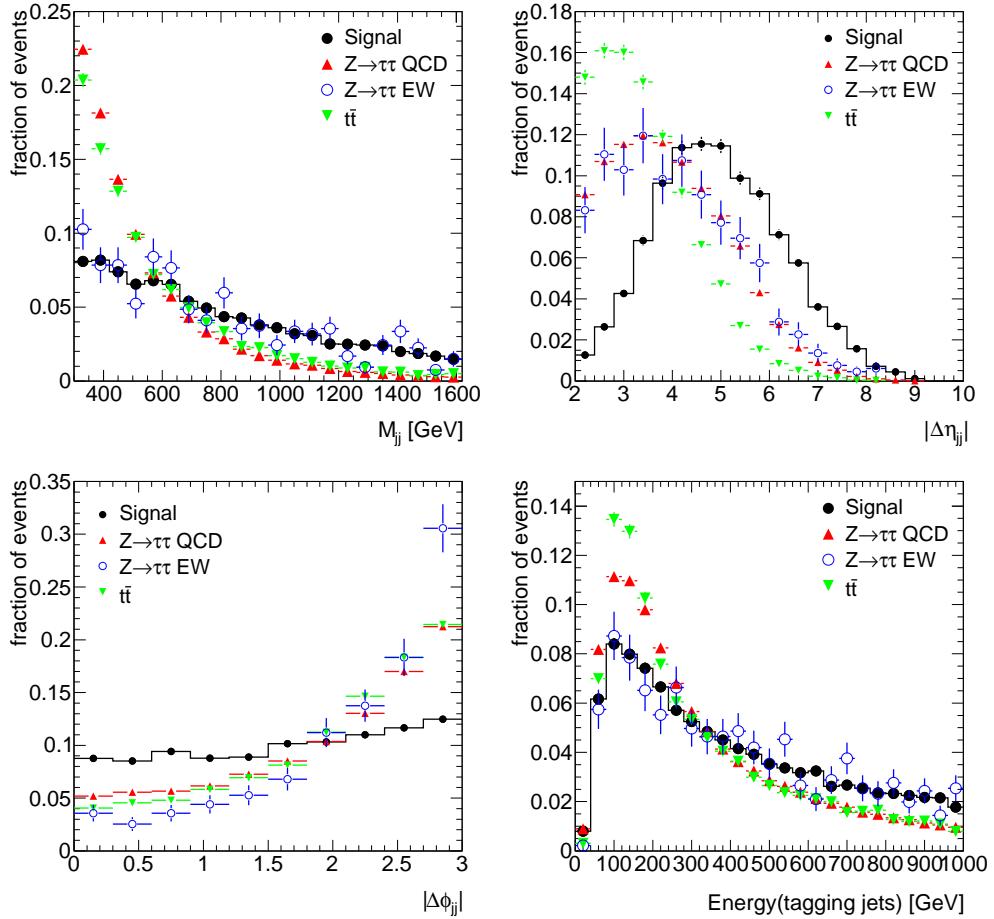
Figure 6.8: *Distributions of discriminating variables of the tagging jets: top left: invariant di-jet mass M_{jj}, top right: distance in pseudo-rapidity $|\Delta\eta_{jj}|$, bottom left: azimuthal angle $|\Delta\phi_{jj}|$, bottom right: energy of the tagging jets. The distributions are derived using the simulated events without pile-up.*

detector. Therefore tagging jets are required to be in different pseudo-rapidity hemispheres ($\eta_{j1} \times \eta_{j2} < 0$) and are well separated in pseudo-rapidity, $|\Delta\eta_{jj}| > 3.6$, cf. Fig. 6.8. In the presence of pile-up the optimal selection criteria is $|\Delta\eta_{jj}| > 3.2$.

Furthermore the tagging jets, lying often in the forward region of the detector, usually have a large energy which leads to a high invariant di-jet mass M_{jj}, cf. Fig. 6.8. M_{jj} is required to be $M_{jj} > 600 GeV$.

Further background rejection is achieved by requiring the ϕ separation of the tagging jets, cf. Fig. 6.8. It is required to be $|\Delta\phi_{jj}| < 2.5$. The same selection criteria of M_{jj} and $\Delta\phi_{jj}$ are used in the presence of pile-up.

b-jet Veto:

The $t\bar{t}$ background process is characterised by the production of two b-jets originating from the top quark decays, while the signal process contains almost no b-quarks and therefore
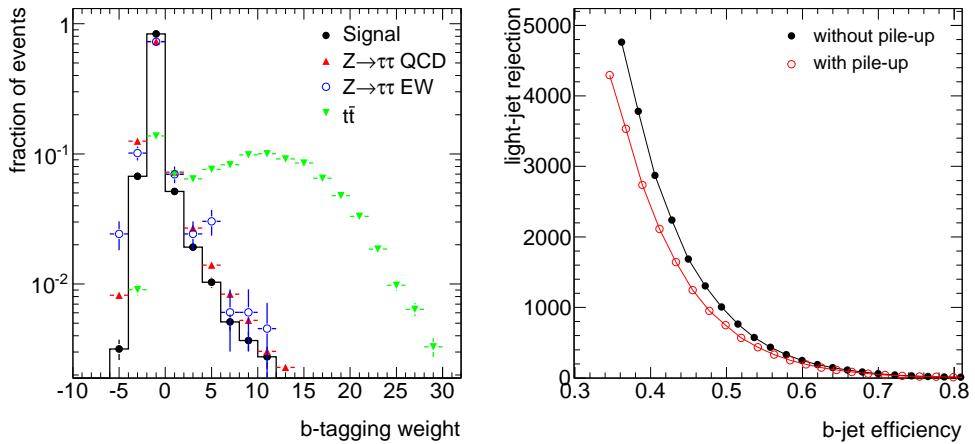
Figure 6.9: *Left: comparison of the b-jet weight distribution of the most probable b-jet per event for the signal and background Monte Carlo samples without pile-up. Right: comparison of b-tagging efficiency and light jet rejection for the $t\bar{t}$ Monte Carlo sample with and without pile-up. The b-tagging efficiency and light jet rejection are evaluated starting from $b_{weight} = -1.5$ to $b_{weight} = 9$ in steps of 0.5.*

no b-jets. Rejecting events which contain jets tagged as b-jets suppress the $t\bar{t}$ background contribution. Fig. 6.9 shows the weight distribution of the most likely b-jet in an event. Events containing a jet with a b-tagging weight of $b_{weight} > 4$ are rejected. This corresponds to a b-tagging efficiency of $b_{eff.} = 59\%$, while the light jet rejection[2] is 295 determined using the $t\bar{t}$ Monte Carlo dataset. The b-tagging efficiency and the light jet rejection are determined with respect to jets lying within $|\eta| < 2.5$. They are evaluated using the $t\bar{t}$ background process.

In the presence of pile-up the b-tagging efficiency $b_{eff.} = 57\%$ decreases while the light jet rejection of 295 is the same. The performance of the b-tagging algorithm with and without pile-up are compared in Fig. 6.9. The b-tagging efficiency and light jet rejection are evaluated starting from $b_{weight} = -1.5$ to $b_{weight} = 9$ in steps of 0.5.

Since the b-tagging requirement is rather loose, i.e. a high b-tagging efficiency is chosen, the selection requirement in the case of pile-up is not changed.

Central Jet Veto:

The absence of colour exchange between the scattered partons in the signal process leads to a suppressed production of jets between the tagging jets. In contrast, jets originating from QCD processes are enhanced in the central region of the detector, cf. Fig. 6.10. By vetoing any additional jet to the tagging jets reconstructed with $p_T > 20\,\text{GeV}$ in $|\eta| < 3.2$ a good background suppression is achieved.

The central jet veto suffers from the large increase of the jet multiplicity due to pile-up, cf. Fig. 6.12. To obtain a better signal selection efficiency, jets originating from pile-up have

---

[2]The light jet rejection is defined as the inverse of the fraction of true light-jets that are falsely tagged as b-jets.
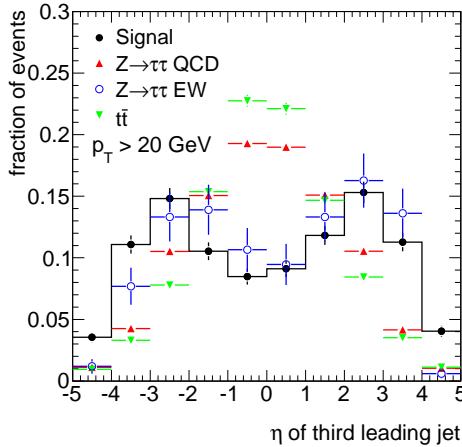
Figure 6.10: *Comparison of the pseudo-rapidity distribution of the third leading jet for the signal and background Monte Carlo samples without pile-up.*

to be excluded from the jet veto. This is achieved by using the jet vertex tool [58].

The interaction vertices of the additional minimum bias interactions are usually displaced from the primary vertex. The jet vertex tool makes use of the charged particle content of jets that leave tracks in the inner detector. Tracks are assigned to jets, if they are pointing towards the jet area. On the other hand, each track is assigned to a vertex by the vertex reconstruction algorithm. In this way the jets are associated to the interaction vertices. To discriminate jets originating from pile-up the quantity jet-vertex-fraction (JVF) is used. The JVF is defined as:

$$\text{JVF} = \frac{\sum p_\text{T} \text{ of tracks assigned to the jet and to the primary vertex}}{\sum p_\text{T} \text{ of tracks assigned to the jet}} \quad .$$

The jet-vertex-fraction is required to be JVF > 0.8, as proposed in [58]. This method is limited in pseudo-rapidity to the range $|\eta| < 2.5$ since inner detector tracks are needed. The impact of pile-up on the central jet veto can be minimised by limiting it to the range $|\eta| < 2.5$.

The performance of the central jet veto without and with pile-up is compared in Fig. 6.11. The signal and background efficiencies are evaluated for different jet p_T thresholds, starting from 20 GeV to 45 GeV in steps of 5 GeV. The $t\bar{t}$ background and $Z \to \tau\tau$ QCD background are considered separately. Using the jet vertex tool the signal selection efficiency improves a lot, whereas the background rejection decreases, cf. Fig. 6.11.

The central jet veto is applied as follows:

Without pile-up: reject event, if an additional jet to the tagging jets with $p_\text{T} > 20$ GeV in $|\eta| < 3.2$ is found.

With pile-up: reject event, if an additional jet to the tagging jets with JVF > 0.8, $p_\text{T} > 20$ GeV in $|\eta| < 2.5$ is found.
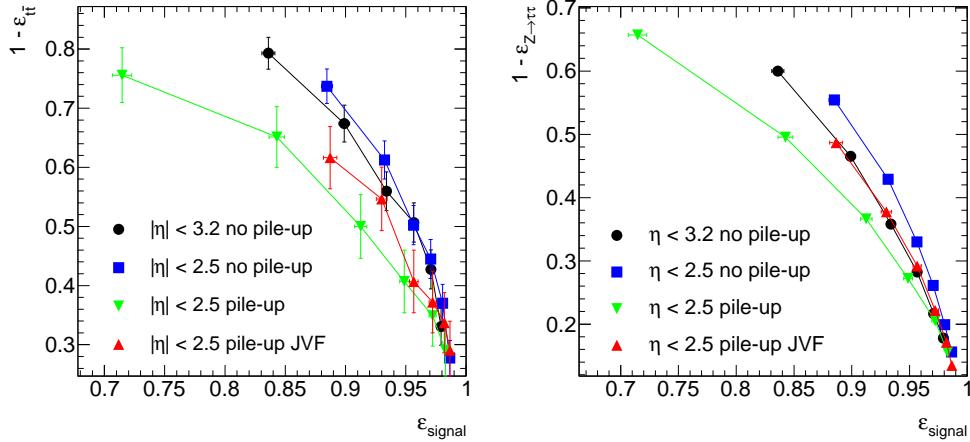
**Figure 6.11:** *Comparison of signal efficiency versus $t\bar{t}$ (left) and $Z \to \tau\tau$ QCD (right) background efficiency of the central jet veto with and without pile-up. The efficiencies have been evaluated for different jet p_T thresholds, starting from $20\,\mathrm{GeV}$ to $45\,\mathrm{GeV}$ in steps of $5\,\mathrm{GeV}$.*

Missing Transverse Energy:

Due to the four neutrinos in the final state the signal process has a large amount of missing transverse energy E_T^{miss}. Since E_T^{miss} is used in the mass reconstruction a precise measurement is of large importance. Fig. 6.13 shows the E_T^{miss} distribution for the signal and background processes. Requiring $E_T^{\mathrm{miss}} > 40\,\mathrm{GeV}$ provides a good background suppression. Especially backgrounds like $Z \to ee$ and $Z \to \mu\mu$ are suppressed since the measured E_T^{miss} is expected to be small and solely caused by the finite detector resolution and coverage. The additional minimum bias interactions have a large impact on the resolution of the E_T^{miss} measurement. In Fig. 6.14 the resolution of the reconstructed missing transverse energy as a function of the total transverse momentum $\sum p_T$ is shown for the signal sample. Due to pile-up the resolution increases by about $6\,\mathrm{GeV}$. The degradation of the resolution in the presence of pile-up is caused by the large total transverse momentum which is uncorrelated with the total transverse momentum of the main process. In the case of pile-up the requirement on the missing transverse energy is increased to $E_T^{\mathrm{miss}} > 45\,\mathrm{GeV}$.

Lepton Kinematics:

To further suppress the background processes the properties of the τ-lepton decay products are used. As can be seen in Fig. 6.16 the invariant di-lepton mass M_{ll} provides a good background suppression. Especially $Z \to ee$, $Z \to \mu\mu$ and $t\bar{t}$ processes are suppressed by requiring $M_{ll} < 80\,\mathrm{GeV}$. Furthermore the requirement $M_{ll} > 30\,\mathrm{GeV}$ is applied. Due to the large transverse momentum of the Higgs boson the leptons are boosted into the direction of the Higgs boson. Therefore they are not that much separated in ϕ as the background processes, cf. Fig. 6.15. Furthermore events with large separation in ϕ show a worse mass resolution using the collinear approximation. For this reasons the requirement $|\Delta\phi_{\ell\ell}| < 2.2$ is used.
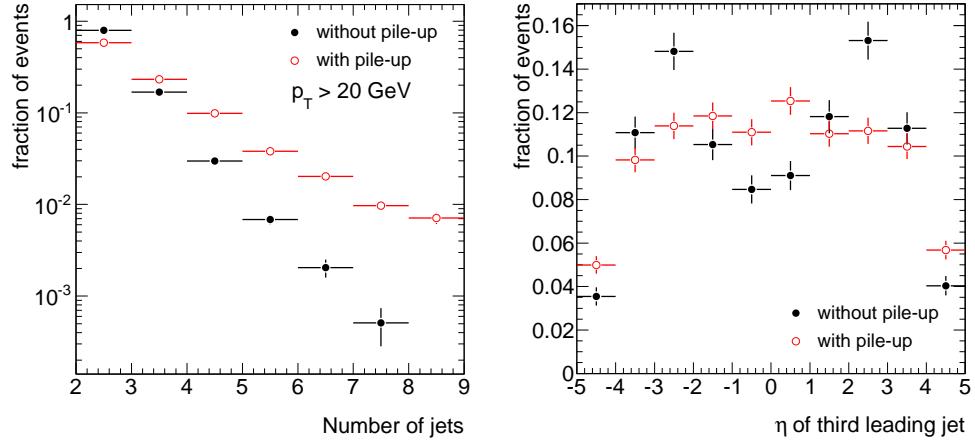
Figure 6.12: *Comparison of number of jets with $p_T > 20\,\mathrm{GeV}$ and η_j of third leading jet for the signal Monte Carlo sample with and without pile-up.*
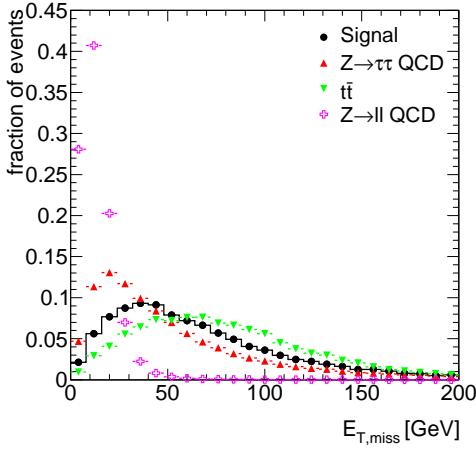

Figure 6.13: *Comparison of missing transverse energy for signal and background processes without pile-up.*

Since the decay products of the Higgs boson lie in the central region of the detector n whereas the tagging jets are predominantly in the forward and backward region, it is required that the leptons are between the tagging jets in pseudo-rapidity, $\min(\eta_{j1}, \eta_{j2}) < \eta_\ell < \max(\eta_{j1}, \eta_{j2})$. This requirement is referred to as centrality.

Further the lepton and the tagging jets should be well separated. This leads to the selection criteria $|\Delta\eta_{j,\ell}| > 0.7$ applied to all lepton - tagging jet combinations.

In the presence of pile-up the same selection criteria as without considering pile-up effects are used.
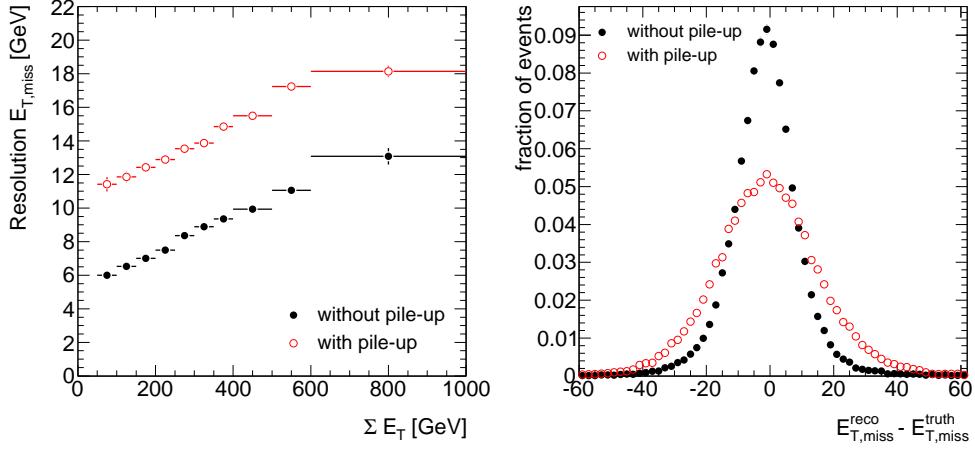
Figure 6.14: *Comparison of the missing transverse energy of the signal process without and with pile-up. Left: resolution of the reconstructed E_T^{miss} depending on the total sum of transverse energy in the calorimeter, right: distribution of the difference between the reconstructed E_T^{miss} and the E_T^{miss} calculated using generated particles.*
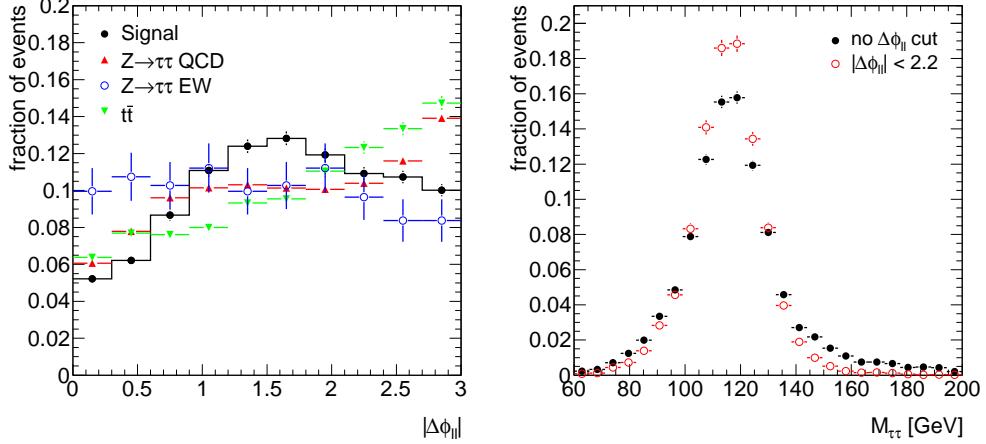
Figure 6.15: *Comparison of ϕ separation of the leptons for signal and background processes without pile-up. Events with a large separation in ϕ show a worse mass resolution.*

Collinear Approximation:

As has been discussed in Section 6.1, the mass of the Higgs boson can be reconstructed using the collinear approximation. During this procedure the variables x_1 and x_2 are calculated, which represent the momentum fraction of the lepton from the τ-lepton decay to the corresponding τ-lepton. Not considering the used approximations and detector resolution effects physically meaningful values are in the range $0 \leq x_{1,2} \leq 1$. A comparison of $x_{1,2}$ for signal and background processes show that these quantities are useful to suppress backgrounds where the selected leptons and the missing transverse momentum do not originate from τ-lepton decays, cf. Fig. 6.17. A good background suppression is achieved
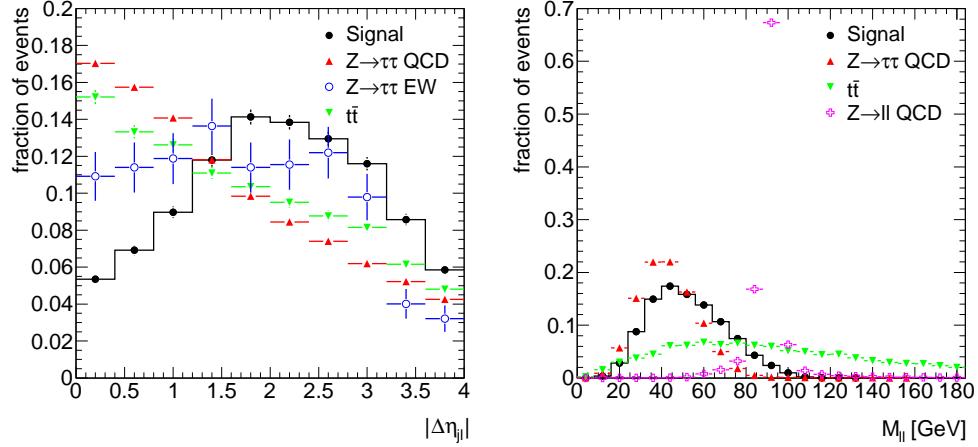
Figure 6.16: *Distribution of discriminating variables of the leptons. Left: separation in pseudo-rapidity between leptons and tagging jets, right: invariant di-lepton mass. The distributions are derived using the signal sample without pile-up.*

using the selection $0 \leq x_{1,2} \leq 1$. The same requirements are used in the presence of pile-up.

As the resolution of the reconstructed $E_{\mathrm{T}}^{\mathrm{miss}}$ is degraded by pile-up the distribution of x_1 and x_2 changes. For this reason pile-up has a large impact on the invariant di-τ-lepton mass $M_{\tau\tau}$, c.f. Fig. 6.18. The $M_{\tau\tau}$ distribution in Fig. 6.18a are derived requiring in addition to the pre-selection the requiement $0 \leq x_{1,2} \leq 1$. After the application of all selection criteria the resolution of the reconstructed mass is about $10\,\mathrm{GeV}$ without pile-up and about $14\,\mathrm{GeV}$ with pile-up, cf. Fig. 6.18b.
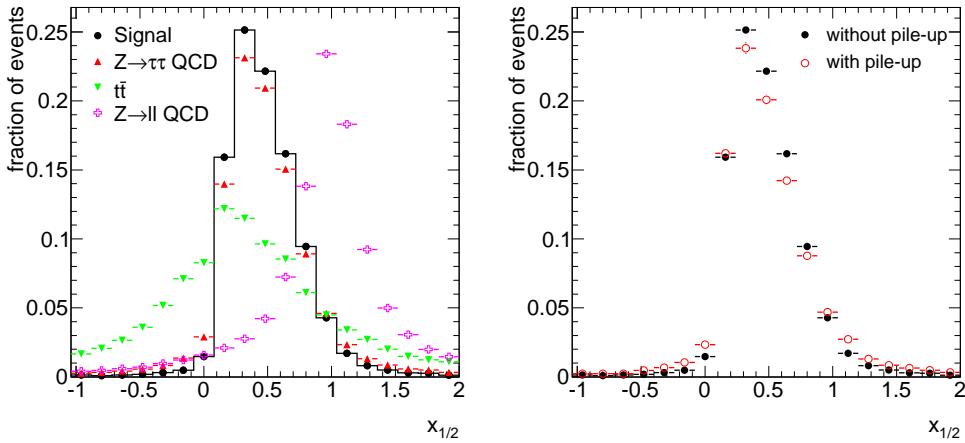
Figure 6.17: *Comparison of the quantities $x_{1,2}$ for signal and background processes without pile-up. On the right $x_{1,2}$ are compared for the signal process with and without pile-up.*
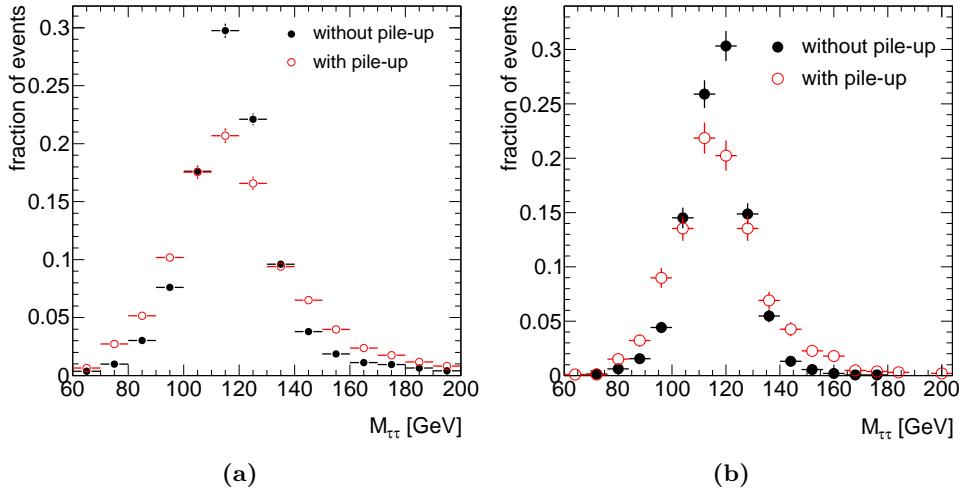
Figure 6.18: *Comparison of the Higgs boson mass $M_{\tau\tau}$ calculated using the collinear approximation for the signal process with and without pile-up. $x_{1,2}$ are required to be in the range $0 \leq x_{1,2} \leq 1$. Left: after the application of the pre-selection criteria, right: after the application of all selection criteria.*

6.3 Cut Factorisation

The high rejection rate of the presented selection criteria ensures that only a few tens of background events are expected at an integrated luminosity of $30\,\mathrm{fb}^{-1}$ of data. Since the number of simulated Monte Carlo events for the background processes W+jets, $Z \to \mu\mu$, $Z \to ee$, di-boson and especially $t\bar{t}$ is limited, the prediction of these backgrounds has to be approximated using a cut factorisation method. For this the selection criteria are arranged into three groups that are preferably uncorrelated. The first group contains requirements related to jets (jet transverse momentum, di-jet mass, jet separation, b-jet veto, central jet veto). The second group is related to the Higgs boson decay products (lepton separation, lepton centrality, di-lepton mass, missing transverse energy, collinear approximation). In the third group are the common object selection criteria that are required to apply the requirements belonging to the other groups.

The background rejection of the total event selection is estimated by the product of the rejection rates of each individual group. The rejection rates for group one and two are determined with respect to group three.

The cut factorisation method neglects correlations between the different selection criteria groups. In order to estimate the expected uncertainty of this approximation method and hence for the background prediction, the cut factorisation procedure was applied to the signal sample as well as the $Z \to \tau\tau \to \ell\ell + 4\nu$ sample. The comparison of the number of events surviving all selection requirements to that using cut factorisation shows a discrepancy of 20% using the signal process and of 10% using the $Z \to \tau\tau \to \ell\ell + 4\nu$ process. In both cases the cross sections predicted using cut factorisation are smaller.

6.4 Shape Parametrisation

As mentioned earlier only a small amount of events are left after the application of the selection requirements. As a consequence the $M_{\tau\tau}$ shape after all selection cuts is affected by large statistical uncertainties. Since the $M_{\tau\tau}$ shapes of the signal and background processes are derived from Monte Carlo simulation and serve as probability distributions for the event expectations they are smoothed using parametrisation functions. The parametrisations are fitted using a maximum likelihood fit, except of the $Z \to \tau\tau$ events. For these a χ^2 fit is used, because the histogram contains weighted events.

Shape Parametrisation for $H \to \tau\tau$ and $Z \to \tau\tau$

The choice of parametrisation functions is mainly driven by the choices taken in [1]. The shape of the $M_{\tau\tau}$ distribution for signal and $Z \to \tau\tau$ background events is very similar. In both cases the τ-leptons emerge from the decay of a resonance. Since $M_{\tau\tau}$ is reconstructed using the collinear approximation its shape is dictated by the kinematics of its ingredients, the momenta of the two leptons and $E_{\mathrm{T}}^{\mathrm{miss}}$. The width of the $M_{\tau\tau}$ distribution is dominated by the resolution of the $E_{\mathrm{T}}^{\mathrm{miss}}$ reconstruction. To account for these properties the $M_{\tau\tau}$ distribution is described by a double Gaussian with identical mean. The applied selection criteria, especially the requirement on the visible momentum fraction $x_{1/2}$, introduce an asymmetry in the $M_{\tau\tau}$ distribution. This asymmetry is modelled using the Gaussian error function erf. Thus, the $M_{\tau\tau}$ shape is parametrised by:

$$
\begin{aligned}
F_Z(M_{\tau\tau}; m, \sigma_1, \sigma_2, &m_{asym}, \sigma_{asym}, f_{g1}) = \left(\frac{1}{2} + \frac{1}{2} \cdot erf\left(\frac{M_{\tau\tau} - m_{asym}}{\sqrt{2}\sigma_{asym}} \right) \right) \\
&\times \left(f_{g1}\, e^{(M_{\tau\tau}-m)^2/2\sigma_1^2} + (1 - f_{g1})\, e^{(M_{\tau\tau}-m)^2/2\sigma_2^2} \right).
\end{aligned}
\tag{6.6}
$$

f_{g1} is the relative contribution of the first Gaussian. For the signal process the $M_{\tau\tau}$ distribution after all selection requirements is used for parametrisation.
Because of the low number of $Z \to \tau\tau$ events surviving all selection criteria, the $M_{\tau\tau}$ distribution at an earlier cut stage is used for the fit. In particular the requirement of the lepton centrality and the central jet veto are omitted, since they show only a small influence on the $M_{\tau\tau}$ distribution. This has been tested by comparing the $M_{\tau\tau}$ distribution after a basic selection to the $M_{\tau\tau}$ distribution and in addition either the central jet veto or the centrality requirement, cf. Fig. 6.19. The agreement has been is confirmed using a Kolmogorov test, which results in a value of 0.9 for the centrality and of 0.4 for the central jets veto.
The basic selection contains the requirements: object selection (cf. 6.2.2, tagging jet selection, $E_{\mathrm{T}}^{\mathrm{miss}} > 40\,\mathrm{GeV}$, $|\Delta\phi_{\ell\ell}| < 2.2$, $30\,\mathrm{GeV} < M_{\ell\ell} < 80\,\mathrm{GeV}$, $|\Delta\phi_{jj}| < 2.5$ and $0 \le x_{1,2} \le 1$.
The $M_{\tau\tau}$ distribution of the electro-weak and the QCD part of the $Z \to \tau\tau$ background are in good agreement, cf. 6.20. For the comparison the selection criteria $\Delta\phi_{jj}$ and the central jet veto are omitted. The good agreement has been tested using a Kolmogorov test, which results in a value of 0.97. For this reason the same parametrisation is used for both.

Fig. 6.21 shows the parametrisation function fitted to the signal events and to the $Z \to \tau\tau$ events. Table 6.1 shows the values of the function parameters, which fit best. In the case of

the signal events the broader $M_{\tau\tau}$ distribution with pile-up is described by an increase of the width of the two Gaussian distributions. Instead in the $Z \to \tau\tau \to \ell\ell + 4\nu$ background process the broader $M_{\tau\tau}$ distribution is achieved increasing the relative contribution of the Gaussian distribution with the large width.
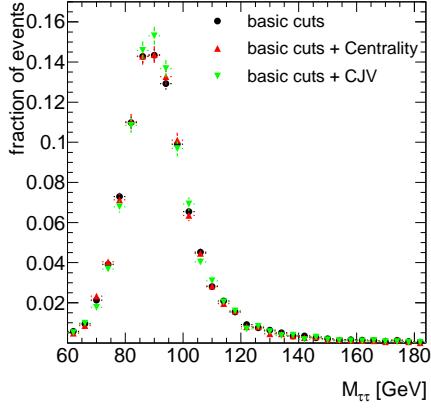

Figure 6.19: *Comparison of the $M_{\tau\tau}$ distribution of the $Z \to \tau\tau \to \ell\ell + 4\nu$ QCD background without pile-up. Black filled circles: $M_{\tau\tau}$ distribution after the application of a basic selection (see text), red up-pointing triangles: $M_{\tau\tau}$ distribution after the application of the basic selection and in addition the centrality requirement, green down-pointing triangles: $M_{\tau\tau}$ distribution after the application of the basic selection and in addition the central jet veto.*
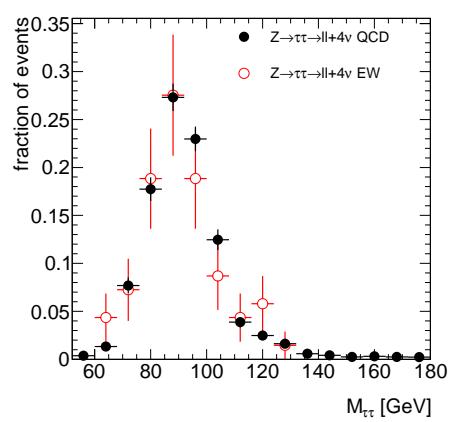
Figure 6.20: *Comparison of the $M_{\tau\tau}$ distribution of the electro-weak and QCD part of the $Z \to \tau\tau \to \ell\ell + 4\nu$ background. Due to the limited number of Monte Carlo events the selection criteria $\Delta\phi_{jj}$ and the central jet veto have not been applied. The good agreement has been verified using a Kolmogorov test, which results in a value of 0.97.*

Fit-parameter	$H \to \tau\tau \to \ell\ell + 4\nu$ $M_H = 120\,\text{GeV}$				$Z \to \tau\tau \to \ell\ell + 4\nu$			
	without pile-up		with pile-up		without pile-up		with pile-up	
m	116.5	$\pm$ 0.3	110.8	$\pm$ 4.8	88.4	$\pm$ 2.1	90.1	$\pm$ 0.9
σ_1	9.3	$\pm$ 0.50	14.8	$\pm$ 1.3	10	$\pm$ 0.7	13.6	$\pm$ 1.3
σ_2	18.8	$\pm$ 2.3	34.3	$\pm$ 3.7	32	$\pm$ 5	34.9	$\pm$ 4.9
m_{asym}	71.4	$\pm$ 4.9	97	$\pm$ 22	68	$\pm$ 11	62.5	$\pm$ 2.3
σ_{asym}	5.1	$\pm$ 4.0	22	$\pm$ 10	14.5	$\pm$ 7.3	5.8	$\pm$ 2.5
f_{g1}	0.80	$\pm$ 0.08	0.78	$\pm$ 0.08	0.88	$\pm$ 0.04	0.78	$\pm$ 0.07

Table 6.1: *Values of the parameter used for the parametrisation of the $M_{\tau\tau}$ shape for the signal and background process.*

Shape Parametrisation for $t\bar{t}$ Background

The shape of the $t\bar{t}$ background is parametrised by the convolution of a single sided decay function with a Gaussian:

$$F_{t\bar{t}}(M_{\tau\tau}; \tau, \mu, \sigma) = \left(e^{-y/\tau} * G(y, \mu, \sigma)\right)(M_{\tau\tau}). \qquad (6.7)$$
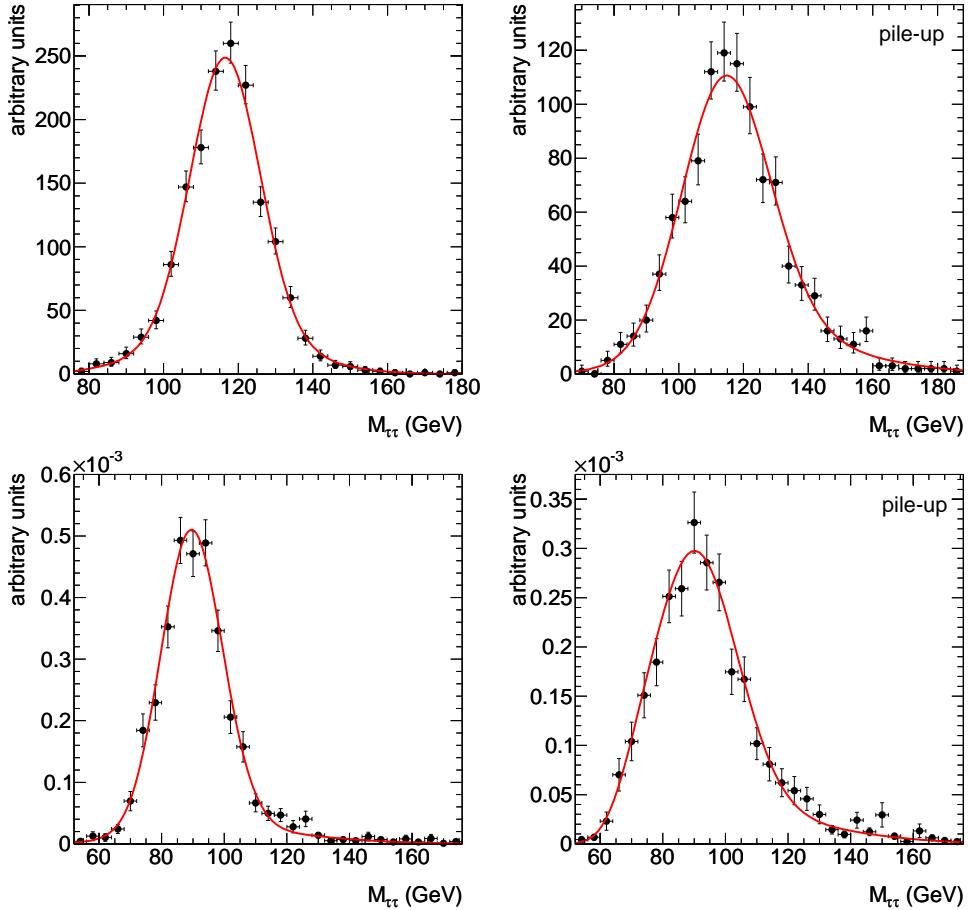
Figure 6.21: $M_{\tau\tau}$ *distribution and fitted parametrisation for signal events (top) and $Z \to \tau\tau$ events (bottom). To determine the parametrisation function of the $Z \to \tau\tau$ events selection criteria with minor influence on the shape are omitted, see text.*

The strong limitation of the number of Monte Carlo events does not permit the derivation of the parametrisation function after all selection criteria. In order to get a reliable parametrisation the shape of the $M_{\tau\tau}$ distribution is evaluated at an earlier cut stage. To minimise the influence of the omitted requirements, the selection criteria are arranged by decreasing influence on the shape of the $M_{\tau\tau}$ distribution. To identify the requirements with minor influence, the change of the shape of the $M_{\tau\tau}$ distribution is evaluated for each requirement after a basic selection. The basic selection requires: exactly two identified leptons of opposite charge with $p_T > 10\,\text{GeV}$, exactly two identified jets with $p_T > 20\,\text{GeV}$, $0 \leq x_{1,2} \leq 1$. Finally the selection criteria: Trigger, M_{jj}, $\Delta\eta_{jj}$, $\Delta\eta_{jl}$ and the Central Jet Veto are omitted. In addition the requirement that the tagging jets are in different pseudo-rapidity hemispheres is omitted.

The $M_{\tau\tau}$ distribution and its fitted parametrisation function are shown in Fig. 6.22. The values of the parameters, which fit best are shown in Table 6.2. Only small differences between the parametrisations with and without pile-up are observed. The large uncertainties in the case of pile-up are a result of the lower number of Monte Carlo events, cf. Table 4.3.
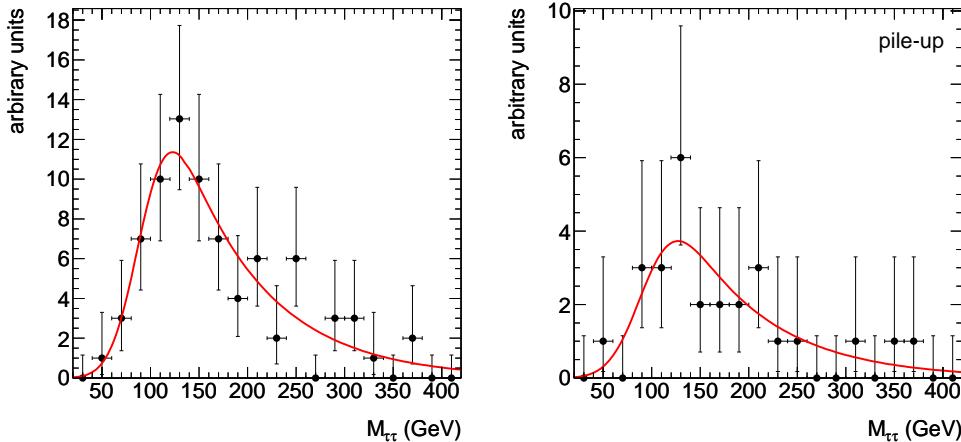
Figure 6.22: *$M_{\tau\tau}$ distribution and its fitted parametrisation for $t\bar{t}$ event. To determine the parametrisation function selection criteria with minor influence on the shape are omitted.*

Fit-parameter	without pile-up			with pile-up		
μ	91.3	$\pm$	7.9	90	$\pm$	13
σ	24.2	$\pm$	6.3	26	$\pm$	10
τ	86	$\pm$	16	88	$\pm$	28

Table 6.2: *Values of the parameter used for the parametrisation of the $M_{\tau\tau}$ shape for the $t\bar{t}$ process.*

6.5 Results of the Event Selection

Without Pile-Up

Table 6.3 gives the result of the event selection applied to the signal Monte-Carlo samples with different mass assumptions. Only the statistical uncertainties are given. Assuming a dataset that corresponds to an integrated luminosity of $30\,\mathrm{fb}^{-1}$ about 20 events are expected of which 16 are in the given mass window assuming $M_H = 120\,\mathrm{GeV}$. Due to the decreasing production cross section and branching ratio the number of expected $H \to \tau\tau$ events decreases as well with higher masses M_H.

Table 6.4 shows the expected background cross sections after the event selection. As expected $Z \to \tau\tau \to \ell\ell + 4\nu$ is the main background process. A fraction of about 12% are due to the electro-weak $Z \to \tau\tau \to \ell\ell + 4\nu$ background. About 51 $Z \to \tau\tau \to \ell\ell + 4\nu$ events are expected assuming a dataset that corresponds to an integrated luminosity of $30\,\mathrm{fb}^{-1}$. The background with the second highest contribution is $t\bar{t}$ with about 14 expected events. In the mass window $105\,\mathrm{GeV} < M_{\tau\tau} < 135\,\mathrm{GeV}$ about 5 $Z \to \tau\tau \to \ell\ell + 4\nu$ and about 3 $t\bar{t}$ events are expected. These numbers are derived using parametrised $M_{\tau\tau}$ shapes normalised to expected number of events. The calculation of the quantity $\frac{S}{\sqrt{B}}$ in the given mass range is $\frac{S}{\sqrt{B}} = 5.6$. Background processes of minor importance are the $Z \to \ell\ell$, W+jets and di-boson processes. Although cut factorisation is applied, none of the available W+jets Monte Carlo events survive all selection criteria. For this reason a

Mass [GeV]	$H \to \tau\tau \to \ell\ell + 4\nu$			
	115	120	125	130
Cross section [fb]	22.63	20.39	17.98	15.31
Object selection cuts:				
Trigger	14.25	13.10	11.68	10.21
N(lepton) = 2	6.51	6.20	5.50	4.92
Lepton charge	6.49	6.18	5.48	4.91
Trigger lepton	6.27	5.99	5.32	4.76
Tagging jet selection	3.73	3.54	3.17	2.78
Lepton cuts:				
$30\,\text{GeV} < M_{\ell\ell} < 80\,\text{GeV}$	3.27	3.04	2.69	2.32
$|\Delta\phi_{\ell\ell}| < 2.2$	2.35	2.13	1.81	1.55
$E_\text{T}^\text{miss} > 40\,\text{GeV}$	1.93	1.77	1.57	1.37
Collinear Approx.	1.76	1.62	1.43	1.27
Jet cuts:				
$|\Delta\eta_{jj}| > 3.6$	1.35	1.26	1.10	0.98
$M_{jj} > 600\,\text{GeV}$	1.10	1.05	0.92	0.82
$|\Delta\phi_{jj}| < 2.5$	0.97	0.93	0.83	0.75
Centrality	0.95	0.91	0.81	0.72
$|\Delta\eta_{j\ell}| > 0.7$	0.86	0.80	0.72	0.64
b-jet veto	0.84	0.78	0.70	0.63
Central jet veto	0.70 ± 0.02	0.66 ± 0.02	0.61 ± 0.03	0.54 ± 0.02
Mass window cut:				
$M_{\tau\tau}$ in $M_H \pm 15\,\text{GeV}$	0.58 ± 0.02	0.54 ± 0.01	0.46 ± 0.02	0.42 ± 0.02

Table 6.3: *Accepted signal cross section after each selection step. The cross sections are given in fb. The selection requirements are applied to signal Monte Carlo samples assuming various Higgs boson masses without pile-up. Only the statistical uncertainties are quoted. The given cross sections include already the event filter efficiency.*

limit on the cross section corresponding to a 95% confidence level according to the Poisson distribution is given. Due to limited amount of Monte Carlo events their contribution is difficult to estimate, which results in a large uncertainty on the cross section after all selection requirements. Furthermore no shape of the $M_{\tau\tau}$ distribution of these background processes could be estimated.

With Pile-Up

Table 6.5 gives the result of the event selection applied to the signal Monte-Carlo samples with different mass assumptions with pile-up. About 16 events are expected assuming a dataset that corresponds to an integrated luminosity of $30\,\text{fb}^{-1}$. 10 of these events are in the given mass window assuming $M_H = 120\,\text{GeV}$. Even though the selection criteria are optimised, pile-up leads to a loss of signal efficiency of about 20% after the central jet veto requirement. Due to the much broader $M_{\tau\tau}$ distribution (cf. Fig. 6.17) the loss of expected signal events in the mass window is even more dramatic and about 40%.

| | $Z \to \tau\tau \to \ell\ell + 4\nu$ | | $t\bar{t}$ | $Z \to \ell\ell$ | W+jets | di-boson |
	QCD	EW		QCD	QCD	
Cross section [fb]	1906	1794	467300	94960	1154600	174100
Object selection cuts:						
Trigger	1163	288	231300	84500	609900	35000
N(lepton) $= 2$	609	25	24450	49000	466	4540
Lepton charge	608	24	23830	48800	290	4390
Trigger Lepton	571	23	23610	48700	281	4380
N(jets) ≥ 2	452	21	22170	36100	191	1860
Tagging jet selection	220	8	9450	16170	78	560
Lepton cuts:						
$30\,\mathrm{GeV} < M_{\ell\ell} < 80\,\mathrm{GeV}$	191	7	3206	920	43	93
$|\Delta\phi_{\ell\ell}| < 2.2$	130	5	2425	572	39	72
$E_\mathrm{T}^\mathrm{miss} > 40\,\mathrm{GeV}$	86	3	1916	17	14	50
Collinear Approx.	71	3	221	4.73	2	4.1
Jet cuts:						
$|\Delta\eta_{jj}| > 3.6$	23.2	1.1	33.4*	1.92*	0.65*	1.04*
$M_{jj} > 600\,\mathrm{GeV}$	11.8	1.0	19.2*	0.66*	0.34*	0.63*
$|\Delta\phi_{jj}| < 2.5$	8.74	0.61	12.3*	0.40*	0.10*	0.54*
Centrality	6.48	0.57	8.8*	0.30*	0.10*	0.40*
$|\Delta\eta_{j\ell}| > 0.7$	4.05	0.48	5.4*	0.20*	0.10*	0.39*
b-jet veto	3.89	0.46	1.9*	0.20*	0.10*	0.39*
Central jet veto	1.51 ± 0.05	0.20 ± 0.05	0.45 ± 0.07*	0.06 ± 0.01*	< 0.11*	0.19 ± 0.21*

Table 6.4: *Accepted background cross sections after each selection step. The cross sections are given in fb. The selection requirements are applied to background processes without pile-up. Caution must be take at the numbers derived with only a few requirements, since the cross sections are derived using Monte Carlo events which passed an event filter (see Chapter 4). The limit corresponds to a 95% confidence level according to the Poisson distribution. An asterisk is used to indicate cross sections estimated using the cut factorisation method. Only the statistical uncertainties are given.*

	$H \to \tau\tau \to \ell\ell + 4\nu$			
Mass [GeV]	115	120	125	130
Cross section [fb]	22.63	20.39	17.98	15.31
Object selection cuts:				
Trigger	13.07	12.12	10.90	9.55
N(lepton) = 2	5.37	5.16	4.58	4.12
Lepton charge	5.35	5.15	4.56	4.11
Trigger Lepton	5.18	5.00	4.43	3.99
N(jets) $\geq$ 2	4.31	4.09	3.65	3.25
Tagging jet selection	3.26	3.07	2.77	2.43
Lepton cuts:				
$30\,\text{GeV} < M_{\ell\ell} < 80\,\text{GeV}$	2.85	2.64	2.35	2.00
$|\Delta\phi_{\ell\ell}| < 2.2$	2.04	1.87	1.58	1.34
$E_{\text{T}}^{\text{miss}} > 45\,\text{GeV}$	1.52	1.43	1.27	1.06
Collinear Approx.	1.27	1.18	1.07	0.91
Jet cuts				
$|\Delta\eta_{jj}| > 3.2$	1.07	0.99	0.89	0.76
$M_{jj} > 600\,\text{GeV}$	0.84	0.79	0.71	0.61
$|\Delta\phi_{jj}| < 2.5$	0.74	0.70	0.64	0.55
Centrality	0.72	0.68	0.62	0.52
$|\Delta\eta_{j\ell}| > 0.7$	0.64	0.60	0.54	0.46
b-jet veto	0.63	0.59	0.54	0.45
Central jet veto	0.56±0.02	0.52±0.02	0.48±0.02	0.40±0.01
Mass window cut:				
$M_{\tau\tau}$ in $M_H \pm 15\,\text{GeV}$	0.37±0.02	0.33±0.01	0.32±0.02	0.25±0.01

Table 6.5: *Accepted signal cross section after each selection step. The cross sections are given in fb. The selection requirements are applied to signal Monte Carlo samples assuming various Higgs boson masses with pile-up. Only the statistical uncertainties are quoted. The given cross sections include already the event filter efficiency.*

Table 6.4 shows the expected background cross sections after the event selection. The $Z \to \tau\tau \to \ell\ell + 4\nu$ process is the main background and of approximately the same size as without pile-up. Unfortunately, no electro-weak $Z \to \tau\tau \to \ell\ell + 4\nu$ Monte Carlo events with pile-up were available. Assuming that the electro-weak $Z \to \tau\tau \to \ell\ell + 4\nu$ background are influenced in the same way by pile-up as the QCD $Z \to \tau\tau \to \ell\ell + 4\nu$ background it is estimated using the relative fraction from the none pile-up case. This means it is of the order of 12% of the QCD $Z \to \tau\tau \to \ell\ell + 4\nu$ background. Using this assumption about 51 $Z \to \tau\tau \to \ell\ell + 4\nu$ events are expected. In the mass range $105\,\text{GeV} < M_{\tau\tau} < 135\,\text{GeV}$ the estimated background is almost twice as large as without pile-up, which means about 9 events are expected. This effect is caused on the grounds of the worse resolution of the reconstructed mass. The contribution from the $t\bar{t}$ background is slightly increased to about 16 expected events. In the mass window $105\,\text{GeV} < M_{\tau\tau} < 135\,\text{GeV}$ about 3 $t\bar{t}$ events are expected, which is the same as without pile-up. The calculation of the quantity $\frac{S}{\sqrt{B}}$ in the given mass range is $\frac{S}{\sqrt{B}} = 2.9$. When considering pile-up the background processes

$Z \to \ell\ell$, W+jets and di-boson are still of minor importance. Due to the limited amount of Monte Carlo events their contribution is difficult to estimate, which results in a rather large uncertainty on the cross section after all selection requirements. Furthermore no shape of the $M_{\tau\tau}$ distribution of these background processes could be estimated.

Comparison of $M_{\tau\tau}$ Distributions

Figure 6.23 shows the expected $M_{\tau\tau}$ distribution for an integrated luminosity of $30\,\mathrm{fb}^{-1}$ assuming $M_H = 120\,\mathrm{GeV}$. Only the signal and main background processes are considered. The histograms are stacked.

The signal events are on the right tail of the $Z \to \tau\tau$ background. In the case without pile-up the signal peak can be distinguished from the $Z \to \tau\tau$ background. Since the $t\bar{t}$ background events show a rather flat $M_{\tau\tau}$ distribution it is of less importance compared to $Z \to \tau\tau$. For higher masses of the Higgs boson this changes.

Due to pile-up the shape of the $M_{\tau\tau}$ distribution of the signal and the $Z \to \tau\tau$ background gets much broader. In particular the resolution of the mass reconstruction increases roughly from $10\,\mathrm{GeV}$ to $14\,\mathrm{GeV}$. The signal peak can only hardly be distinguished from the $Z \to \tau\tau$ background and is spread over the whole falling shoulder.

For this reason a precise knowledge of the $M_{\tau\tau}$ shape of the $Z \to \tau\tau$ background is very important.
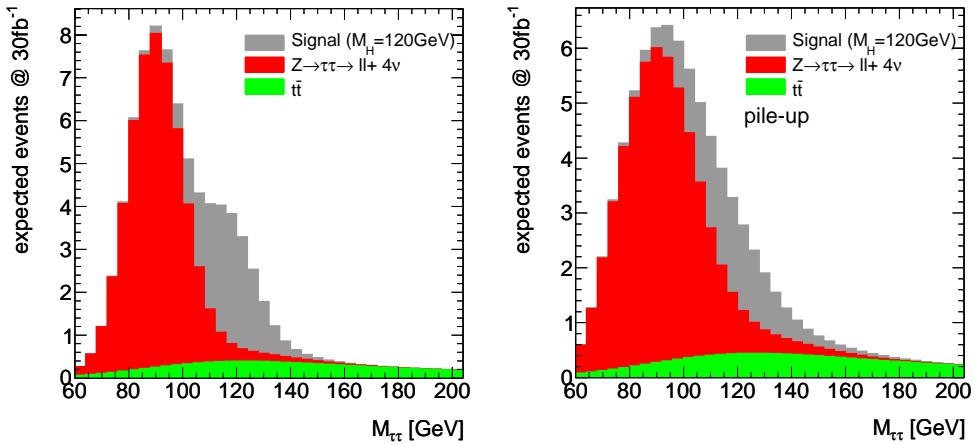
Figure 6.23: *Expected $M_{\tau\tau}$ distribution for the signal ($M_H = 120\,\mathrm{GeV}$) and the main background processes for an integrated luminosity of $30\,\mathrm{fb}^{-1}$ without (left) and with (right) pile-up. The histograms are stacked. The shapes are derived using the parametrisation functions.*

6.6 Summary

In this chapter the event selection used in the VBF $H \to \tau\tau \to \ell\ell + 4\nu$ analysis has been discussed. The selection requirements are optimised separately with and without pile-up. As expected, $Z \to \tau\tau \to \ell\ell + 4\nu$ and $t\bar{t}$ are the main background processes. Comparing the results of the event selection without pile-up to the results of the selection proposed in [1],

	Z → ττ → ℓℓ + 4ν QCD	tt̄	Z → ℓℓ QCD	W+jets QCD	di-boson
Cross section [fb]	1906	467300	94960	1154600	174100
Object selection cuts:					
Trigger	1060	213600	80640	542900	31800
N(lepton) = 2	490	21800	43550	417	3910
Lepton charge	488	21230	43380	264	3750
Trigger Lepton	462	21000	43270	256	3750
N(jets) ≥ 2	395	20100	35770	188	2020
Tagging jet selection	189	8723	15580	71	589
Lepton cuts:					
30 GeV < $M_{\ell\ell}$ < 80 GeV	188	2020	872	28	103
$|\Delta\phi_{\ell\ell}|$ < 2.2	111	2184	537	25	89
E_T^{miss} > 45 GeV	67	1626	36	12	58
Collinear Approx.	49	179	4.8	1.7	3.3
Jet cuts:					
$|\Delta\eta_{lj}|$ > 3.2	21.2	41.5*	1.7*	0.74*	1.38*
M_{jj} > 600 GeV	10.5	19.5*	0.69*	0.16*	0.57*
$|\Delta\phi_{jj}|$ < 2.5	7.78	12.7*	0.40*	0.16*	0.40*
Centrality	5.44	8.56*	0.29*	0.16*	0.29*
$|\Delta\eta_{j\ell}|$ > 0.7	3.31	4.78*	0.19 *	0.16*	0.23*
b-jet veto	3.15	1.63*	0.18*	0.16*	0.23*
Central jet veto	1.49 ± 0.06	0.53 ± 0.09*	0.06 ± 0.01*	0.03 ± 0.04*	0.03 ± 0.03*

Table 6.6: *Accepted background cross sections after each selection step. The cross sections are given in fb. The selection requirements are applied to background processes with pile-up. Caution must be take at the numbers derived with only a few requirements, since the cross sections are derived using Monte Carlo events which passed an event filter (see Chapter 4). An asterisk is used to indicate cross sections estimated using the cut factorisation method. Only the statistical uncertainties are given.*

an increase in the signal efficiency of about 20% is observed. The contribution of the $t\bar{t}$ background is reduced to about $\frac{1}{3}$ compared with the results of [1]. This is mainly achieved by introducing the selection criteria on the quantities $M_{\ell\ell}$ and $\Delta\eta_{j\ell}$. The contribution of the $Z \to \tau\tau \to \ell\ell + 4\nu$ background is of the same order as the results of [1].

In the presence of pile-up the signal efficiency decreases by 20%, whereas the background contribution is almost the same. This effect is mainly caused by the degraded resolution of the reconstructed missing transverse energy, which in addition leads to a broader $M_{\tau\tau}$ distribution. The $M_{\tau\tau}$ spectra of the signal and the $Z \to \tau\tau \to \ell\ell + 4\nu$ background overlap, making the signal extraction more difficult.

For this reasons a significant loss of the signal sensitivity in the presence of pile-up is observed.

Chapter 7

Background Estimation using Data

The precise knowledge of the background processes is crucial for this analysis. Typically the background contamination is estimated based on Monte Carlo simulated events. The discriminating variable used for the observation is $M_{\tau\tau}$ calculated via the collinear approximation, which is very sensitive to the missing transverse energy E_T^{miss}. E_T^{miss} is difficult model using simulated events, because its measurement is sensitive to several effects, as e.g. instrumental effects, jet energy mis-measurements and pile-up.

As studies performed at the TEVATRON accelerator show, a precise description of the event kinematic of the production of the Z boson in association with jets using current Monte Carlo simulations is difficult [59]. Furthermore the description of the underlying-event[1] with Monte Carlo generators is affected by uncertainties.

In addition to that the Monte Carlo generation and detector simulation of events, in particular the $t\bar{t}$ events, is computationally very expensive. The production of a sufficient number of Monte Carlo events, corresponding to an integrated luminosity much larger than the integrated luminosity of the data, is difficult.

For these reasons the background estimation should not entirely rely on Monte Carlo simulated events. The extraction of the background contamination from data is preferred.

The methods described in the following are used to estimate the dominant background processes $Z \to \tau\tau$ and $t\bar{t}$. They rely on the selection of control samples giving a precise description of the shape of the $M_{\tau\tau}$ distributions of the corresponding background process.

7.1   Estimation of $t\bar{t}$ Background

To estimate the $t\bar{t}$ background contribution a control sample with a similar $M_{\tau\tau}$ shape is selected by using the analysis cuts with inverted b-jet veto. This procedure was first studied in [60].

---

[1]The underlying-event refers to the interaction of the proton remnants of the protons taking part in the interaction of interest (*hard interaction*). The proton remnants are connected to the partons of the *hard interaction* via the colour charge. This needs to be considered in the initial and final state radiation. The underlying-event process is dominated by QCD processes with low energetic particles.

As described in Chapter 6.2 the b-jet veto is used to suppress the $t\bar{t}$ background. The impact of the b-jet veto on the other background processes is rather small. Inverting the b-jet veto, i.e. requiring at least one tagged b-jet, selects mainly $t\bar{t}$ events. The application of the additional analysis cuts ensures the suppression of other background processes than the $t\bar{t}$ production.

To legitimate this method the following assumptions have to be tested.

- The shape of the $M_{\tau\tau}$ distribution is independent of the identification of b-jets.

- The contribution of other processes than $t\bar{t}$ process is negligible in the control sample.

- The control sample contains a number of $t\bar{t}$ events to provide a reliable estimation of the $t\bar{t}$ background process.

The first item is discussed in the next section. The last two items are discussed in Section 7.1.2.

7.1.1   Validation using Monte Carlo Simulation

The assumption that the shape of the $M_{\tau\tau}$ distribution is independent of the identification of b-jets needs to be verified in order to validate the $t\bar{t}$ control sample. For this two samples are selected, only differing in applying the b-jet veto or the b-jet requirement. The b-jet requirement means that at least one jet with a b-tagging weight of $b_{weight} > 4$ is found. Since the number of available Monte Carlo events is very limited only basic selection cuts are applied: two identified leptons with opposite charge and the variables $x_{1,2}$ are required to be $0 \leq x_{1,2} \leq 1$.

Fig. 7.1 shows the b-tagging identification efficiency depending on the transverse momentum and pseudo-rapidity of the jet. A different event kinematic is favoured by requiring a b-jet than by applying the b-jet veto. For example the b-tagging efficiency for high-p_T jets is higher than for low-p_T jets and therefore the relative fraction of events with b-jets with high p_T is larger in the control sample. The selection of a different event kinematic is further enhanced because b-jets can only be identified within $|\eta| < 2.5$.

Comparing certain distributions of kinematic variables of jets and leptons the different event kinematics become visible, cf. Fig. 7.2. Nevertheless the method can be used if the $M_{\tau\tau}$ distribution is independent of the b-jet identification. In Figure 7.3 the shapes of the $M_{\tau\tau}$ distributions of $t\bar{t}$ events with at least one identified b-jet is compared to events with no identified b-jets. For the comparison the cuts object selection, $0 \leq x_{1,2} \leq 1$, N(jets)≥ 2 are required. Both distributions are in good agreement which is confirmed by a Kolmogorov test resulting in the values 0.82 without pile-up and 0.8 with pile-up.

To verify whether the limitation of b-jet identification to $|\eta| < 2.5$ has any impact on the $M_{\tau\tau}$ distribution, the $t\bar{t}$ events are divided into the categories two, one and no b-jets within $|\eta| < 2.5$. For this separation the information of the generated particles are used. The number of events in the category no b-jets within $|\eta| < 2.5$ is too small for a meaningful comparison. The shape of the $M_{\tau\tau}$ distribution for the sub-samples one and two b-jets within $|\eta| < 2.5$ are compared in Fig. 7.4. For this comparison the cuts: object selection,
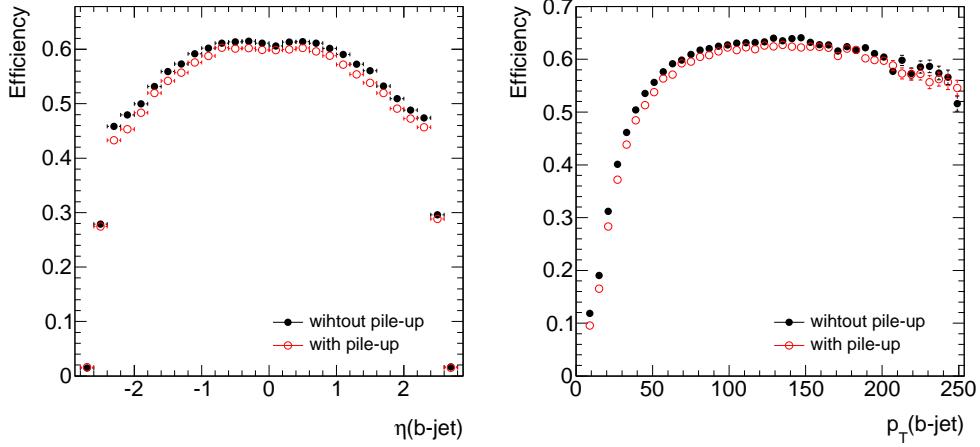
Figure 7.1: *Efficiency of finding a b-jet depending on pseudo-rapidity and transverse momentum for a b-weight greater than 4.*

$0 \leq x_{1,2} \leq 1$, N(jets)≥ 2 and $E_{\mathrm{T}}^{\mathrm{miss}} > 20\,\mathrm{GeV}$ are required. The values of a Kolmogorov test are 0.25 without pile-up and 0.29 with pile-up, that shows that both distributions are in good agreement.

To verify whether the application of the selection cuts has any impact on the agreement of the $M_{\tau\tau}$ distributions, a comparison between events without tagged b-jets and with tagged b-jets is done for each cut, cf. Figures 7.5 and 7.6. In this comparison a basic selection (containing the cuts: object selection, $0 \leq x_{1,2} \leq 1$, N(jets)≥ 2) is applied and in addition a different single cut. All distributions agree within their statistical uncertainty. Only the simulated events without pile-up are shown, because their number is much higher.

In the case of pile-up the comparison shows similarly good agreement.

7.1.2 Control Sample Selection

To increase the number of events in the control sample the central jet veto is removed only for the control sample selection. Of course this can only be done if the impact of the central jet veto on the shape of the $M_{\tau\tau}$ distribution is negligible. This is verified by comparing the shape of the $M_{\tau\tau}$ distribution of events passing the central jet veto cut to rejected events, cf. Fig. 7.7. The compatibility of both distributions is tested using a Kolmogorov test which results in the values 0.11 without pile-up and 0.34 with pile-up. Both distribution are in good agreement.

These requirements result in the selection of approximately 100 events (94 events with pile-up) assuming a dataset that corresponds to an integrated luminosity of $30\,\mathrm{fb}^{-1}$. This corresponds to about seven times more events in the control sample than the expected $t\bar{t}$ contribution in the signal selection. Considering pile-up this fraction changes to about six times more $t\bar{t}$ events in the control sample than the expected $t\bar{t}$ background.
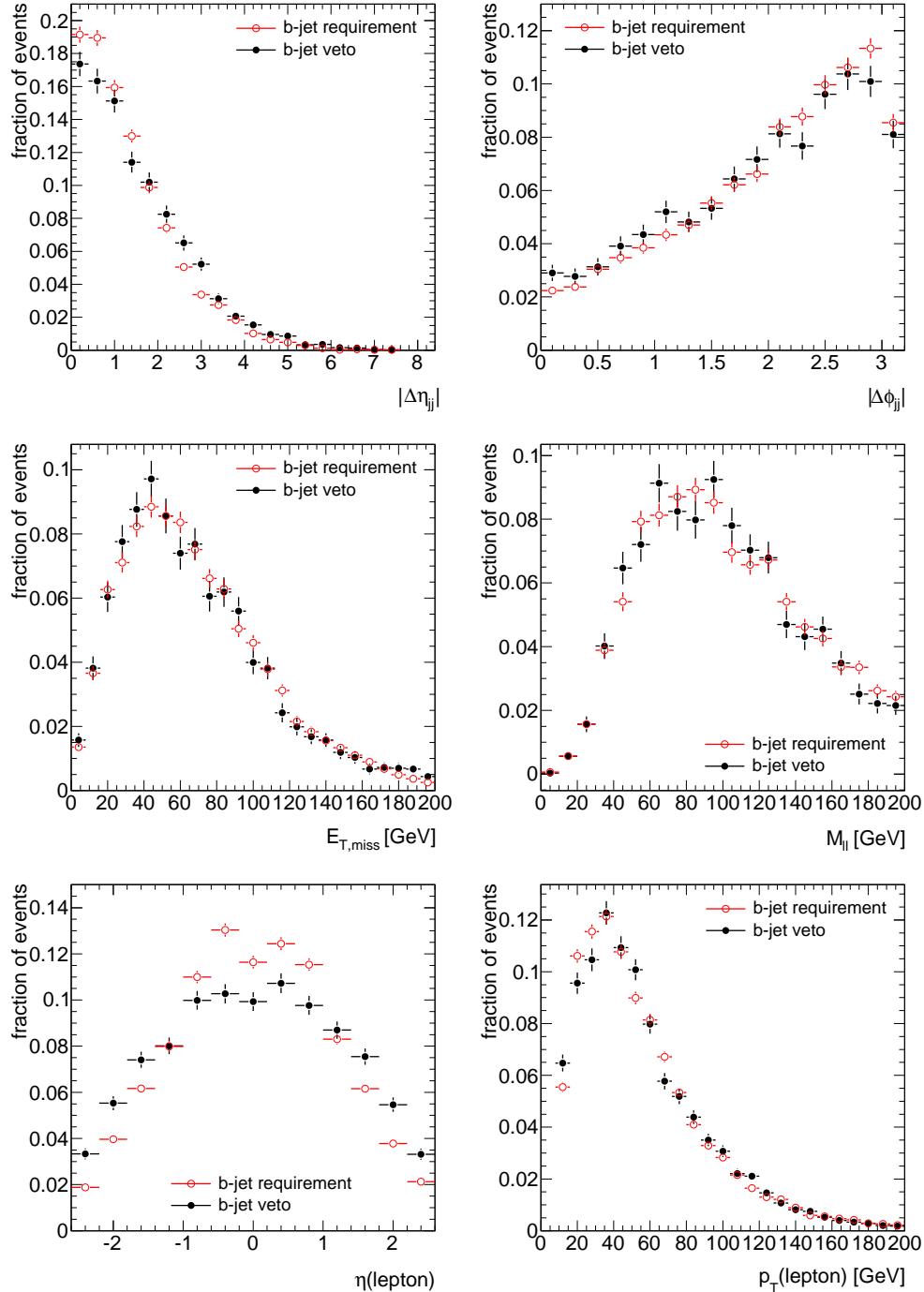
Figure 7.2: *Comparison of $t\bar{t}$ event kinematic without pile-up for events where no b-jet is tagged to events where at least one b-jet is tagged.*

Background in the Control Sample

The expected contribution of the $Z \to \tau\tau$ background in the control sample is 7 ± 2 events not considering pile-up effects assuming a dataset that corresponds to an integrated luminosity of $30\,\mathrm{fb}^{-1}$. This estimation is based on simulated $Z \to \tau\tau$ QCD events generated with *Sherpa*. Contrary to the *Alpgen* events, the *Sherpa* sample includes processes of the form $Zb(b)$. Due to the limited number of Monte Carlo events cut factorisation has to be used. Only the statistical error is given, systematic uncertainties due to cut factorisation and the use of the fast detector simulation are not considered.

Unfortunately no *Sherpa* $Z \to \tau\tau$ events considering pile-up effects are available. The *Alpgen* $Z \to \tau\tau \to \ell\ell + 4\nu$ events predict the same number of events with and without considering pile-up effects. For this reason the expected number of $Z \to \tau\tau$ events is assumed to be 7 in the case of pile-up as well.

The shape of the $M_{\tau\tau}$ distribution without as well as with pile-up is derived using the *Alpgen* events, because the $Z \to \tau\tau$ events generated with *Sherpa* are simulated using the fast detector simulation and no corresponding events considering pile-up are available.

The contribution of other processes to the control sample can be directly read off Table 6.4. The signal is contributing with in average 0.6 events (pile-up: 0.3 events) for a Higgs boson of mass $M_H = 120\,\mathrm{GeV}$.

The contributions from $Z(\to \mu\mu/ee)$ and W+jets are negligible. This has to be handled with care, because the background events generated with *Alpgen* neglect processes of the form $Zb(b)$ and Wb. Unfortunately no $Z(\to \mu\mu/ee)$ and W+jets Monte Carlo samples including the contribution from $Zb(b)$ and Wb processes are available.

The same parametrisation of the $M_{\tau\tau}$ distribution for the $t\bar{t}$ background is used for the control events, because the $M_{\tau\tau}$ distribution of both samples are in good agreement. The shape of the $Z \to \tau\tau \to \ell\ell + 4\nu$ and signal contribution in the $t\bar{t}$ control sample is assumed to be the same as derived in Chapter 6.4. This has been validated with the limited number of Monte Carlo events.

Fig. 7.8 shows the expected $M_{\tau\tau}$ distribution of the control sample selection. The background events lead to a distortion of the $M_{\tau\tau}$ shape which has to be considered when using the control sample for background estimation.

7.1.3   Validation using Data

In addition to the validation using Monte Carlo data, the $t\bar{t}$ background estimation method needs to be validated using data. For this purpose the validation presented in this chapter should in the future be repeated using $t\bar{t}$ events selected in data. This sample needs to be selected without making use of the identification of b-jets. The selection of a pure $t\bar{t}$ sample has been demonstrated using Monte Carlo data. Studies preparing the $t\bar{t}$ production cross section measurement achieve a selection of $t\bar{t}$ events with a purity of about 85% in the lepton-lepton channel [1]. It is expected that this purity could be improved, because this study was not optimised to select $t\bar{t}$ events with a high purity.
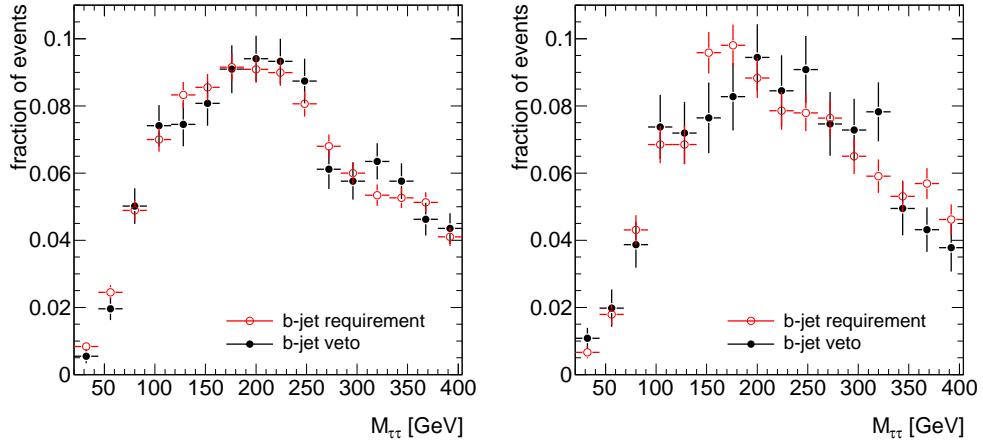
Figure 7.3: *$M_{\tau\tau}$ distribution with b-jet requirement compared to b-jet veto. On the left side without considering pile-up, on the right side with pile-up.*
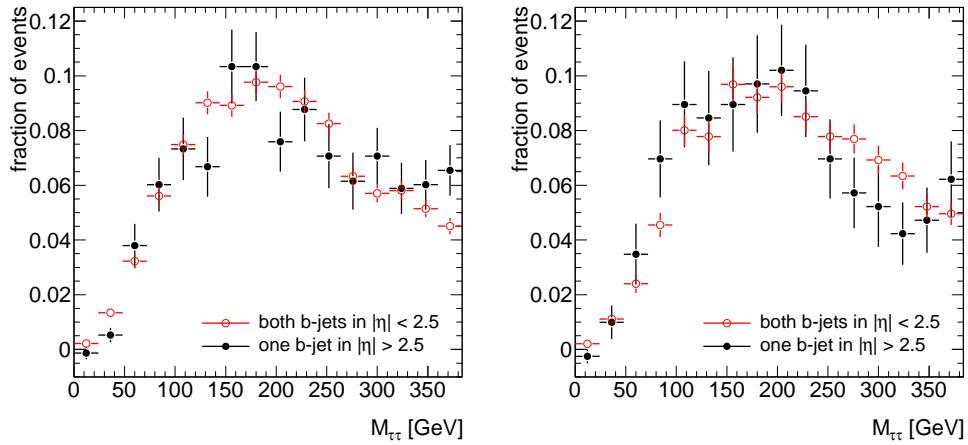

Figure 7.4: *$M_{\tau\tau}$ distribution of $t\bar{t}$ events separated into the categories two and one b-jets lying within $|\eta| < 2.5$. On the left side without considering pile-up, on the right side with pile-up.*
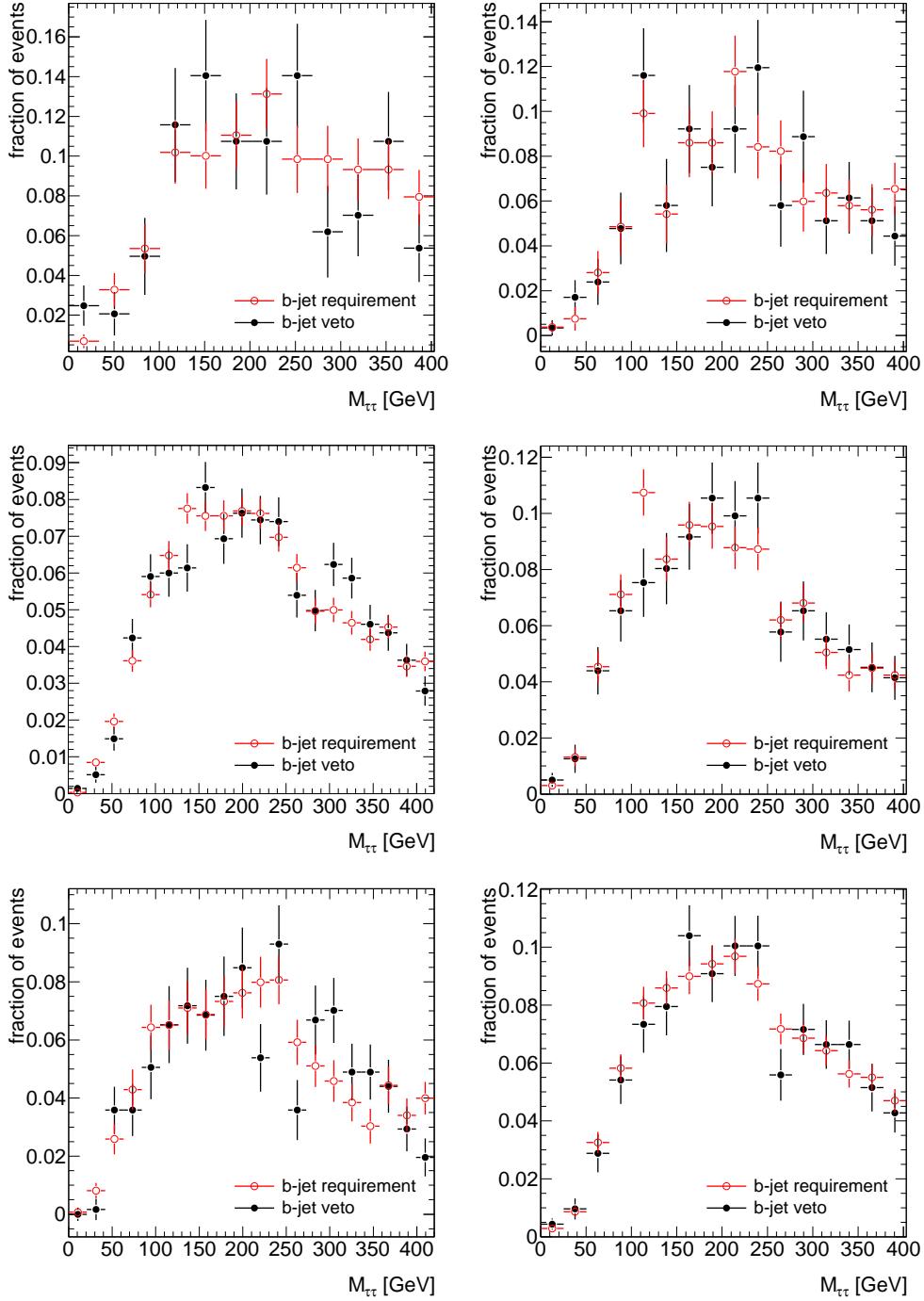
Figure 7.5: *Comparison of $M_{\tau\tau}$ for events passing a certain cut (black filled circles) to rejected events (red open circles). The events are simulated without pile-up. Top left: $M_{jj} > 600 GeV$, top right: $|\Delta\eta_{jj}| > 3.6$, middle left: $|\Delta\phi_{jj}| < 2.5$, middle right: centrality, bottom left: $|\Delta\eta_{j,\ell}| > 0.7$, bottom right: tagging jets being in different pseudo-rapidity hemispheres $\eta_{j1} \times \eta_{j2} < 0$.*
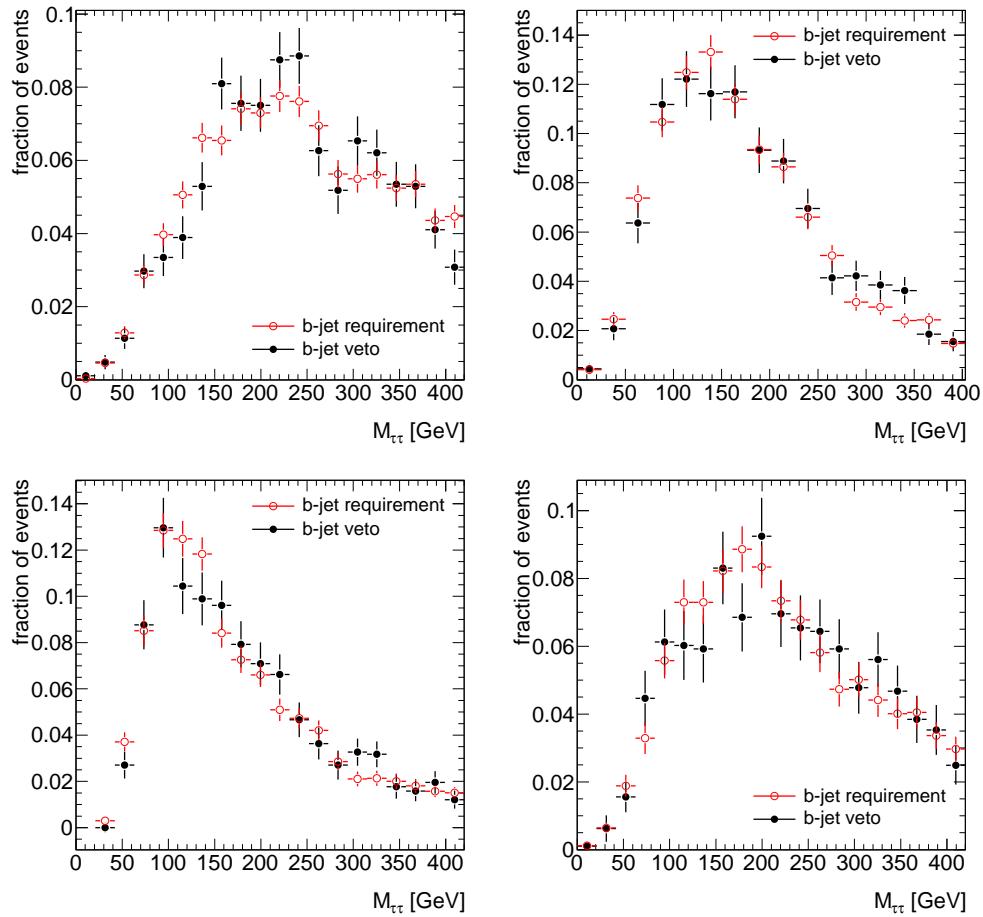
Figure 7.6: *Comparison of $M_{\tau\tau}$ for events passing a certain cut (black filled circles) to rejected events (red open circles). The events are simulated without pile-up. Top left: $E_{\mathrm{T}}^{\mathrm{miss}} > 40\,\mathrm{GeV}$, top right: $|\Delta\phi_{\ell\ell}| < 2.2$, bottom left: $30\,\mathrm{GeV} < M_{ll} < 80\,\mathrm{GeV}$, bottom right: central jet veto.*
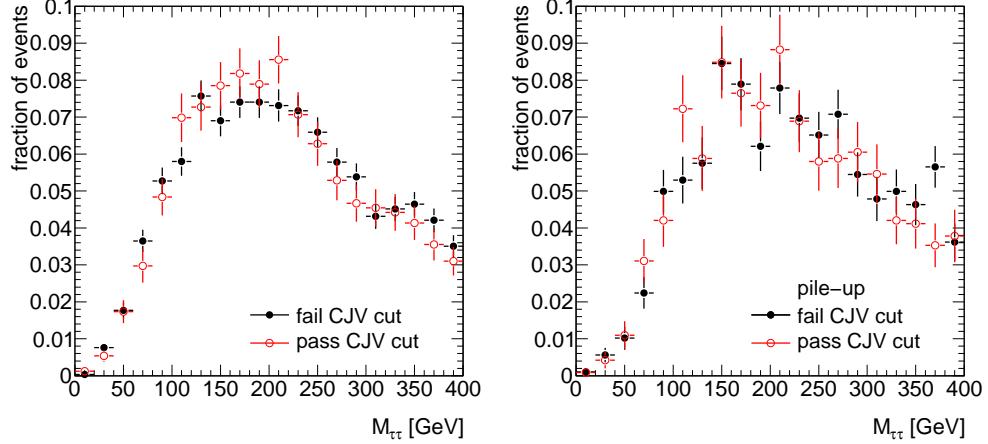
Figure 7.7: *Comparison of the $M_{\tau\tau}$ distribution for events passing the central jet veto cut (black filled circles) to rejected events (red open circles). In both selections only events with at least one identified b-jet are used. On the left without considering pile-up, on the right including pile-up.*
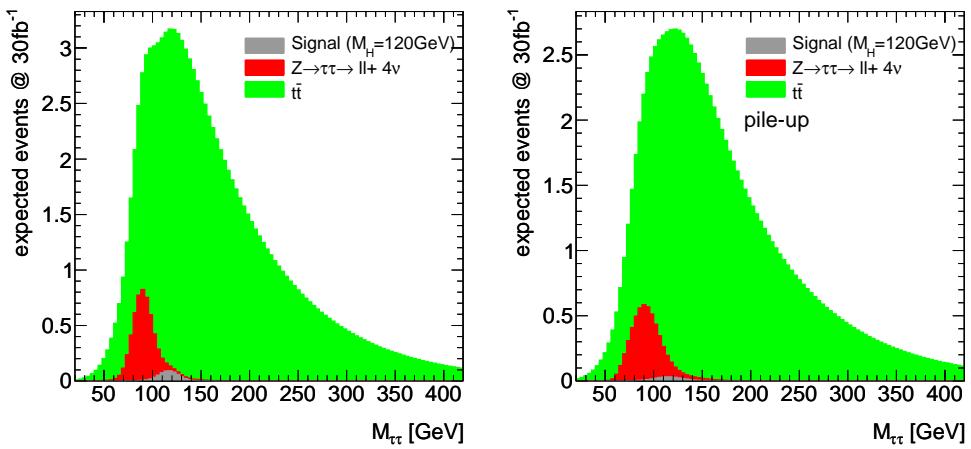
Figure 7.8: *$M_{\tau\tau}$ distribution of the $t\bar{t}$ control sample without (left) and with (right) pile-up. The $Z \to \tau\tau$ and signal process lead to a distortion of the shape. The histograms are stacked and are normalised to the expected number of events assuming a dataset that corresponds to an integrated luminosity of $30\,\mathrm{fb}^{-1}$.*

7.2 Estimation of $Z \to \tau\tau$ Background

To select a control sample for the $Z \to \tau\tau \to \ell\ell + 4\nu$ background the process Z+jets with the decay $Z \to \mu\mu$ is utilised. Neglecting the differences in mass between the muon and the τ-lepton, the kinematics of the muons and the τ-leptons in both processes are identical. Furthermore the kinematics of additional jets are the same. $Z \to \mu\mu$ events provide a signal-free signature of two isolated, high energetic muons with opposite charge and a di-muon invariant mass at the Z resonance.

The $Z \to \tau\tau \to \ell\ell + 4\nu$ process can be modelled modifying the muons in the $Z \to \mu\mu$ events to make them look like τ-lepton decays. This event modification is done using an embedding technique [61, 62] which replaces the muons from the Z decay by the decay products of equivalent τ-leptons. The kinematics of the τ-leptons are given by the kinematics of the muons. Their decays are generated using Monte Carlo simulation, which is justified by the well-understood Z boson and τ-lepton decays. In this way a $Z \to \tau\tau \to \ell\ell + 4\nu$ event is produced, in which only the $Z \to \tau\tau \to \ell\ell + 4\nu$ decay is produced by Monte Carlo, whereas the event remnant and the event kinematics are given by data.

In the following the creation of the control sample using the embedding method is introduced. First the method is explained in detailed and validated using Monte Carlo simulated events. Afterwards the selection of the $Z \to \mu\mu$ and its impact of the selection criteria on the control sample are discussed.

7.2.1 Conversion of $Z \to \mu\mu$ events into $Z \to \tau\tau$ events

The general procedure of converting $Z \to \mu\mu$ into $Z \to \tau\tau \to \ell\ell + 4\nu$ events is illustrated in Fig. 7.9 and can be divided into four basic steps:

1. Z decay identification: the two muons of the Z decay are selected.

2. Construction of $Z \to \tau\tau \to \ell\ell + 4\nu$ decay: the $Z \to \mu\mu$ decay is turned into a $Z \to \tau\tau \to \ell\ell + 4\nu$ decay with the same kinematics. The production vertex of the τ-leptons is set to the production vertex of the muons. The decay of the τ-leptons is performed by TAUOLA. Afterwards the full ATLAS simulation, digitisation and reconstruction are applied.

3. Embedding: the muons from the $Z \to \mu\mu$ decay in the original event are replaced by the decay products of the τ-leptons from the $Z \to \tau\tau \to \ell\ell + 4\nu$ decay using calorimeter cell and track information.

4. Re-reconstruction: the ATLAS event reconstruction is re-run to obtain the $Z \to \tau\tau \to \ell\ell + 4\nu$ event.

In the following the different parts of the method are discussed.

Identification of $Z \to \mu\mu$ Decays

In this first step the two muons from the $Z \to \mu\mu$ decay are selected. The actual selection criteria are adjustable and not relevant for the procedure itself. In this analysis exactly two
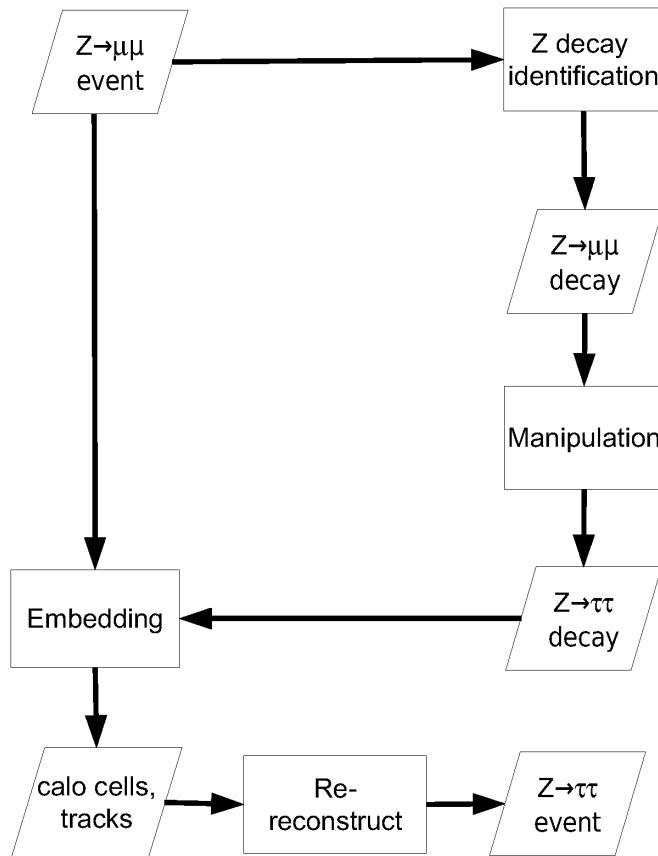
**Figure 7.9:** *Flowchart of the embedding procedure.*

isolated combined muons with $p_T > 10\,\mathrm{GeV}$ are required. Both muons have to be assigned to the same primary vertex. After having selected two muons their four-vectors are added to get the four-vector of the Z boson.

Events not fulfilling the requirements are marked and discarded.

Construction of $Z \to \tau\tau$ Decay

The $Z \to \mu\mu$ decay is transformed into a $Z \to \tau\tau \to \ell\ell + 4\nu$ decay having the same kinematics. For this purpose the muons are declared as τ-leptons and their four vectors together with the four vector of the Z boson are written to an ASCII file in the HEPEVT [63] format. The production vertex of the τ-leptons and the decay vertex of the Z boson are set to the production vertex of the muons. To account for the τ-lepton mass the four-vector of the muon momenta are rescaled so that $p_\tau = \sqrt{E_\mu^2 - m_\tau^2}$. The ASCII file is read into *ATHENA* and processed by TAUOLA and PHOTOS. TAUOLA generates the τ-leptons decay, with PHOTOS adding final state radiation. These events are then fed into the ATLAS detector simulation, digitisation and reconstruction.

The application of PHOTOS adds final state radiation a second time, because the muons which are declared as τ-leptons have already undergone final state radiation. On the other

hand final state radiation needs to be added to the τ-lepton decay products. For this reason PHOTOS is used and the application of final state radiation to the τ-leptons a second time is accepted.

It is important to note that the decay vertex of the $Z \to \tau\tau \to \ell\ell + 4\nu$ decay matches the decay vertex of the $Z \to \mu\mu$ decay. This is achieved by requiring that both muons are assigned to the same primary vertex (see Paragraph: Identification of Z Decays). Further the displacement of the beam spot and the smearing of the interaction vertex in the simulation of the $Z \to \tau\tau \to \ell\ell + 4\nu$ decay is switched off.

The simulation of electronic noise in the calorimeter is switched off in the simulation of the $Z \to \tau\tau \to \ell\ell + 4\nu$ decay, to avoid double counting of energy in the embedding step.

Embedding

The embedding step itself replaces the $Z \to \mu\mu$ decay of the original event with the simulated $Z \to \tau\tau \to \ell\ell + 4\nu$ decay. The replacement is done using calorimeter cells, inner detector tracks and muon spectrometer track segments. The algorithm is subdivided into the following steps:

1. The calorimeter cells in a cone of size $\Delta R_{inner} \leq 0.1$ around the muons of the $Z \to \mu\mu$ decay are replaced by the corresponding calorimeter cells of the $Z \to \tau\tau \to \ell\ell + 4\nu$ decay. This means their energy and timing[2] information are replaced. The calorimeter cells in a hollow cone of size $0.1 < \Delta R_{outer} \leq 0.3$ around the muons are added to their corresponding calorimeter cells of the $Z \to \mu\mu$ decay. This means that their energies are added and the timing information is replaced.

2. All track segments in the muon spectrometer inside a cone of size $\Delta R \leq 0.3$ around the original muons are deleted. The track segments in the muon spectrometer of the $Z \to \tau\tau \to \ell\ell + 4\nu$ decay, within the same cone are inserted into the original event.

3. The tracks belonging to the muons of the $Z \to \mu\mu$ decay are replaced by all tracks of the $Z \to \tau\tau \to \ell\ell + 4\nu$ decay.

The size of the cones must be chosen in a way that all muon spectrometer track segments and all calorimeter cells containing energy depositions of the object to remove or to embed are selected. On the other hand too big cones remove too much of the event remnant.

In exactly that manner the size of the inner cone is chosen to remove all energy depositions of the muons from $Z \to \mu\mu$ decay, while the size of the outer cone is optimized to select all energy depositions of the objects to embed. The choice of the outer cone size also involves the collinear approximation, since the muon to remove and the lepton to embed have only approximately the same direction.

The energies of calorimeter cells in the region between the inner and the outer cone are added, to keep the energy depositions arising from other objects. The simulation of electronic noise in the calorimeter is switched off in the simulation of the $Z \to \tau\tau \to \ell\ell + 4\nu$ decay to avoid double counting of energy. Furthermore pile-up effects are ignored in the

---

[2]To each calorimeter cell the time when the energy was deposit, relative to the bunch crossing, is assigned [64].

$Z \rightarrow \tau\tau \rightarrow \ell\ell + 4\nu$ decay. For this reason the embedding method leads to the absence of noise and pile-up in the region of the inner cone in the calorimeter.

The values of the cone sizes chosen in this study are optimised to result in a reasonable agreement between the $Z \rightarrow \tau\tau \rightarrow \ell\ell + 4\nu$ Monte Carlo sample and the embedded sample in terms of transverse momentum, isolation and number of reconstructed objects.

Re-reconstruction

After the embedding step the event is passed to the ATLAS event reconstruction. Since the embedding acts on calorimeter cell and track level, only parts of the reconstruction need to be re-run. In particular these are the calorimeter cluster, jet, electron, photon, τ-lepton, muon and missing transverse energy reconstruction. Care has to be taken in choosing the correct configuration of the reconstruction algorithms in terms of calibration constants, detector description, etc. Otherwise a systematic bias of the $Z \rightarrow \mu\mu$ events after embedding is observed.

7.2.2 Validation using Monte Carlo Simulation

When comparing the simulated $Z \rightarrow \mu\mu$ events with the simulated $Z \rightarrow \tau\tau \rightarrow \ell\ell + 4\nu$ events, the applied lepton filter after the event generation needs to be considered, see Section 4.2. In the case of the $Z \rightarrow \mu\mu$ events the requirements of the lepton filter are directly applied to the Z decay products whereas int the case of the $Z \rightarrow \tau\tau \rightarrow \ell\ell + 4\nu$ events the requirements are applied to muons and electrons from τ-lepton decays. For this reason the requirements of the lepton filter needs to be applied to the $Z \rightarrow \mu\mu$ events after embedding.
Except for the Z boson decay products $Z \rightarrow \mu\mu$ events and $Z \rightarrow \tau\tau \rightarrow \ell\ell + 4\nu$ events are kinematically identical. Therefore differences between the $Z \rightarrow \mu\mu$ events after embedding and the $Z \rightarrow \tau\tau \rightarrow \ell\ell + 4\nu$ events should only be visible in the vicinity of the embedded objects.

Muons: A priori the muons are expected to be the simplest particle to embed. Muons deposite only a small fraction of their energy in the calorimeter and are reconstructed purely from inner detector and spectrometer tracks. As shown in Fig. 7.10 the spectrum of transverse momentum is reproduced very well using the embedding procedure. This is expected since the tracking does not change by the embedding.
The replacing and adding of calorimeter cells affects the energy content in the vicinity of the muons. When the energy depositions of the muons of the $Z \rightarrow \mu\mu$ events are removed, noise is removed, too. The added energy of the calorimeter cells of the $Z \rightarrow \tau\tau \rightarrow \ell\ell + 4\nu$ decay does not contain calorimeter noise, because the noise simulation in the calorimeter is switched off in the embedding procedure. For this reason the noise in the calorimeter is neglected in the inner cone.
Furthermore calorimeter based objects in close vicinity to the replaced muons can be affected due to the removing procedure of calorimeter cells. Related to this is the calorimeter isolation of the muons, which is in general well reproduced, cf. Fig. 7.10.
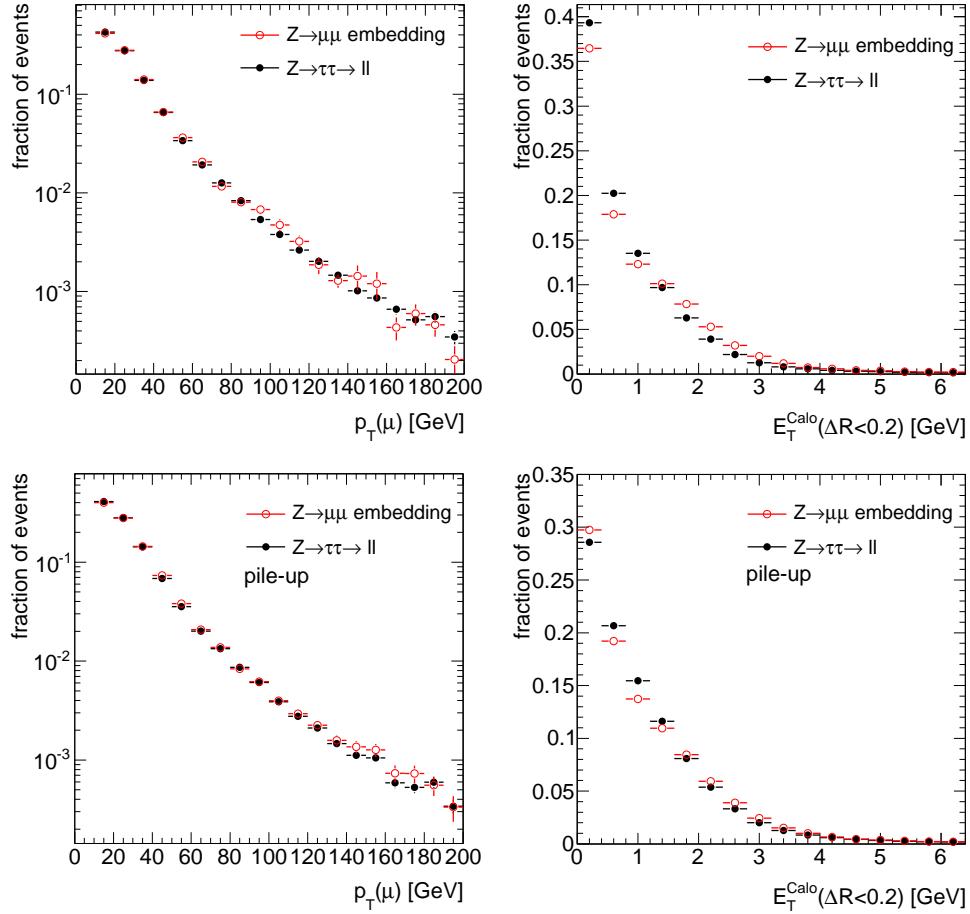
Figure 7.10: *Comparison of muons of $Z \to \tau\tau \to \ell\ell + 4\nu$ and $Z \to \mu\mu$ after embedding for samples without (top) and with (bottom) pile-up. The standard muon selection as discussed in Section 6.2.2 is required. On the left the transverse momentum distributions are shown. On the right the distributions of the transverse energy measured in the calorimeter in a cone of $\Delta R < 0.2$ around the muon axis are shown. The expected energy loss of the muon is subtracted.*

Since muons from $Z \to \mu\mu$ are typically well isolated, the impact of the calorimeter embedding on the performance is small.

Electrons: From the perspective of the embedding procedure, electrons are more complex objects than muons because they involve tracking and calorimetry. The energy of an electron is measured in the calorimeter, whereas its position is determined by the associated track. The electron identification variables related to tracking are well reproduced, because the embedding uses reconstructed tracks. The transverse momentum spectrum of the electrons is in reasonable agreement, cf. Fig. 7.11. This indicates that the cone sizes for replacing and adding calorimeter cells are large enough and contain all energy depositions of the electron in the calorimeter. As expected the calorimeter isolation of the electrons shows some deviations compared to the $Z \to \tau\tau \to \ell\ell + 4\nu$ events.
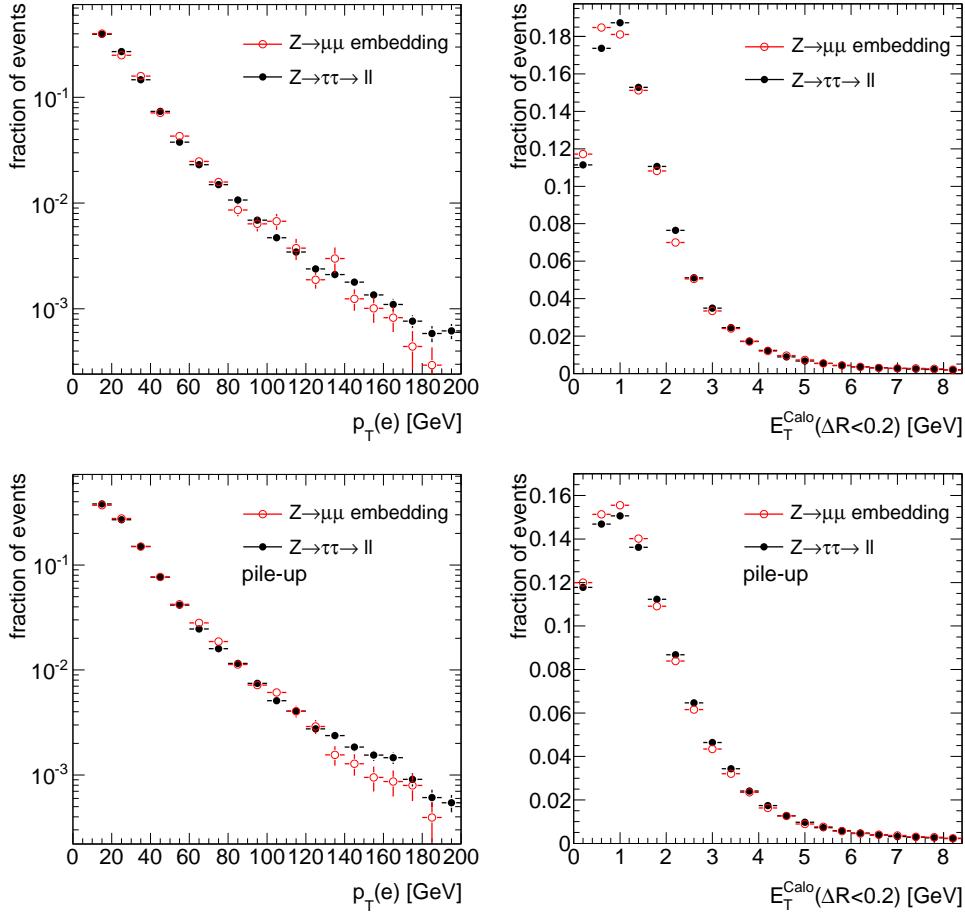
Figure 7.11: *Comparison of electrons of $Z \to \tau\tau \to \ell\ell + 4\nu$ and $Z \to \mu\mu$ after embedding for samples without (top) and with (bottom) pile-up. The standard electron selection as discussed in Section 6.2.2 is required. On the left the transverse momentum distributions are shown. On the right the distributions of the transverse energy measured in the calorimeter in a cone of $\Delta R < 0.2$ around the electron axis are shown. The reconstructed energy of the electron is subtracted.*

The main goal is to reproduce the $M_{\tau\tau}$ distribution to high precision. In addition to $M_{\tau\tau}$ the relevant quantities to judge the performance of the embedding method are the four-momenta of the τ-lepton decay products and the missing transverse energy, because they are needed to calculate $M_{\tau\tau}$.

As discussed above the kinematic distributions of the electrons and muons are in reasonable agreement. This is confirmed by the comparison of the di-lepton invariant mass, which is reproduced in good agreement using the embedding method, cf. Fig. 7.12 and Fig. 7.13.

The most difficult quantity to handle is the missing transverse energy, since it involves all reconstructed objects. Furthermore it is highly sensitive to adjustable parameters in the event reconstruction like jet calibration constants, vertex displacement, etc. Therefore the comparison of $E_{\mathrm{T}}^{\mathrm{miss}}$ is an important test to validate the performance of the embedding method. As shown in Figures 7.12 and 7.13 it is in good agreement.
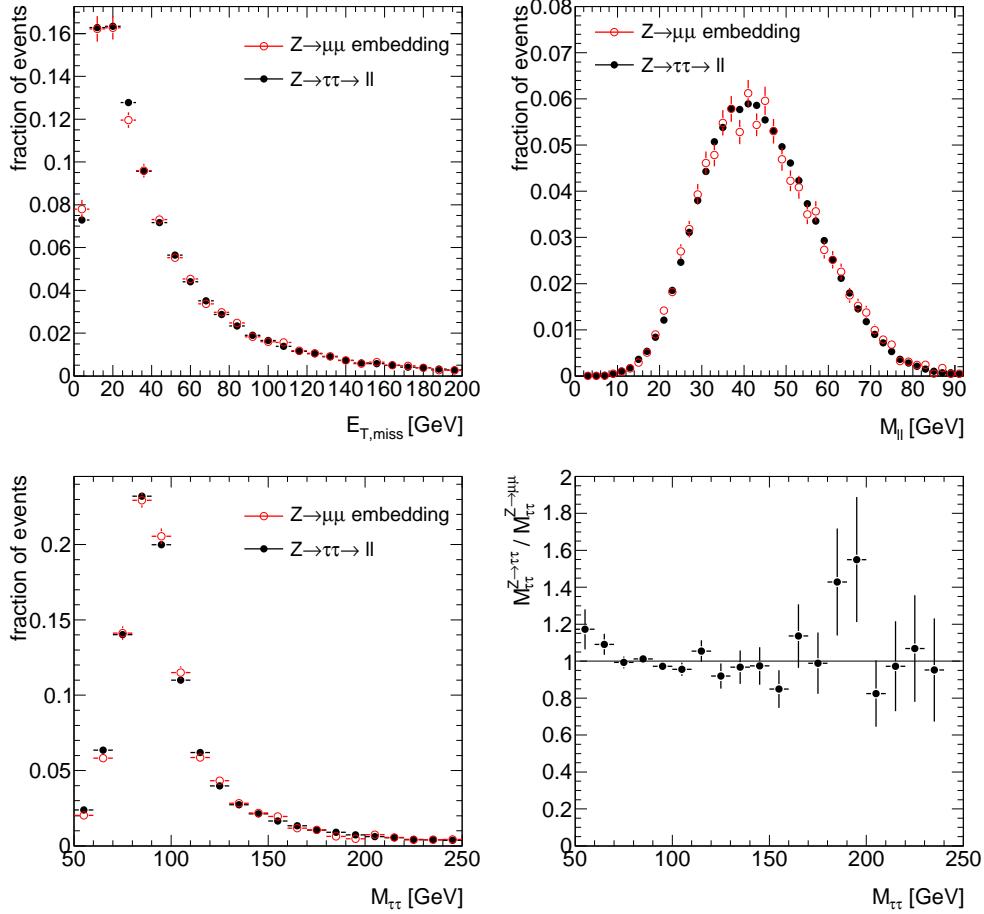
**Figure 7.12:** *Comparison of $Z \to \tau\tau \to \ell\ell + 4\nu$ and $Z \to \mu\mu$ after embedding without pile-up. The standard lepton selection as discussed in Section 6.2.2 is required. Top left: Missing transverse energy, top right: di-lepton invariant mass, bottom left: $M_{\tau\tau}$ distribution calculated using the collinear approximation, bottom right: ratio of the $M_{\tau\tau}$ distributions. Events entering the $M_{\tau\tau}$ distribution are required to fulfil $0 < x_{1,2} \leq 1$, see Section 6.2.3. All distributions are in reasonable agreement.*

Finally the comparison of the $M_{\tau\tau}$ distribution shows that the embedding works very well. For a better comparison the ratio of the $M_{\tau\tau}$ distributions of $Z \to \tau\tau \to \ell\ell + 4\nu$ and $Z \to \mu\mu$ after embedding is shown as well.

7.2.3 $Z \to \mu\mu$ Event Selection

The selection of $Z \to \mu\mu$ events as input to the embedding procedure uitilises the two muons from the Z decay. Since there are no neutrinos in the final state the missing transverse energy should be small. Furthermore the VBF analysis cuts are applied, because they suppress the background from QCD processes and will be applied anyway after the embedding.
In the following the selection cuts are discussed in detail.
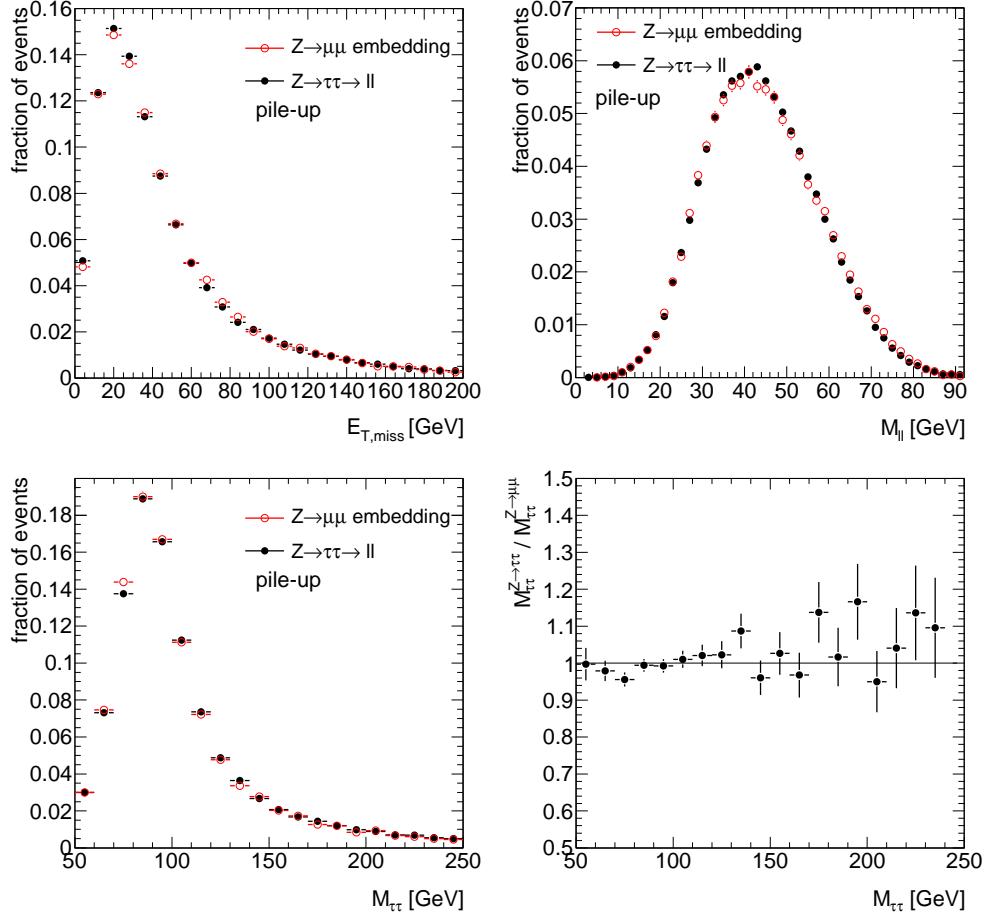
Figure 7.13: *Comparison of $Z \to \tau\tau \to \ell\ell + 4\nu$ and $Z \to \mu\mu$ after embedding with pile-up. The standard lepton selection as discussed in Section 6.2.2 is required. Top left: Missing transverse energy, top right: di-lepton invariant mass, bottom left: $M_{\tau\tau}$ distribution calculated using the collinear approximation, bottom right: ratio of the $M_{\tau\tau}$ distributions. Events entering the $M_{\tau\tau}$ distribution are required to fulfil $0 < x_{1,2} \leq 1$, see Section 6.2.3. All distributions are in reasonable agreement.*

Trigger and Lepton Selection   The two muons provide a good signature for the event trigger. A single muon trigger requiring $p_T \geq 20\,\text{GeV}$ and a di-muon trigger requiring both muons to have $p_T \geq 10\,\text{GeV}$ are used. The muon selection considers only combined muons with inner detector and muon spectrometer tracks with at least a $p_T \geq 10\,\text{GeV}$. The muons need to be well isolated which is achieved by requiring the summed E_T in the calorimeter in a cone of $\Delta R = 0.2$ around the muons being less than 10% of the muon p_T. In the case of pile-up the muon isolation is changed to 15% of the muon p_T.

The requirement on the transverse momentum is adapted depending on the satisfied trigger condition:

- single muon: one muon with $p_T \geq 20\,\text{GeV}$.

- double muon: two muons with $p_T \geq 15\,\text{GeV}$.

The two muons are required to have opposite charge.

Event Kinematics   To make use of the fact that the two muons are the products of the Z boson decay a cut on the di-muon invariant mass is applied: $M_{\mu^+\mu^-} > 60\,\mathrm{GeV}$. The mass $M_{\mu^+\mu^-}$ of a $Z \to \mu\mu$ event corresponds to the mass $M_{\tau\tau}$ of the event after embedding. A requirement on $M_{\mu^+\mu^-}$ directly translates into a requirement on $M_{\tau\tau}$. To avoid any impact on the shape of the $M_{\tau\tau}$ distribution in the signal region, no further requirement on $M_{\mu^+\mu^-}$ is applied.

No neutrinos are present in the final state, for this reason the missing transverse energy is required to be $E_\mathrm{T}^\mathrm{miss} < 40\,\mathrm{GeV}$ without pile-up. In the case of pile-up the cut is increased to $E_\mathrm{T}^\mathrm{miss} < 45\,\mathrm{GeV}$.

After the embedding procedure the VBF analysis cuts are applied to the $Z \to \mu\mu$ events. Thus analysis cuts, not depending on the lepton properties, can already be employed in the $Z \to \mu\mu$ event selection. These cuts are related to the kinematics of the tagging jets. In particular the events are required to have at least two jets. The leading and second leading jets are selected as tagging jets and should have transverse momentum $p_T > 40\,\mathrm{GeV}$ and $p_T > 20\,\mathrm{GeV}$ respectively. Both jets should lie within $|\eta| < 4.8$ and be well separated in pseudo-rapidity $\Delta\eta_{jj} > 3.6$ ($\Delta\eta_{jj} > 3.2$ in the case of pile-up). Their invariant di-jet mass M_{jj} is required to be higher than $M_{jj} > 600 GeV$. The separation in ϕ is required to be $|\Delta\phi_{jj}| < 2.5$. The $t\bar{t}$ background contribution is suppressed applying the b-jet veto, which rejects events containing a jet having a b-tagging weight $b_{weight} > 4$.

Selection Results   Table 7.1 shows the results of the $Z \to \mu\mu$ selection. About 23000 $Z \to \mu\mu$ events are expected assuming a dataset that corresponds to an integrated luminosity of $30\,\mathrm{fb}^{-1}$. Considering pile-up the number of expected $Z \to \mu\mu$ events increases to about 30000. This is mainly caused by the slightly different cut selection and the higher number of jets.

The largest background contribution is caused by the $t\bar{t}$ process with about 1.2% (1.4% in the case of pile-up) with respect to the $Z \to \mu\mu$ events. The contribution of the $t\bar{t}$ background is estimated using the cut factorisation method. In this case the selection cuts are arranged into three groups:

1. Object selection cuts: trigger, muon selection, muon p_T.

2. Z boson related selection cuts: $M_{\mu^+\mu^-}$, $E_\mathrm{T}^\mathrm{miss}$.

3. Jet related selection cuts: tagging jet selection, $\Delta\eta_{jj}$, M_{jj}, b-jet veto, $\Delta\phi_{jj}$.

The efficiencies of the second and third group are determined with respect to the selection cuts in the first group. The efficiency of the total cut selection is estimated by the product of the efficiencies of each group.

The contribution of the other background processes is of minor importance and is estimated to about 0.3% (0.3% in the case of pile-up as well) with respect to the $Z \to \mu\mu$ events. Due to the very limited number of Monte Carlo events the estimation of the W+jets background is highly uncertain. In summary the $Z \to \mu\mu$ sample can be selected as input

Cuts	$Z \to \mu\mu$	$Z \to \tau\tau$	$t\bar{t}$	W+jets	$H \to \tau\tau \to \ell\ell + 4\nu$
None	42620	3720	467300	1154600	20.39
Trigger	38330	842	125120	353000	7.6
N(muon) $= 2$	29060	236	7303	57	2.0
Muon charge	29050	236	7090	27	2.0
Trigger Muon	29050	235	7088	27	2.0
$M_{\mu\mu} \geq 60\,\text{GeV}$	28872	32	5114	12	0.7
$E_{\text{T}}^{\text{miss}} \leq 40\,\text{GeV}$	28438	27	1219	6.6	0.4
Tagging jet selection	9399	8.4	483*	4.7	0.2
$|\Delta\eta_{jj}| > 3.6$	3917	3.5	75*	2.4	0.18
$M_{jj} > 600\,\text{GeV}$	1312	1.1	45*	< 2.1	0.12
b-jet veto	1271	1.1	14*	< 2.1	0.12
$|\Delta\phi_{jj}| < 2.5$	765 ± 8	0.56 ± 0.04	$8.9 \pm 0.8^*$	< 2.1	0.077 ± 0.006

Table 7.1: *Accepted cross section after each selection step. The cross sections are given in fb. The selection cuts are applied to processes without pile-up. The cross sections are given in fb. Only statistical uncertainties are quoted. The given cross sections already include the efficiencies of the applied event filter. The limit corresponds to an 95% confidence level according to the Poisson distribution. An asterisk is used to indicate cross sections estimated using the cut factorisation method. The $Z \to \tau\tau$ process includes QCD and EW contributions.*

for the embedding procedure with less than 2% background contamination.

The background contribution in the $Z \to \mu\mu$ sample after embedding and applied analysis cuts is the important quantity. Unfortunately this cannot be studied, since the current set of Monte Carlo event samples do not exist in the needed data format ESD [3]. Nevertheless it is not expected that the analysis cuts increase the contribution of the background processes. Especially the selection cuts $\Delta\eta_{j\ell}$, centrality and central jet veto are expected to reduce the relative contribution of $t\bar{t}$ background.

Comparison of the $M_{\tau\tau}$ shape   To verify that the proposed $Z \to \mu\mu$ selection cuts do not systematically bias the control sample the $Z \to \mu\mu$ events after embedding using the above described selection cuts are compared to the $Z \to \tau\tau \to \ell\ell + 4\nu$ events. Due to the very limited number of Monte Carlo events only the trigger, muon selection, $M_{\mu\mu}$ and $E_{\text{T}}^{\text{miss}}$ cuts are applied. The cuts related to the tagging jet kinematics are omitted since the jet kinematics of $Z \to \mu\mu$ and $Z \to \tau\tau \to \ell\ell + 4\nu$ events is the same.

Figures 7.14 and 7.15 show the comparison of $Z \to \tau\tau \to \ell\ell + 4\nu$ and $Z \to \mu\mu$ after embedding. Without pile-up the distributions are in good agreement and no systematic bias due to the used $Z \to \mu\mu$ selection is observed. In the presence of pile-up the $E_{\text{T}}^{\text{miss}}$ distribution of the $Z \to \mu\mu$ after embedding shows a small shift to lower values. This shift is introduced by the isolation requirement of the muon selection. However, the distributions of the di-lepton invariant mass $M_{\ell\ell}$ and most importantly the $M_{\tau\tau}$ distributions are in good agreement. In the signal region ($100\,\text{GeV} < M_{\tau\tau} < 150\,\text{GeV}$) the shape of the $M_{\tau\tau}$

---

[3]The Event Summary Data (ESD) is a data format for persistent storage of the ATLAS data, containing detailed reconstruction information [65], because of which it consumes a lot of disc space. The ATLAS Monte Carlo production policy allows only a maximum of 10% of the Monte Carlo data to be stored in the ESD format. An exception has been made on special request for the $Z \to \mu\mu$ datasets only.

Cuts	$Z \to \mu\mu$	$Z \to \tau\tau$	QCD	$t\bar{t}$	W+jets	$H \to \tau\tau \to \ell\ell + 4\nu$
None	1906	467300		1154600		20.39
Trigger	35230	608		112900	273500	6.70
N(muon) = 2	27760	214		7430	71	1.89
Muon charge	27760	214		7110	37	1.89
Trigger Muon	27760	213		7100	37	1.89
$M_{\mu\mu} \geq 60\,\mathrm{GeV}$	27600	29		5030	20	0.645
$E_{\mathrm{T}}^{\mathrm{miss}} \leq 45\,\mathrm{GeV}$	26220	24		1416	9	0.439
Tagging jet selection	9370	8.5		577*	4	0.235
$|\Delta\eta_{jj}| > 3.2$	5072	4.6		137*	3.1	0.198
$M_{jj} > 600\,\mathrm{GeV}$	1693	1.4		67*	< 2.1	0.128
b-jet veto	1638	1.3		23*	< 2.1	0.126
$|\Delta\phi_{jj}| < 2.5$	999 ± 7	0.80 ± 0.47		$14 \pm 1^*$	< 2.1	0.083 ± 0.006

Table 7.2: *Accepted cross section after each selection step. The cross sections are given in fb. The selection cuts are applied to processes with pile-up. Only the statistical uncertainties are quoted. The given cross sections include already the efficiencies of the applied event filter. The limit corresponds to a 95% confidence level according to the Poisson distribution. An asterisk is used to indicate cross sections estimated using the cut factorisation method.*

distribution of the $Z \to \tau\tau \to \ell\ell + 4\nu$ background is very well reproduced and agrees within 10%. This proves that the $Z \to \mu\mu$ selection can be used and the embedding procedure can successfully mimic the $Z \to \tau\tau \to \ell\ell + 4\nu$ process.

After the application of all selection cuts the $M_{\tau\tau}$ distributions show good agreement within the statistical uncertainty, cf. Fig. 7.16. Using the discussed selection cuts about 220 events (270 with pile-up) are expected in the control sample assuming a dataset that corresponds to an integrated luminosity of $30\,\mathrm{fb}^{-1}$. This corresponds to about four times more events than the expected $Z \to \tau\tau \to \ell\ell + 4\nu$ background events in the signal selection. Considering pile-up this fraction increases to about five times more events in the control sample. The increase of events is caused by the slightly different event selection.

Since the shapes of the $M_{\tau\tau}$ distribution for the $Z \to \tau\tau \to \ell\ell + 4\nu$ background and the control sample are in good agreement the same parametrisation is used for both.

7.2.4 Validation using Data

In addition to the performance and validation presented in this chapter, various tests using Monte Carlo data have been performed to ensure the validity of the method. Among them are the application of the embedding procedure to obtain a $Z \to \mu\mu$ decay, which means that the conversion of muons to τ-leptons and their subsequent decay are omitted. Further the embedding procedure has been tested using generated quantities as input. In addition several tests for the non trivial re-running of the event reconstruction have been carried out. All in all the embedding procedure has demonstrated a very good performance.

In Addition validation procedures using collison data have to be carried out. As an example the embedding of muons and electrons instead of τ-leptons and the corresponding comparison to $Z \to \mu\mu$ and $Z \to ee$ can be used to tune and confirm the performance achieved

using simulated events. In the scope of a MSSM Higgs boson $H \to \tau\tau$ analysis, using the data recorded with ATLAS in the year 2010, the embedding procedure is used to estimate the $Z \to \tau\tau \to \ell\ell + 4\nu$ background. In this context first tests between $Z \to \mu\mu$ data after embedding and $Z \to \tau\tau \to \ell\ell + 4\nu$ Monte Carlo data demonstrate a good performance of the embedding procedure [66].
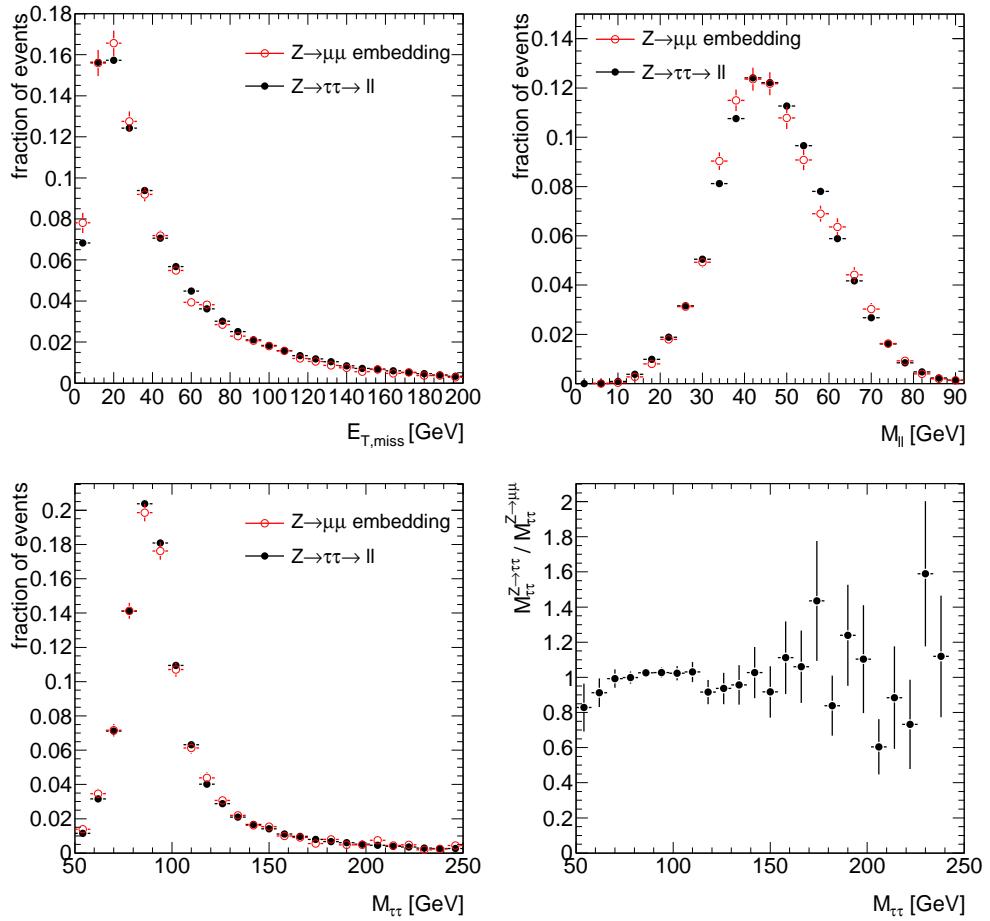

Figure 7.14: *Comparison of $Z \to \tau\tau \to \ell\ell + 4\nu$ and $Z \to \mu\mu$ after embedding without pile-up. The standard lepton selection as discussed in Section 6.2.2 is required. The $Z \to \mu\mu$ events, which serve as input to the embedding procedure, have been selected using the trigger, muon selection, $M_{\mu\mu}$ and E_T^{miss} cuts. Top left: Missing transverse energy, top right: di-lepton invariant mass, bottom left: $M_{\tau\tau}$ distribution calculated using the collinear approximation, bottom right: ratio of the $M_{\tau\tau}$ distributions. Events entering the $M_{\tau\tau}$ distribution are required to fulfil $0 \leq x_{1,2} \leq 1$, see Section 6.2.3. All distributions are in reasonable agreement.*

Figure 7.15: *Comparison of $Z \to \tau\tau \to \ell\ell + 4\nu$ and $Z \to \mu\mu$ after embedding with pile-up. The standard lepton selection as discussed in Section 6.2.2 is required. The $Z \to \mu\mu$ events, which serve as input to the embedding procedure, have been selected using the trigger, muon selection, $M_{\mu\mu}$ and E_T^{miss} cuts. Top left: Missing transverse energy, top right: di-lepton invariant mass, bottom left: $M_{\tau\tau}$ distribution calculated using the collinear approximation, bottom right: ratio of the $M_{\tau\tau}$ distributions. Events entering the $M_{\tau\tau}$ distribution are required to fulfil $0 \leq x_{1,2} \leq 1$, see Section 6.2.3. All distributions are in reasonable agreement.*

Figure 7.16: *Comparison of $M_{\tau\tau}$ distribution of $Z \to \tau\tau \to \ell\ell + 4\nu$ and $Z \to \mu\mu$ after embedding after all selection cuts have been applied.*

7.3   Summary

In this chapter methods to estimate the main background processes $Z \rightarrow \tau\tau \rightarrow \ell\ell + 4\nu$ and $t\bar{t}$ production from data have been presented. These methods rely on the selection of control samples which give a precise description of the shape of the $M_{\tau\tau}$ distribution.

- $t\bar{t}$ background: The selection of the control sample to estimate the $t\bar{t}$ background uses the selection of the signal analysis with inverted b-jet veto. The number of events in the control sample is increased omitting the central jet veto requirement. Without considering pile-up effects about seven times more events in the control sample than the expected $t\bar{t}$ background contribution are expected. In the presence of pile-up this fraction decreases to about six times more $t\bar{t}$ events. Although some deviations in the event kinematics between the $t\bar{t}$ background and the control sample are observed, the shape of the $M_{\tau\tau}$ distribution is described very well.

  The contribution of other process in the control sample is estimated. Only the $Z \rightarrow \tau\tau \rightarrow \ell\ell + 4\nu$ process shows a significant contribution and leads to a distortion of the shape of the $M_{\tau\tau}$ distribution. This has to be taken into account when using the control sample.

- $Z \rightarrow \tau\tau \rightarrow \ell\ell + 4\nu$ background: The selection of the control sample to estimate the $Z \rightarrow \tau\tau \rightarrow \ell\ell + 4\nu$ background utilises $Z \rightarrow \mu\mu$ events. The muons from the $Z \rightarrow \mu\mu$ events are replaced with the decay products of τ-lepton decays from the $Z \rightarrow \tau\tau$ decay. The kinematics of the τ-leptons are given by the muons. In this way a $Z \rightarrow \tau\tau \rightarrow \ell\ell + 4\nu$ event is produced, in which only the $Z \rightarrow \tau\tau \rightarrow \ell\ell + 4\nu$ decay is produced by Monte Carlo, whereas the event remnant and the event kinematics are given by data. This method has been validated with simulated events. In the signal region $100\,\text{GeV} < M_{\tau\tau} < 150\,\text{GeV}$ the $M_{\tau\tau}$ distribution of the $Z \rightarrow \tau\tau \rightarrow \ell\ell + 4\nu$ background is predicted with an accuracy of 10%. It has been shown that the $Z \rightarrow \mu\mu$ events can be selected with a purity of 98%. Without considering pile-up effects the control sample contains about four times more events than the expected contribution of the $Z \rightarrow \tau\tau \rightarrow \ell\ell + 4\nu$ background process. In the presence of pile-up this fraction increases to about five times more events in the control sample, because different selection requirements are used.

Both methods are only used to estimate the shape of the $M_{\tau\tau}$ distribution. The normalisation of the $M_{\tau\tau}$ distribution of the $t\bar{t}$ background control sample requires a precise knowledge of the selection efficiencies of the b-jet veto and the central jet veto. Especially the determination of the efficiency of the central jet veto is difficult to estimate with simulated events and needs to be measured with data.

The normalisation of the $M_{\tau\tau}$ distribution of the $Z \rightarrow \tau\tau \rightarrow \ell\ell + 4\nu$ background control sample requires a precise knowledge of the efficiency of the $Z \rightarrow \mu\mu$ events selection as well as the selection efficiency of the signal analysis requirements.

Using these requirements to obtain a normalisation of the control samples has not yet been studied. For this reason the control samples are only used to predict the shape of the $M_{\tau\tau}$ distribution of the background processes.

Chapter 8

Discovery Potential

In this chapter, the discovery potential for a Higgs boson in the channel $H \to \tau\tau \to \ell\ell + 4\nu$ is discussed assuming a dataset that corresponds to an integrated luminosity of $30\,\text{fb}^{-1}$. In order to establish a discovery the background-only hypothesis needs to be rejected, which implies that the background must be precisely known. Background estimation methods using data have the advantage of giving a more reliable background description by avoiding systematic uncertainties, e.g. theoretical uncertainties, in the modelling of the background processes. Since the control samples contain only a finite number of events, their statistical uncertainties need to be considered. In addition, systematic effects need to be considered. To take these background uncertainties into account a statistical method based on the profile likelihood ratio is used. The signal yield is extracted by fitting the $M_{\tau\tau}$ spectrum.

This chapter starts with an overview of the statistical methods based on [1, 67]. Afterwards the systematic uncertainties and their treatment in the significance calculation are discussed. Finally the expected signal significances for a Standard Model Higgs boson are presented.

8.1 Statistical Method

8.1.1 Establishing Discovery

A discovery of a new signal process is established by rejecting the background-only hypothesis. In the statistical formalism this corresponds to a hypothesis test of the background-only hypothesis H_0.

The level of agreement between the observed data and H_0 is quantified by the so-called p-value, i.e. the probability under the assumption H_0 to find data of equal or greater incompatibility with the prediction of H_0.

In Particle Physics the p-value is expressed by means of the statistical significance Z, defined as the number of standard deviations at which a Gaussian random variable of zero mean would give a one-sided tail area equal to p. An illustration is given in Fig. 8.1. It is common to establish a discovery with a significance of $Z = 5$ which corresponds to a p-value of $p = 2.87 \times 10^{-7}$.
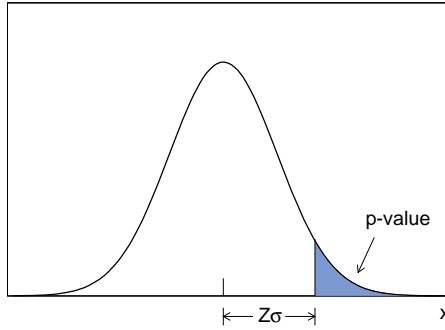
Figure 8.1: *Illustration of the correspondence between p-value and significance Z [1].*

8.1.2   Hypothesis Test

In this analysis the distribution for searching a signal is the $M_{\tau\tau}$ distribution. The shape of the background is estimated using control samples which contain only a limited number of events. The signal significance is extracted using a method based on fitting the $M_{\tau\tau}$ distribution. By simultaneously fitting the $M_{\tau\tau}$ distributions of the signal candidates and the background control samples, the background rate and shape in the signal region are constrained. In this way the statistical uncertainties of the background shapes are taken into account.

The probability density functions (pdf) used for the signal and background description are the functions used for the shape parametrisation as described in Section 6.4. That means the $Z \to \tau\tau \to \ell\ell + 4\nu$ background control sample is fitted using Equation 6.6:

$$
\begin{aligned}
PDF_Z(M_{\tau\tau}; \vec{\theta}_Z) &= F_Z(M_{\tau\tau}; m_Z, \sigma_{Z,1}, \sigma_{Z,2}, m_{Z,asym}, \sigma_{Z,asym}, f_{Z,g1}) \\
&= \left(\frac{1}{2} + \frac{1}{2} \cdot \mathrm{erf}\left(\frac{M_{\tau\tau} - m_{Z,asym}}{\sqrt{2}\sigma_{Z,asym}} \right) \right) \\
&\times \left(f_{Z,g1}\, e^{(M_{\tau\tau} - m_Z)^2 / 2\sigma_{Z,1}^2} + (1 - f_{Z,g1})\, e^{(M_{\tau\tau} - m_Z)^2 / 2\sigma_{Z,2}^2} \right).
\end{aligned}
\tag{8.1}
$$

Here $\vec{\theta}_Z$ represents the parameters $m_Z, \sigma_{Z,1}, \sigma_{Z,2}, m_{Z,asym}, \sigma_{Z,asym}, f_{Z,g1}$ which characterise the shape of the pdf.

The $t\bar{t}$ control sample contains a considerable amount of $Z \to \tau\tau$ events, see Section 7.1, whereas the contribution of the signal process to the $t\bar{t}$ control sample is small and is therefore neglected. For this reason the $M_{\tau\tau}$ distribution of the control sample is fitted by the sum of the $t\bar{t}$ parametrisation function (equation 6.7) and the $Z \to \tau\tau$ pdf:

$$
\begin{aligned}
PDF_{t\bar{t}}(M_{\tau\tau}; \vec{\theta}_{t\bar{t}}, \vec{\theta}_Z, f_{t\bar{t}}) &= f_{t\bar{t}} \cdot F_{t\bar{t}}(M_{\tau\tau}; \tau_{t\bar{t}}, \mu_{t\bar{t}}, \sigma_{t\bar{t}}) \\
&+ (1 - f_{t\bar{t}}) \cdot F_Z(M_{\tau\tau}; m_Z, \sigma_{Z,1}, \sigma_{Z,2}, m_{Z,asym}, \sigma_{Z,asym}, f_{Z,g1}) .
\end{aligned}
\tag{8.2}
$$

$(1 - f_{t\bar{t}})$ is the relative contribution of the $Z \to \tau\tau$ background in the $t\bar{t}$ control sample, $\vec{\theta}_{t\bar{t}}$ represents the parameters $\tau_{t\bar{t}}, \mu_{t\bar{t}}, \sigma_{t\bar{t}}$, see Chapter 6.4. The $Z \to \tau\tau$ background in the $t\bar{t}$

control sample is assumed to have exactly the same shape as the $Z \to \tau\tau$ control sample, which has been validated within the limited number of Monte Carlo events. For this reason the $Z \to \tau\tau$ background in the $t\bar{t}$ control sample is estimated using the $Z \to \tau\tau$ control sample, which means that the parameters $\vec{\theta}_Z$ are the same.

The $M_{\tau\tau}$ distribution of the signal candidates is fitted using the sum of the three contributions (signal, $Z \to \tau\tau$ and $t\bar{t}$):

$$
\begin{aligned}
PDF_H(M_{\tau\tau}; \vec{\theta}_H, \vec{\theta}_Z, \vec{\theta}_{t\bar{t}}, f_H, f_Z) = {} & f_H \cdot F_H(M_{\tau\tau}; m_H, \sigma_{H,1}, \sigma_{H,2}, m_{H,asym}, \sigma_{H,asym}, f_{H,g1}) \\
& + f_Z \cdot F_Z(M_{\tau\tau}; m_Z, \sigma_{Z,1}, \sigma_{Z,2}, m_{Z,asym}, \sigma_{Z,asym}, f_{Z,g1}) \\
& + (1 - f_H - f_Z) \cdot F_{t\bar{t}}(M_{\tau\tau}; \tau_{t\bar{t}}, \mu_{t\bar{t}}, \sigma_{t\bar{t}}) .
\end{aligned}
$$
(8.3)

where F_H is defined as:

$$
\begin{aligned}
PDF_H(M_{\tau\tau}; \vec{\theta}_Z) = {} & \left(\frac{1}{2} + \frac{1}{2} \cdot \mathrm{erf}\left(\frac{M_{\tau\tau} - m_{H,asym}}{\sqrt{2}\sigma_{H,asym}} \right) \right) \\
& \times \left(f_{H,g1}\, e^{(M_{\tau\tau} - m_H)^2 / 2\sigma_{H,1}^2} + (1 - f_{H,g1})\, e^{(M_{\tau\tau} - m_H)^2 / 2\sigma_{H,2}^2} \right) .
\end{aligned}
$$

$\vec{\theta}_H$ represents the parameters $m_H, \sigma_{H,1}, \sigma_{H,2}, m_{H,asym}, \sigma_{H,asym}, f_{H,g1}$ which characterise the shape of the signal pdf. The values of these parameters are given by the hypothetical signal of interest, which in the context of the Higgs boson search means the $M_{\tau\tau}$ distribution of VBF $H \to \tau\tau \to \ell\ell + 4\nu$ Monte Carlo events.

f_H and f_Z are the relative contributions of the signal and the $Z \to \tau\tau$ background processes in the $M_{\tau\tau}$ distribution of the signal candidates. f_Z and $(1 - f_Z - f_H)$ represent the normalisation of the background contribution and are determined by the fit.

The simultaneous fit of the pdfs to the data means that the likelihoods[1] of the three fits are multiplied:

$$
\begin{aligned}
L(M_{\tau\tau}|f_H, \boldsymbol{\theta}) = {} & L_Z(Z_{control}|\vec{\theta}_Z) \\
& \times L_{t\bar{t}}(t\bar{t}_{control}|\vec{\theta}_{t\bar{t}}, \vec{\theta}_Z, f_{t\bar{t}}) \\
& \times L_{s+b}(\text{signal candidates}|\vec{\theta}_H, \vec{\theta}_{t\bar{t}}, \vec{\theta}_Z, f_H, f_Z) .
\end{aligned}
$$
(8.4)

Here f_H is the parameter of interest. The others are nuisance parameters and are summarized in $\boldsymbol{\theta}$. It is important to note that some of the parameters in the likelihoods of the signal candidates are the same as in the likelihood of the control samples. In particular the parameters concerning the shape of the background are the same. Therefore the background control samples constrain these nuisance parameters.

To test the background-only hypothesis, which corresponds to $f_H = 0$, the simultaneous fit is performed twice. The ratio of the likelihoods referred to as profile likelihood ratio is used:

$$
\lambda(f_H = 0) = \frac{L(0, \hat{\hat{\boldsymbol{\theta}}})}{L(\hat{f}_H, \hat{\boldsymbol{\theta}})} .
$$
(8.5)

---

[1]The likelihood function [9] gives the probability of some observed statistically independent measurements $\mathbf{x} = (x_i, \ldots, x_N)$ to be obtained, given the theory (i.e. the pdf) $f(x, \boldsymbol{\theta})$: $L(\boldsymbol{\theta}) = \prod_{i=1}^{N} f(x_i, \boldsymbol{\theta})$.

Here $\hat{\hat{\boldsymbol{\theta}}}$ denotes the values of the nuisance parameters which maximise L under the condition $f_H = 0$. $\hat{\boldsymbol{\theta}}$ and $\hat{f}_H$ are parameters which maximise L, i.e. they are the maximum-likelihood estimators. If the data can be very well described by the H_0 hypothesis the ratio will be close to unity.

The presence of the nuisance parameters makes it more likely that the data is compatible with the H_0 hypothesis and therefore makes it more difficult to observe the signal. The constraints of the nuisance parameters by the background control samples reflect the knowledge of the background. Strong constraints show a good knowledge of the background and vice versa.

In order to judge the agreement between data and the H_0 hypothesis the p-value of the profile likelihood ratio needs to be computed. Instead of $\lambda(f_H)$ it is convenient to use the quantity q_{f_H} defined by:

$$q_{f_H} = -2 \ln \lambda(f_H) \ . \tag{8.6}$$

In the case of the Higgs boson search, the new signal is assumed to lead to a higher number of events than expected from background alone, i.e. $\hat{f}_H \geq 0$. A deviation from the background-only hypothesis with $\hat{f}_H < 0$ would not be interpreted as an observation of a new signal. For this reason in the case of a strictly positive contribution of the signal the test statistic is defined

$$q_0 = \begin{cases} -2 \ln \lambda(f_H = 0) & \hat{f}_H \geq 0 \ , \\ 0 & \hat{f}_H < 0 \ . \end{cases} \tag{8.7}$$

The p-value for an observed $q_{0,obs}$ is given by

$$p_0 = \int_{q_{0,obs}}^{\infty} f(q_0|0) dq_0 \ . \tag{8.8}$$

$f(q_0|0)$ denotes the sampling distribution of the statistic q_0 under the condition of background-only hypothesis.

8.1.3   Sampling Distribution of Likelihood Ratio

In order to find the p-value for an observed $q_{0,obs}$ the sampling distribution $f(q_0|0)$ is needed. The term $f(q_0|0)$ can be derived using ensemble tests. This means the experiment is simulated many times using generated pseudo-data. For a discovery this involves more than 10^7 pseudo-experiments which is computationally very expensive and usually can only be carried out for test cases.

Instead, based on Wilks' theorem [68], the sampling distribution can be approximated by a χ^2-distribution for one degree of freedom in the limit of a large sample size. As has been shown in [1] the sample size in the search presented here is large enough to ensure the validity of the approximation.

The requirement that a possible signal can only lead to a higher number of expected events, cf. equation 8.7, causes a slight modification of the sampling distribution. In particular one finds a mixture of a delta function at zero and a χ^2-distribution. Under the assumption that upward and downward fluctuations of the background are equally likely the significance Z of a signal can be calculated by the formula

$$Z = \sqrt{q_0} = \sqrt{-2 \ln \lambda(0)} \ . \tag{8.9}$$

The sensitivity of an experiment is its expected significance. To estimate the sensitivity the significance calculation is performed on a test sample containing the expectation values of the experiment. This data set is called *Asimov* data.

8.2   Systematic Uncertainties

The background estimation using data avoids systematic uncertainties related to detector simulation and theoretical modelling of the background processes. On the other hand the background estimation methods, presented in this thesis, are only validated within the available number of Monte Carlo events. The good agreement between the background and the control sample distributions shows that a possible systematic bias is smaller than the statistical uncertainty of the Monte Carlo samples. Since the control samples are used to estimate the shape of the background contribution, only systematic uncertainties related to the shape are important. For this reason systematic uncertainties are estimated allowing the shape to vary within its statistical uncertainty.

In the following the systematic uncertainties related to the control samples and how they are incorporated into the estimated sensitivity are discussed.

8.2.1 $Z \to \tau\tau$ Background Estimation

Since the embedding procedure involves some Monte Carlo and detector simulation related to the $Z \to \tau\tau \to \ell\ell + 4\nu$ decay, systematic uncertainties are introduced. In particular these are the energy scale and resolution of the muons and electrons from the $Z \to \tau\tau \to \ell\ell + 4\nu$ decay and their impact on the $E_\mathrm{T}^\mathrm{miss}$ measurement. The expected scales of the mis-measurements are listed in Table 8.1, they are taken from [1]. The influence of these systematic uncertainties on the analysis is studied by varying the reconstructed quantities within their expected precision. Subsequently $E_\mathrm{T}^\mathrm{miss}$ is modified accordingly.

As can be seen in Fig. 8.2 the systematic variation of the lepton energy scale and momentum resolution has almost no effect on the $M_{\tau\tau}$ distribution and for this reason is neglected.

Further systematic uncertainties arise from the fact that the kinematics of the $Z \to \tau\tau \to \ell\ell + 4\nu$ decay is created from reconstructed quantities of the $Z \to \mu\mu$ decay. Whereas the muon direction is measured with high precision, the muon energy scale and resolution as well as the reconstruction and identification efficiencies are important.

In addition, the impact of the lepton trigger used in the signal selection is not considered for the embedded $Z \to \mu\mu$ sample. As the trigger efficiencies do only weakly depend on p_T above the corresponding lepton trigger cut [1] it is assumed that the shortfall of the trigger cut is of minor importance.

The choice of the cone sizes of the embedding procedure is also a source of systematic uncertainties. In the inner cone the cells are replaced by the cells from the Monte Carlo simulation, which does not consider electronic noise and additional energy deposition due to pile-up. This should show up in the p_T and isolation distributions of the leptons. Whereas the p_T distrbutions agree quite well some deviations are observed in lepton isolation distributions, cf. Chapter 7.2.2.

Nevertheless the primary quantity to judge the performance of the method is the $M_{\tau\tau}$
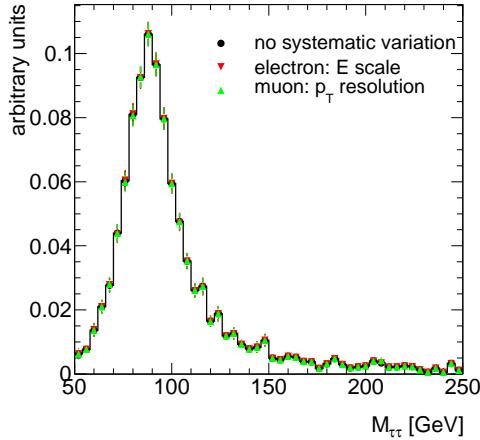
Figure 8.2: *$M_{\tau\tau}$ distributions of the $Z \to \mu\mu$ after embedding showing the impact of systematic uncertainties arising from Monte Carlo simulation. Exemplary the variation of the electron energy scale and the muon momentum resolution are shown.*

distribution. Since the $M_{\tau\tau}$ distribution predicted by the embedding method agrees very well with that of the $Z \to \tau\tau \to \ell\ell + 4\nu$ background, the impact of the discussed sources of systematic uncertainties is smaller than the statistical uncertainty. As a conservative estimate the systematic uncertainty will be estimated by the variation of the predicted $M_{\tau\tau}$ distribution within its statistical uncertainty as will be explained in Section 8.2.3.

A further source of systematic uncertainties are the cuts chosen for the $Z \to \mu\mu$ events selection. Here the by far most sensitive cut variable is the muon isolation. It has been observed that wrong settings could lead to deviations in the missing transverse energy distribution and the transverse momentum distribution of the leptons. Whereas the $M_{\tau\tau}$ distribution is mostly unaffected by the muon isolation setting it should be optimised in data using cross checks. This can be done for example using embedding of $Z \to \mu\mu$ events to mimic $Z \to ee$ events or even $Z \to \mu\mu$ events itself, cf. Chapter 7.2.4. For this reason the systematic uncertainty assigned to the $Z \to \mu\mu$ event selection is assumed to be small and therefore it is neglected.

Observable	Relative uncertainty
Electron energy scale	$\pm 1\%$
Electron energy resolution	$\sigma(E_T) \oplus 0.0073 \cdot E_T$
Muon momentum scale	$\pm 1\%$
Muon momentum resolution	$\sigma(p_\mathrm{T}) \oplus 0.011 p_\mathrm{T} \oplus 1.7 \cdot 10^{-4} p_\mathrm{T}^2$

Table 8.1: *Estimated scale of systematic mis-measurements [1].*

8.2.2 Background Estimation of the Top Quark Pair Production

Systematic uncertainties arise from the slightly different event kinematics of the control sample compared to the $t\bar{t}$ background. The difference in the event kinematics can be

caused by several effects. The dominant effect is the b-jet identification efficiency and in particular the limitation of the b-jet identification to $|\eta| < 2.5$. Second the control sample selection omits the central jet veto.

However, as the comparisons in Chapter 7.1 show these effects are small and not visible within the available number of Monte Carlo events. As a conservative estimate the systematic uncertainty is estimated by the variation of the predicted $M_{\tau\tau}$ distribution within their statistical uncertainty as explained in Section 8.2.3.

In addition, the background events in the control sample lead to a distortion of the $M_{\tau\tau}$ distribution. The distortion due to the $Z \to \tau\tau$ events are taken into account in the significance calculation. The contribution of the signal events in the $t\bar{t}$ control sample is very small and can be safely neglected.

8.2.3 Treatment of Systematic Uncertainties in the Likelihood

The general way to include systematic uncertainties into the profile likelihood formalism is to modify the model including nuisance parameters that correspond to this uncertainty. As discussed earlier only systematic uncertainties concerning the shape of the $M_{\tau\tau}$ distribution need to be considered. Since the background and the control sample distribution are in good agreement, a possible systematic bias is smaller than the statistical uncertainty of the current Monte Carlo samples. For this reason the shape is allowed to vary within its statistical uncertainty.

To include the shape uncertainty the parameters of the parametrisation function of the control sample are allowed to differ from the parameters of the parametrisation function of the corresponding background. A nuisance parameter is introduced for each parameter of the control sample. As an example, the parameter m_Z in the parametrisation function $F_Z(M_{\tau\tau}; m_Z, \sigma_{Z,1}, \sigma_{Z,2}, m_{asym}, \sigma_{asym})$ of the $Z \to \tau\tau \to \ell\ell + 4\nu$ background control sample is replaced by:

$$m'_Z = m_Z + \alpha . \tag{8.10}$$

α denotes the nuisance parameter, its nominal value is zero. The likelihood is then multiplied by a Gaussian in α centred about zero: $G(\alpha, 0, \sigma_\alpha)$. The width of the Gaussian σ_α denotes the uncertainty of the parameter m_Z. It is in this sense that the parameter m_Z is allowed to vary within its statistical uncertainty.

Extending this procedure to all parameters of the parametrisation functions of the control sample result in the likelihood:

$$L(M_{\tau\tau}|f_H, \boldsymbol{\theta}) = L_Z(Z_{control}|\vec{\theta}'_Z) \times \prod_{\alpha_i \text{ in } \vec{\alpha}_Z} G(\alpha_i, 0, \sigma_{\alpha_i})$$
$$\times L_{t\bar{t}}(t\bar{t}_{control}|\vec{\theta}'_{t\bar{t}}, \vec{\theta}_Z) \times \prod_{\alpha_j \text{ in } \vec{\alpha}_{t\bar{t}}} G(\alpha_j, 0, \sigma_{\alpha_j}) \tag{8.11}$$
$$\times L_{s+b}(\text{signal candidates}|\vec{\theta}_H, \vec{\theta}_{t\bar{t}}, \vec{\theta}_Z) .$$

Here $\vec{\theta}'_Z$ and $\vec{\theta}'_{t\bar{t}}$ denotes the parameters of the parametrisation functions of the control samples, and $\vec{\alpha}_Z$ and $\vec{\alpha}_{t\bar{t}}$ are the additional nuisance parameters to account for systematic uncertainties. The values of the width σ_{α_i} of the Gaussian $G(\alpha_i, 0, \sigma_{\alpha_i})$ are listed in

Table 8.2. They correspond to the uncertainties of the parameters of the shape parametrisation, cf. Section 6.4.

Due to the additional nuisance parameters the model gets more flexible and the background is less constrained by the control sample. This results in a lower sensitivity.

Parameter		Value of σ_{α_i}	
		without pile-up	with pile-up
$\vec{\theta}'_{t\bar{t}}$:	$\mu'_{t\bar{t}}$	7.9	12.5
	$\sigma'_{t\bar{t}}$	6.3	10
	$\tau'_{t\bar{t}}$	16	28
$\vec{\theta}'_Z$:	m'_Z	2.1	0.9
	$\sigma'_{Z,1}$	0.7	1.3
	$\sigma'_{Z,2}$	5	4.9
	$m'_{Z,asym}$	11	2.3
	$\sigma'_{Z,asym}$	7.2	2.5
	$f'_{Z,g1}$	0.037	0.07

Table 8.2: *Width σ_{α_i} of the Gaussian $G(\alpha_i, 0, \sigma_{\alpha_i})$ which is multiplied to the likelihood to account for the systematic uncertainty of the parameter i.*

8.3   Results

The signal sensitivity is based on the used Monte Carlo samples and on the expected cross sections derived after the application of the event selection, cf. Section 6.5. Uncertainties related to the modelling of the signal and background processes and on the expected cross sections are not taken into account. A incorrect modelling due to theoretical (e.g. underlying event model, cross section) or experimental (e.g. jet reconstruction efficiency) uncertainties, will lead to wrong signal sensitivities. For example:

- If the expected contribution of the $t\bar{t}$ background is estimated too small, the estimated discovery potential is too large.

- A larger signal cross section than expected results in more signal events, which means that the estimated discovery potential will be too low.

For these reasons, the expected signal significances are only valid, if the modelling of the signal and background processes, which has been used in this thesis, is valid.

The profile likelihood ratio is used to evaluate the discovery potential for Higgs boson masses M_H of $115, 120, 125, 130 \, \text{GeV}$. The selection cuts have been optimised for $M_H = 120 \, \text{GeV}$. To obtain the profile likelihood ratio a maximum likelihood fit is performed twice using the likelihood defined in equation (8.4). Once it is fitted without constraints and once with the signal normalisation constrained to zero ($f_H = 0$). In the fits the signal parameters $m_H, \sigma_{H,1}, \sigma_{H,2}, m_{H,asym}, \sigma_{H,asym}$ are fixed to the assumed signal hypothesis by fitting the signal pdf to the signal process. That means only one signal hypothesis is tested in the

fit. If the signal hypothesis is not known a priori, e.g. m_H is allowed to vary in a certain mass range, then several signal hypotheses are tested at once. In this case, the significance calculation must take into account that an excess anywhere in the mass range could lead to the rejection of the background-only hypothesis. This is commonly known as *look-elsewhere-effect* [69, 70]. To avoid these complications only fixed signal hypotheses are tested.

Figures 8.3 and 8.4 show the results of the *Asimov* data for a Higgs boson mass of $M_H = 120\,\text{GeV}$ both without and with considering systematic uncertainties without pile-up. The fitting results for all assumed Higgs boson masses are in appendix A. In the constrained fit ($f_H = 0$) it can be seen that the background shapes try to accommodate the excess at $120\,\text{GeV}$, but the background control sample prevents the variation. The incorporation of systematic uncertainties leads to a drop in signal sensitivity from 3.8σ to about 3.4σ. A comparison of Figures 8.3 and 8.4 reveals a shift of the $Z \to \tau\tau$ background pdf in the histogram of the signal candidates for the constrained fit to higher values, when systematic uncertainties are considered. This is a result of the more flexible model, which reflects the weaker constraints of the background control samples due to systematic uncertainties.

Figures 8.5 and 8.6 show the results of the *Asimov* data without and with considering systematic uncertainties with pile-up. Comparing both figures differences in the results of the constrained fit ($f_H = 0$) become visible. When considering systematic uncertainties the background model can accommodate the signal excess in the constrained fit more easily. This leads to a drop in signal sensitivity from 2.0σ to about 1.7σ.

Figure 8.7 shows the expected discovery significance depending on the assumed mass of the Higgs boson. Without pile-up the highest discovery significance is obtained at $M_H = 120\,\text{GeV}$. For higher masses the signal sensitivity decreases, because of the lower Higgs boson production cross section. For lower masses the close-by $Z \to \tau\tau \to \ell\ell + 4\nu$ peak causes the lower signal sensitivity. The incorporation of systematic uncertainties leads to a significant drop in signal sensitivity of the order of 0.4σ. The signal sensitivity at $M_H = 115\,\text{GeV}$ is more affected, because the more flexible model of the $Z \to \tau\tau \to \ell\ell + 4\nu$ background can more easily accommodate the signal excess at low masses.

The presence of pile-up results in a large drop of signal sensitivity. This is mainly caused by two effects. Even with optimized selection cuts and the use of tools like the jet vertex tool the signal selection efficiency decreases by about 20%, whereas the background rejection is almost the same. However, the dominant effect is the worse resolution of the E_T^miss reconstruction caused by pile-up. This results in much broader $M_{\tau\tau}$ distributions of the signal and the $Z \to \tau\tau \to \ell\ell + 4\nu$ background. Hence the signal peak can no longer be distinguished from the $Z \to \tau\tau \to \ell\ell + 4\nu$ peak, cf. Fig. 8.5 and Fig. 8.8.

For higher masses the separation between signal and $Z \to \tau\tau \to \ell\ell + 4\nu$ peak becomes easier, which explains the increase of the signal sensitivity at $M_H = 125\,\text{GeV}$. But, due to lower Higgs boson production cross section the signal sensitivity decreases at $M_H = 130\,\text{GeV}$.

As before the incorporation of systematic uncertainties leads to a further decrease in signal sensitivity.
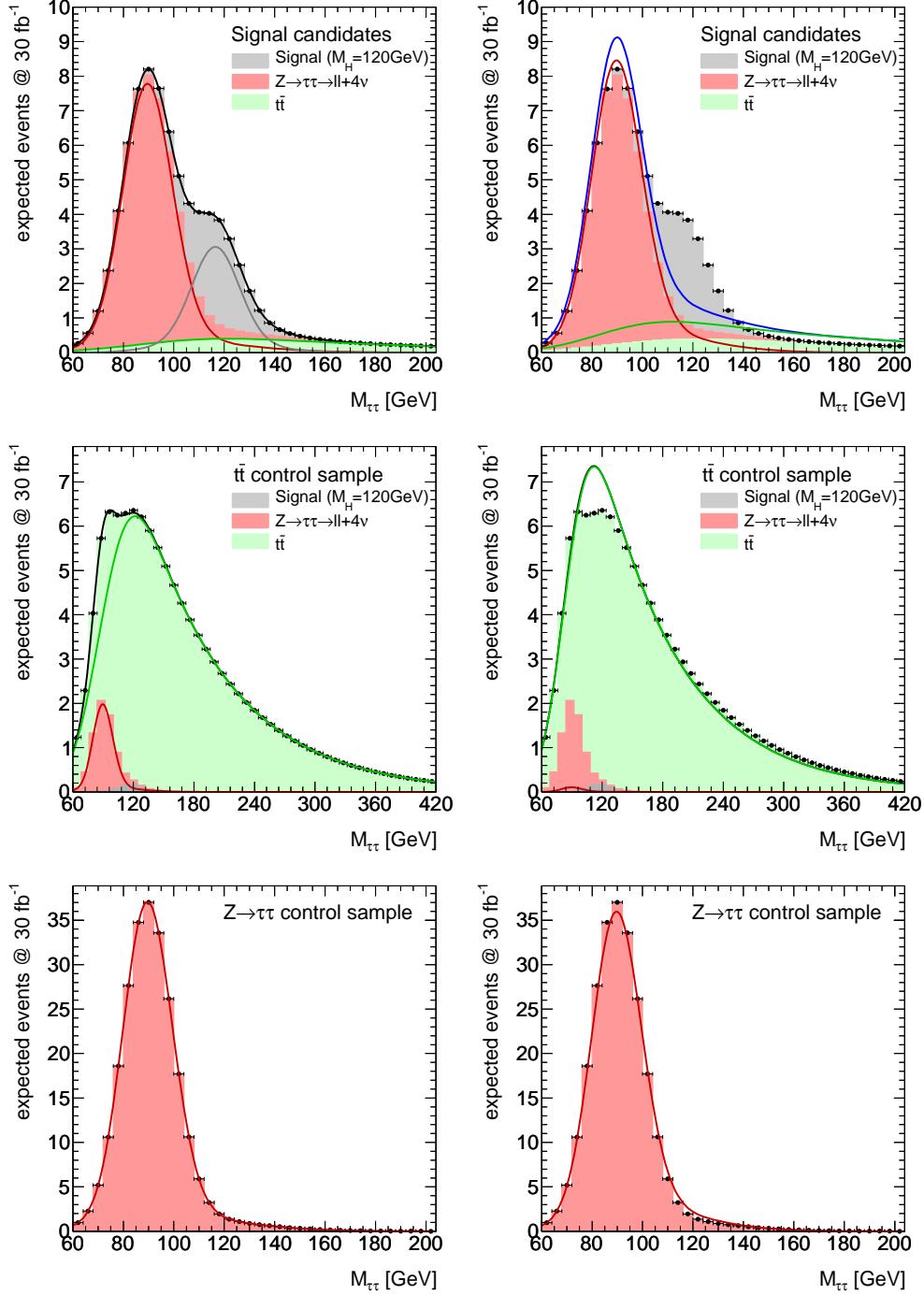
Figure 8.3: *Likelihood fit to the signal and background expectation (Asimov data) for $M_H = 120\,\mathrm{GeV}$ without pile-up. Systematic uncertainties are not considered. The signal region and background control samples are fitted simultaneously. On the left: unconstrained fit, on the right: constrained fit with $f_H = 0$. Top: signal candidates, middle: $t\bar{t}$ control sample, bottom: $Z \rightarrow \tau\tau \rightarrow \ell\ell + 4\nu$ control sample. Red line: $Z \rightarrow \tau\tau \rightarrow \ell\ell + 4\nu$ pdf, green line: $t\bar{t}$ pdf, grey line: signal pdf, black line: combined signal-plus-background pdf.*
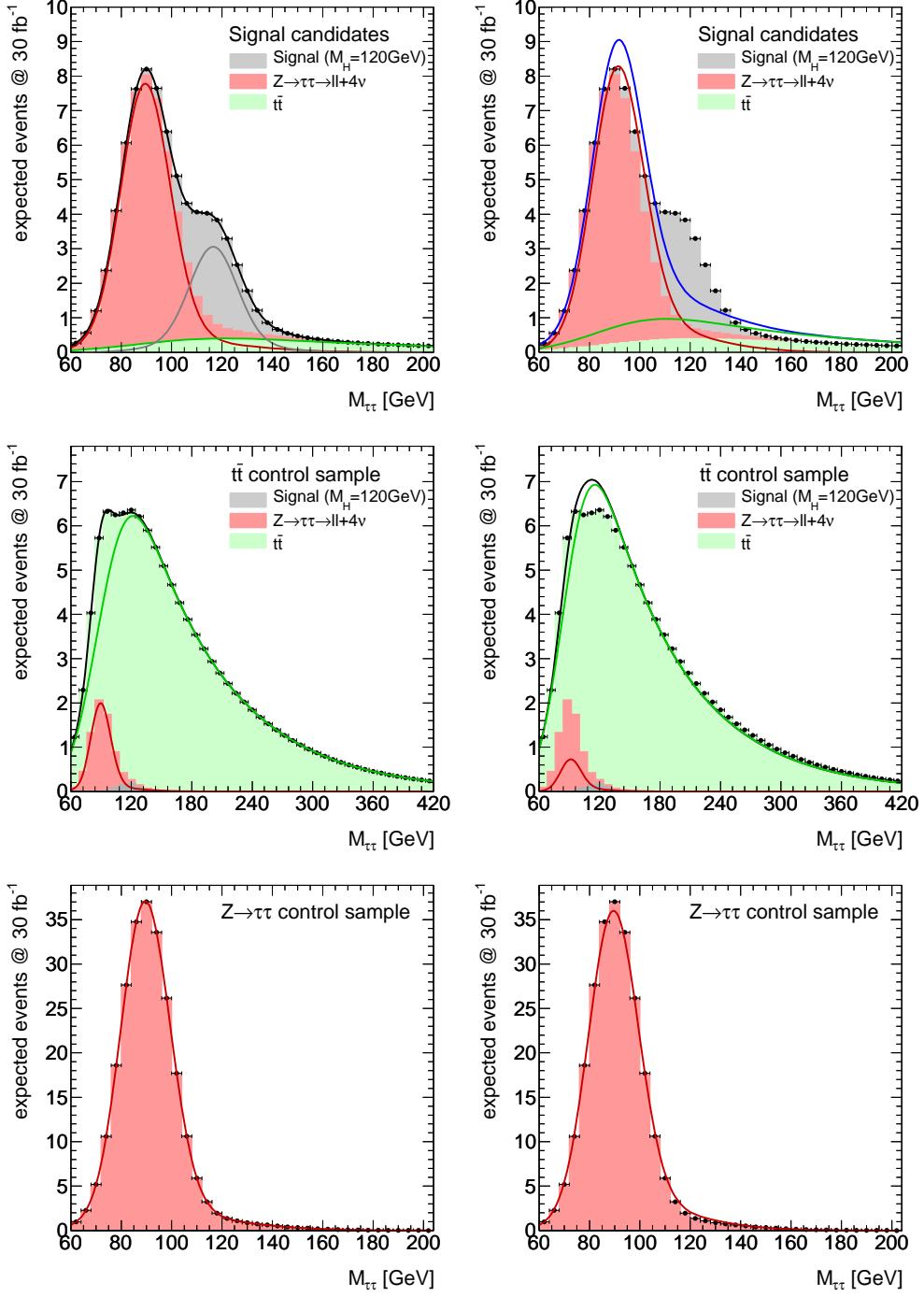
Figure 8.4: *Likelihood fit to the signal and background expectation (Asimov data) for $M_H = 120$ GeV including systematic uncertainties without pile-up. The signal region and background control samples are fitted simultaneously. On the left: unconstrained fit, on the right: constrained fit with $f_H = 0$. Top: signal candidates, middle: $t\bar{t}$ control sample, bottom: $Z \to \tau\tau \to \ell\ell + 4\nu$ control sample. Red line: $Z \to \tau\tau \to \ell\ell + 4\nu$ pdf, green line: $t\bar{t}$ pdf, grey line: signal pdf, black line: combined signal-plus-background pdf.*
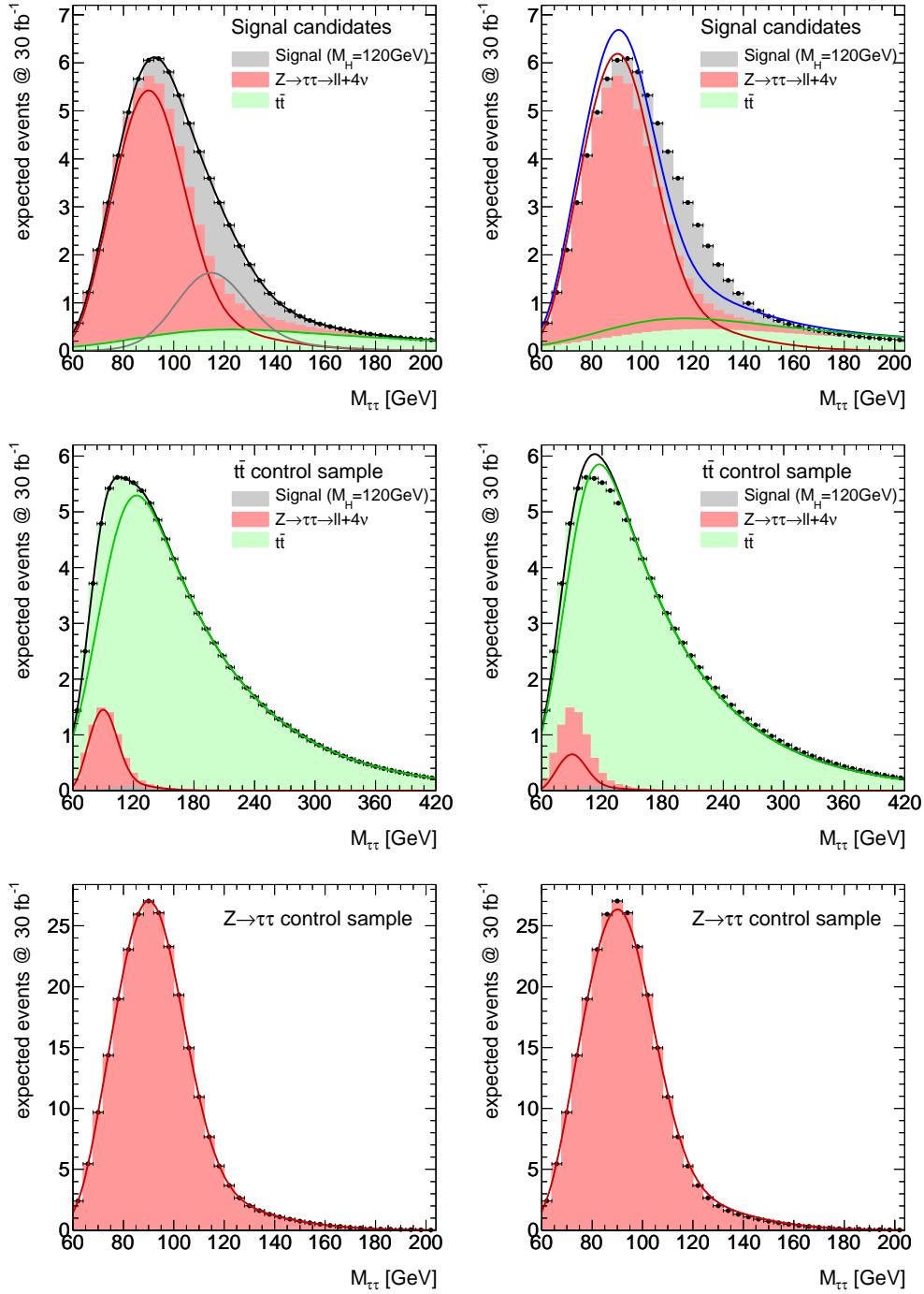
Figure 8.5: *Likelihood fit to the signal and background expectation (Asimov data) for $M_H = 120\,\text{GeV}$ with pile-up. Systematic uncertainties are not considered. The signal region and background control samples are fitted simultaneously. On the left: unconstrained fit, on the right: constrained fit with $f_H = 0$. Top: signal candidates, middle: $t\bar{t}$ control sample, bottom: $Z \to \tau\tau \to \ell\ell + 4\nu$ control sample. Red line: $Z \to \tau\tau \to \ell\ell + 4\nu$ pdf, green line: $t\bar{t}$ pdf, grey line: signal pdf, black line: combined signal-plus-background pdf.*
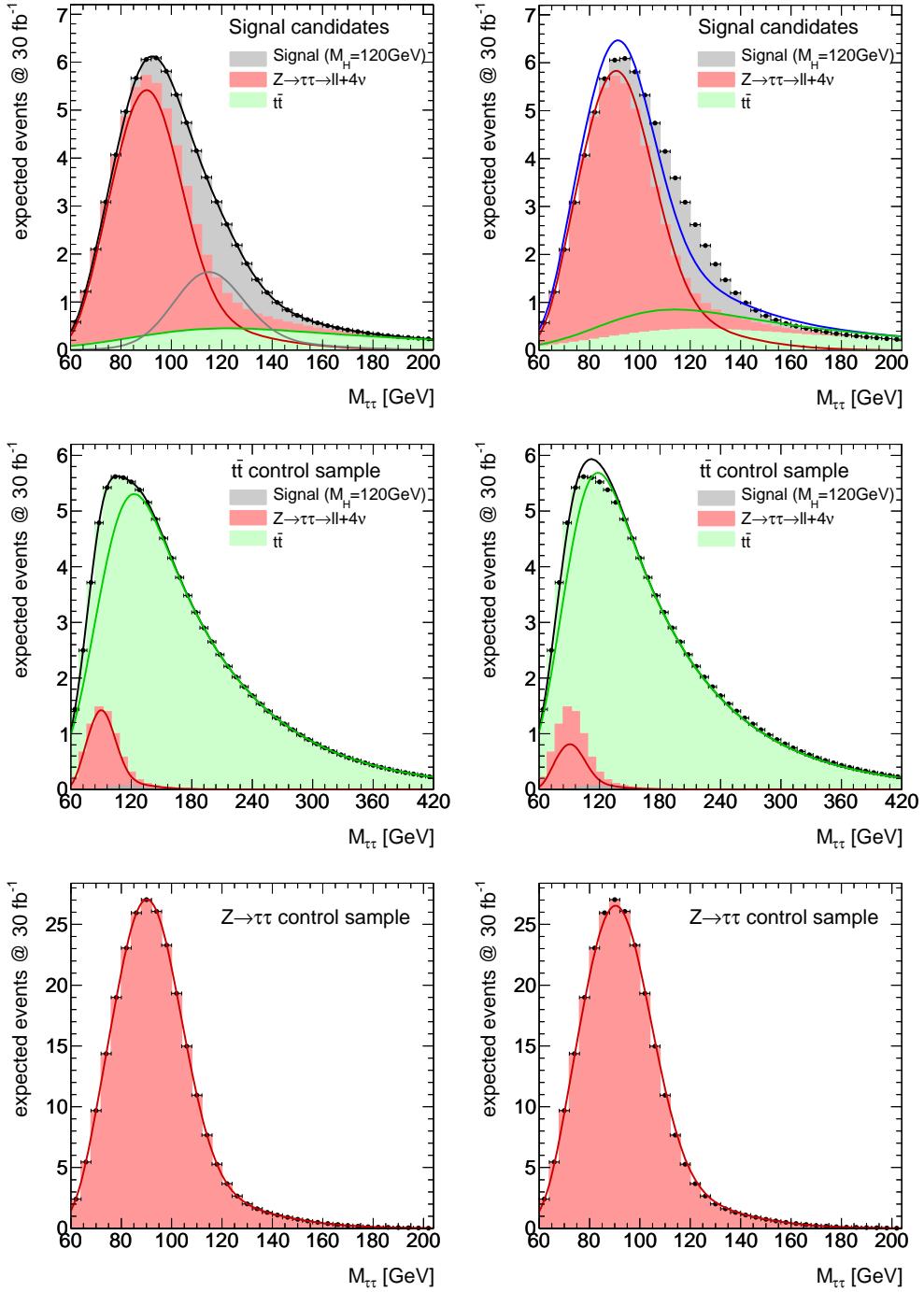
Figure 8.6: *Likelihood fit to the signal and background expectation (Asimov data) for $M_H = 120\,\text{GeV}$ including systematic with pile-up. The signal region and background control samples are fitted simultaneously. On the left: unconstrained fit, on the right: constrained fit with $f_H = 0$. Top: signal candidates, middle: $t\bar{t}$ control sample, bottom: $Z \to \tau\tau \to \ell\ell + 4\nu$ control sample. Red line: $Z \to \tau\tau \to \ell\ell + 4\nu$ pdf, green line: $t\bar{t}$ pdf, grey line: signal pdf, black line: combined signal-plus-background pdf.*
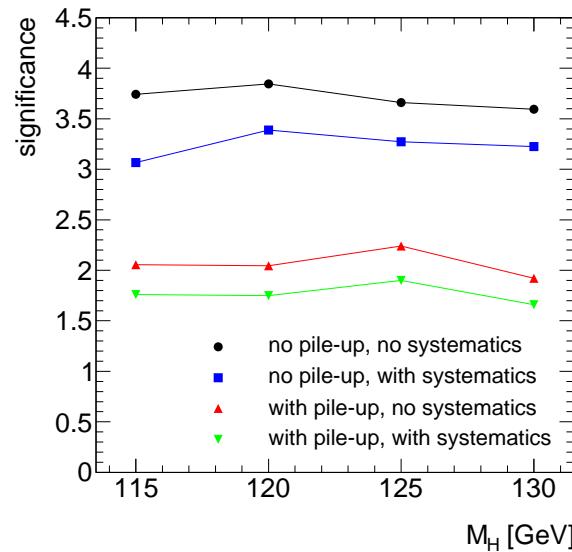
Figure 8.7: *Expected discovery significances for several assumed Higgs boson masses. The significance have been estimated with and without systematic uncertainties as well as with and without the impact of pile-up.*
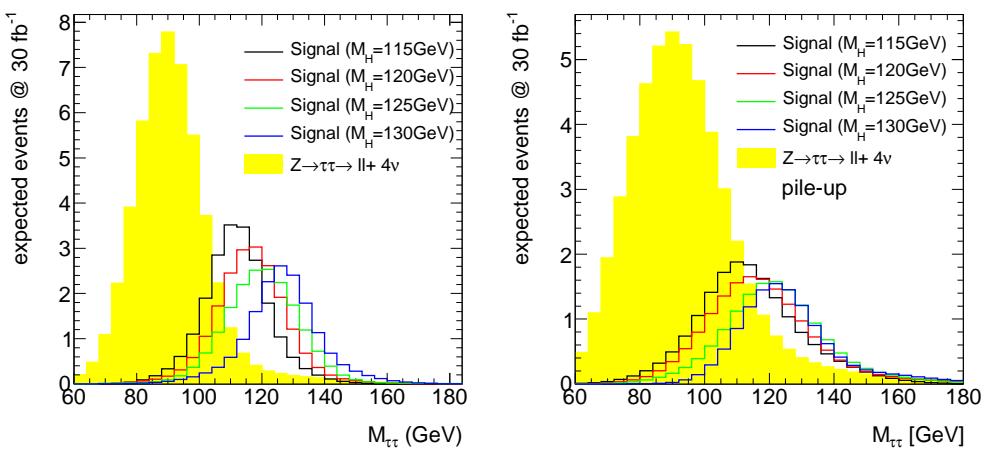
Figure 8.8: $M_{\tau\tau}$ *distribution of the* $Z \to \tau\tau \to \ell\ell + 4\nu$ *background and the signal process with several mass assumptions without and with pile-up. The distributions are normalised to the expected number of events assuming a dataset that corresponds to an integrated luminosity of* $30\,\text{fb}^{-1}$.

8.4   Discussion

The most recent results published by the ATLAS collaboration studying the discovery potential of the process VBF $H \to \tau\tau \to \ell\ell + 4\nu$ at a centre-of-mass energy of $14\,\text{TeV}$ are [1]. Neglecting the effects due to pile-up, they achieve a signal significance of about 2.5σ to 3.0σ in the mass range $115\,\text{GeV} < M_H < 130\,\text{GeV}$. By re-optimizing the selection cuts these results are improved. This has already been shown by [56], who achieved signal significance compatible with the results of this study.
In former studies the main concern about the presence of pile-up was the large increase of the number of jets, which populate the pseudo-rapidity gap between the tagging jets and spoil the central jet veto. For this reason methods, e.g. the jet vertex tool, have been developed to separate the jets generated by pile-up from jets induced by the proton-proton interaction of interest.

However this study shows that, even though these tools are used, the signal sensitivity with pile-up is still worse than without pile-up, which is mainly caused by the degradation of the resolution of the reconstructed E_T^miss.

To recover the signal sensitivity two solutions are possible:

- Improving the resolution of the $M_{\tau\tau}$ reconstruction. This has been tried using a different E_T^miss definition, namely the calculation of E_T^miss from the two leptons and the tagging jets. The calculation of E_T^miss in this way is probably subject to systematic uncertainties and needs to be validated using data. For this reason the method is neglected even though it shows small improvements. Furthermore it has been observed that in the presence of pile-up the reconstructed energy of jets is biased [71]. Adjusting the cuts applied on the calorimeter cell selection during the cluster formation remove the bias. The application of this method on a signal sample did not show any improvement of the resolution of the $M_{\tau\tau}$ or E_T^miss reconstruction. According to [72] a re-optimisation of the cell selection cuts in matter of the E_T^miss resolution could possibly gain some improvements of the resolution of the reconstructed E_T^miss.

- A calculation of the mass $M_{\tau\tau}$ that is not that much affected by pile-up could be used. Recently a new method to reconstruct the mass $M_{\tau\tau}$ has been proposed [73]. Instead of relying on the assumption of the collinear approximation additional constraints are introduced by requiring the invariant mass of the neutrinos and the lepton for each τ-lepton candidate to be consistent with the τ-lepton mass. The most probable value of $M_{\tau\tau}$ is derived by minimising a likelihood function defined in the kinematically allowed phase space.
  Using this method a large improvement of the resolution of the reconstructed mass has been demonstrated for inclusive $H \to \tau\tau$ decays. The main reason for the improvement is that the assumption of the collinear approximation is often not valid and thus has a large impact on the resolution of $M_{\tau\tau}$ reconstruction. However, in case of VBF $H \to \tau\tau$ the collinear approximation is a valid assumption and the resolution of the reconstructed mass is driven by the resolution of the E_T^miss reconstruction. For this reason only a small improvement using the new mass reconstruction method is expected.

Chapter 9

Conclusion

After a long period of development and construction the Large Hadron Collider (LHC) has started regular operation in November 2009. With the data recorded in 2010 the first Standard Model processes are observed and their properties are used to verify the performance of the detector and the Monte Carlo simulations. Now the time to probe for new Physics processes has come and the first searches for the Higgs boson in the mass range $M_H > 140\,\mathrm{GeV}$ are performed [74].

As a preparation for the search of the Higgs boson at masses $115\,\mathrm{GeV} < M_H < 130\,\mathrm{GeV}$, the presented study evaluates the expected sensitivity of the ATLAS detector to discover the Standard Model Higgs boson produced via vector boson fusion (VBF) and its decay to $H \to \tau\tau \to \ell\ell + 4\nu$. The study is based on simulated proton-proton collisions at a centre-of-mass energy of $14\,\mathrm{TeV}$.

Special emphasis is placed on the development of background estimation techniques to evaluate the dominant background processes $Z \to \tau\tau$ and $t\bar{t}$ production using data control samples.

The control sample to estimate the $t\bar{t}$ background is selected using the VBF analysis cuts with inverted b-jet veto. Although slightly different event kinematics are observed, it is shown that the control sample could be used to estimate the $t\bar{t}$ background.

The dominant background process $Z \to \tau\tau$ is estimated using $Z \to \mu\mu$ events. Replacing the muons from the $Z \to \mu\mu$ event with the decay products of simulated τ-lepton decays, $Z \to \tau\tau$ events are modelled to high precision. The kinematics of the τ-leptons are given by the muons. For the replacement of the Z boson decay products a dedicated method based on tracks and calorimeter cells is developed, validated and optimised.

A cut based event selection has been implemented to evaluate the discovery potential of the Higgs boson. The analysis is performed with and without considering pile-up effects. Higgs boson masses in the range $115\,\mathrm{GeV} < M_H < 130\,\mathrm{GeV}$ are considered. For the first time the background processes are solely estimated by background estimation techniques using data.

Without considering pile-up a signal sensitivity of 3σ to 3.4σ is achieved assuming a dataset that corresponds to an integrated luminosity of $30\,\mathrm{fb}^{-1}$. This is a significant improvement compared to the results obtained by [1].

For the first time the discovery potential is evaluated with a complete and consistent de-

scription of pile-up. Pile-up leads to an increase of the number of reconstructed jets and affects the characteristic jet signature of the signal process. In particular additional jets show up in the central region of the detector and degrade the central jet veto. With the help of inner detector tracks, jets, lying in the central region ($|\eta| < 2.5$) of the detector, are assigned to vertices. In this way jets not originating from the proton-proton interaction of interest are identified and the performance of the central jet veto is partially restored. Furthermore, pile-up produces a large increase of energy depositions in the calorimeter which degrade the resolution of the missing transverse energy reconstruction, and propagates into a degradation of the resolution of the reconstructed mass. Due to pile-up a decrease of the signal to background ratio by about 20% is observed. These effects lead to a significant decrease of the signal sensitivity to about 1.7σ to 1.9σ.

Although a loss of signal sensitivity in the presence of pile-up is not surprising, the drastic decrease is unexpected and has not been predicted by earlier studies. In future studies this can now be considered and new ways of improvement must be found.

Appendix A

# Likelihood Fits for $M_H = 115, 125, 130 \, \text{GeV}$
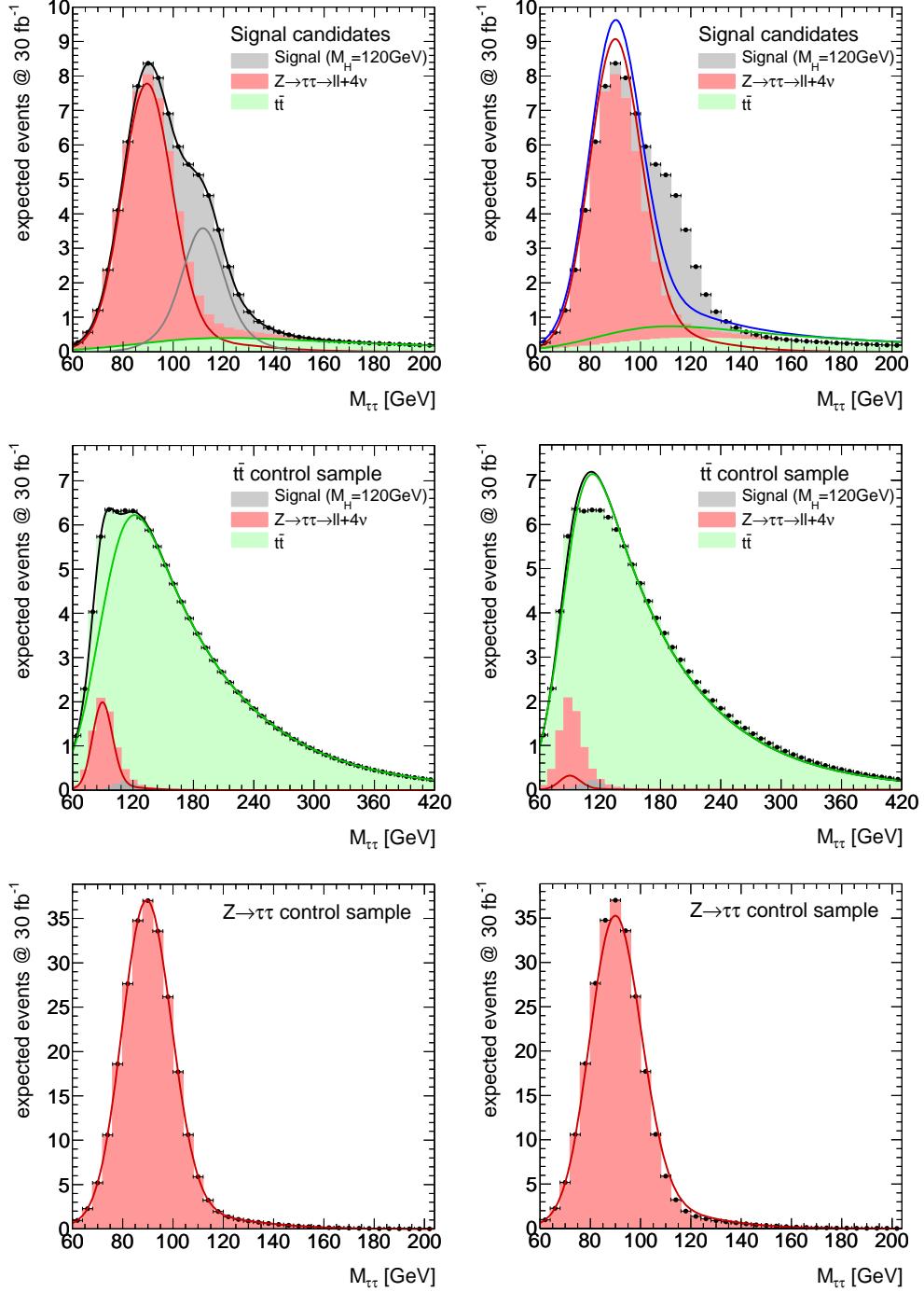
Figure A.1: *Likelihood fit to the signal and background expectation (Asimov data) for $M_H = 115\,\text{GeV}$ without pile-up. Systematic uncertainties are not considered. The signal region and background control samples are fitted simultaneously. On the left: unconstrained fit, on the right: constrained fit with $f_H = 0$. Top: signal candidates, middle: $t\bar{t}$ control sample, bottom: $Z \rightarrow \tau\tau$ control sample. Red line: $Z \rightarrow \tau\tau$ pdf, green line: $t\bar{t}$ pdf, grey line: signal pdf, black line: combined signal-plus-background pdf.*
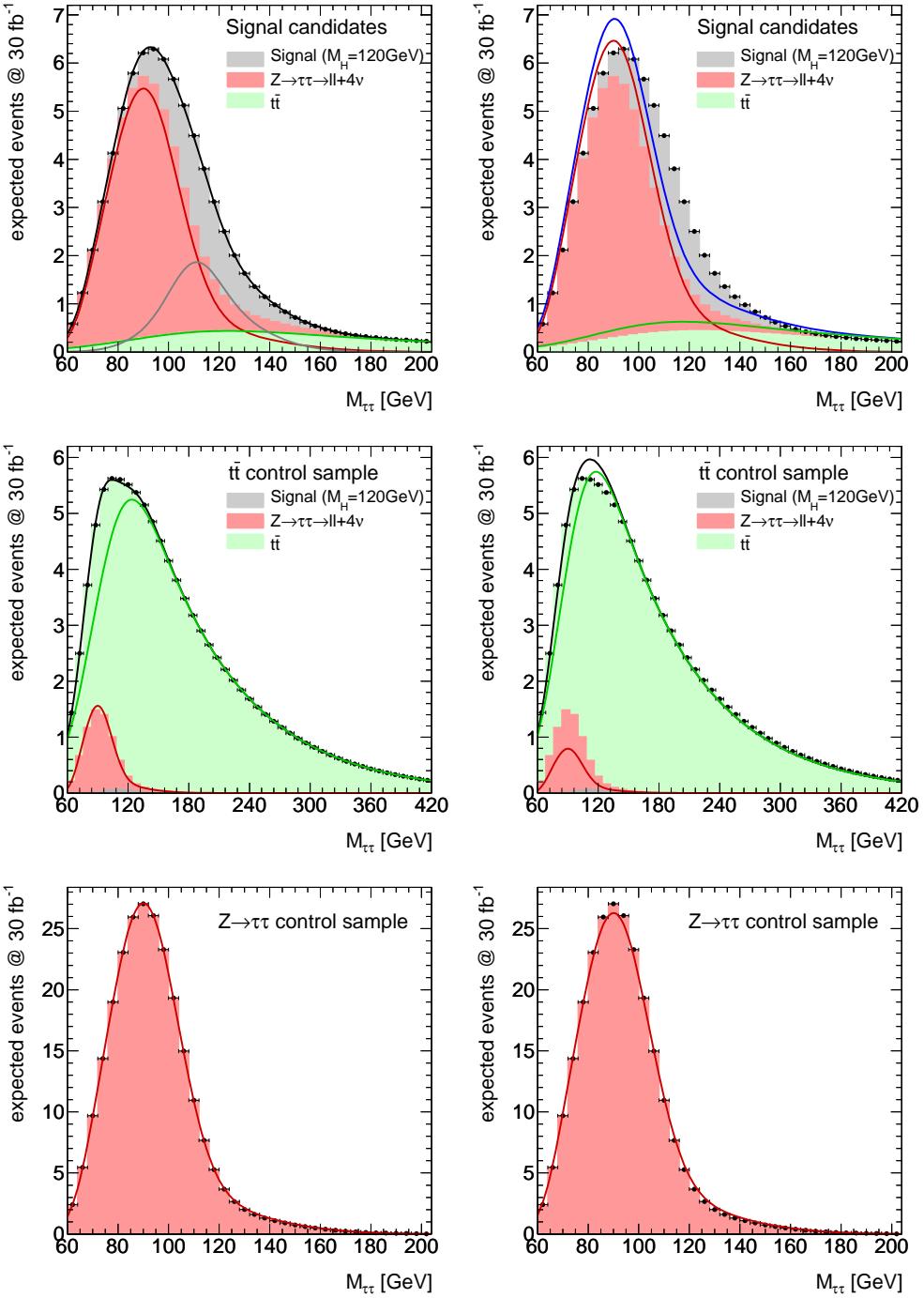
Figure A.2: *Likelihood fit to the signal and background expectation (Asimov data) for $M_H = 115\,\mathrm{GeV}$ with pile-up. Systematic uncertainties are not considered. The signal region and background control samples are fitted simultaneously. On the left: unconstrained fit, on the right: constrained fit with $f_H = 0$. Top: signal candidates, middle: $t\bar{t}$ control sample, bottom: $Z \to \tau\tau$ control sample. Red line: $Z \to \tau\tau$ pdf, green line: $t\bar{t}$ pdf, grey line: signal pdf, black line: combined signal-plus-background pdf.*
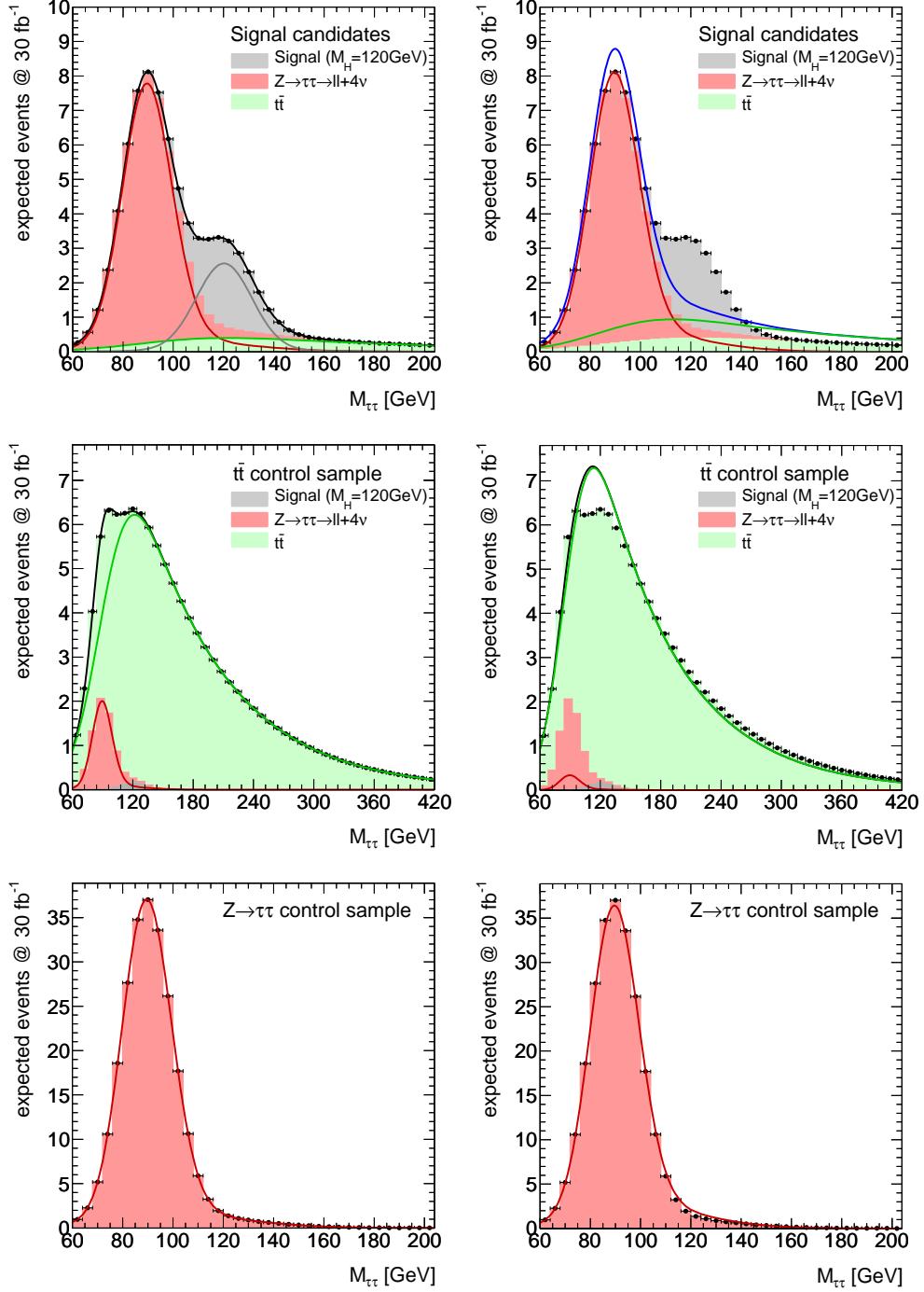
Figure A.3: *Likelihood fit to the signal and background expectation (Asimov data) for $M_H = 125\,\text{GeV}$ without pile-up. Systematic uncertainties are not considered. The signal region and background control samples are fitted simultaneously. On the left: unconstrained fit, on the right: constrained fit with $f_H = 0$. Top: signal candidates, middle: $t\bar{t}$ control sample, bottom: $Z \to \tau\tau$ control sample. Red line: $Z \to \tau\tau$ pdf, green line: $t\bar{t}$ pdf, grey line: signal pdf, black line: combined signal-plus-background pdf.*
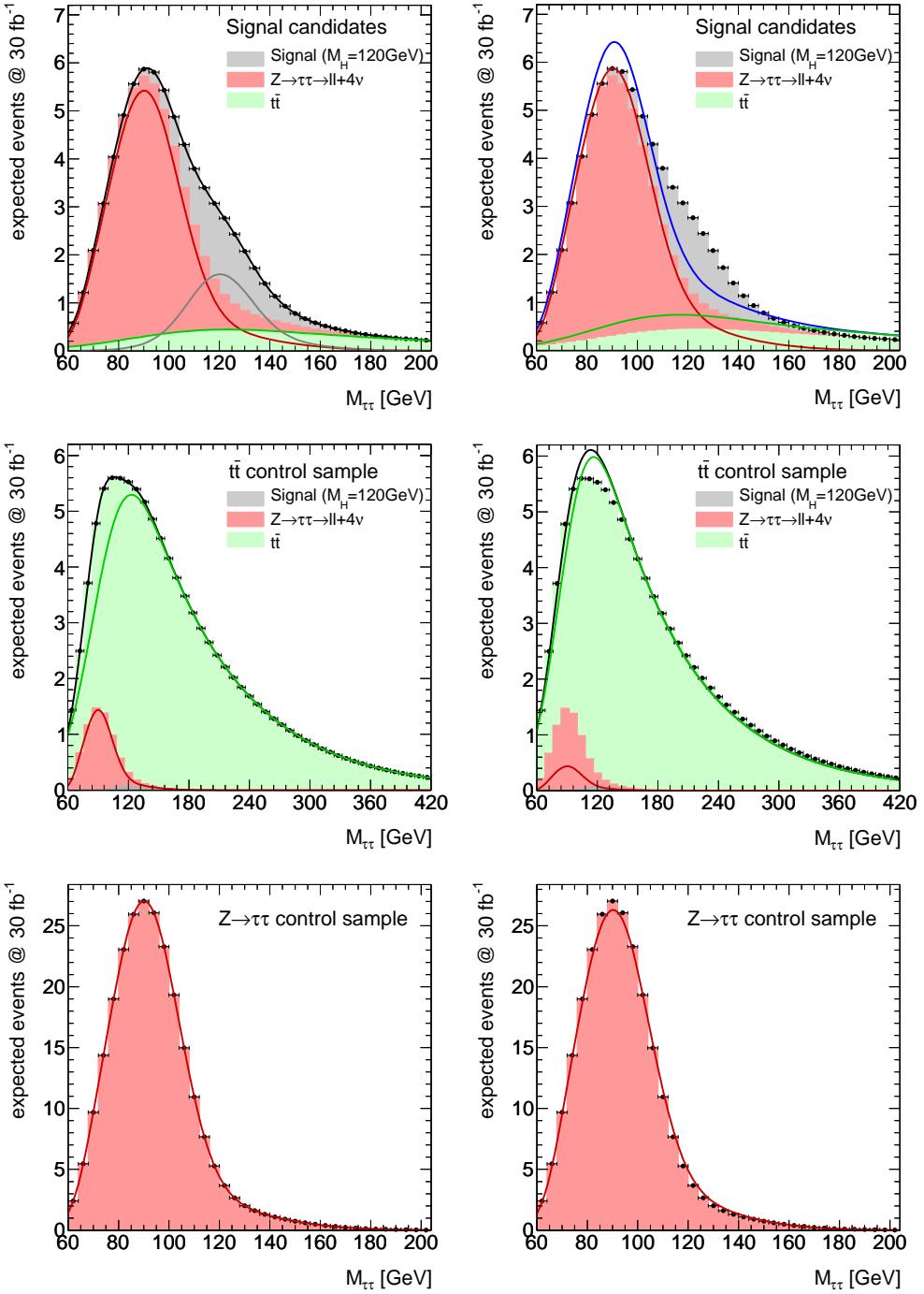
Figure A.4: *Likelihood fit to the signal and background expectation (Asimov data) for $M_H = 125$ GeV with pile-up. Systematic uncertainties are not considered. The signal region and background control samples are fitted simultaneously. On the left: unconstrained fit, on the right: constrained fit with $f_H = 0$. Top: signal candidates, middle: $t\bar{t}$ control sample, bottom: $Z \to \tau\tau$ control sample. Red line: $Z \to \tau\tau$ pdf, green line: $t\bar{t}$ pdf, grey line: signal pdf, black line: combined signal-plus-background pdf.*
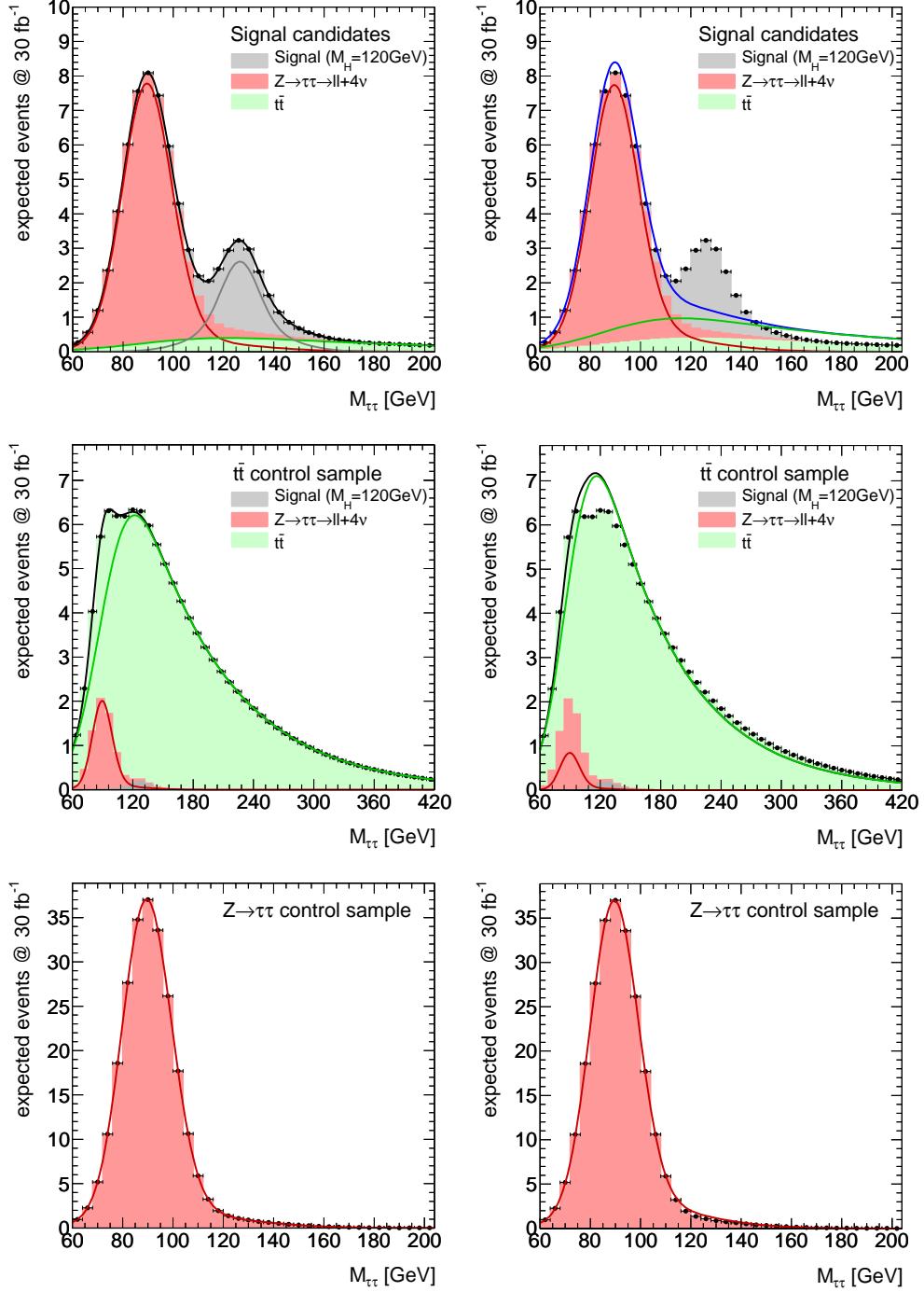
Figure A.5: *Likelihood fit to the signal and background expectation (Asimov data) for $M_H = 130\,\mathrm{GeV}$ without pile-up. Systematic uncertainties are not considered. The signal region and background control samples are fitted simultaneously. On the left: unconstrained fit, on the right: constrained fit with $f_H = 0$. Top: signal candidates, middle: $t\bar{t}$ control sample, bottom: $Z \to \tau\tau$ control sample. Red line: $Z \to \tau\tau$ pdf, green line: $t\bar{t}$ pdf, grey line: signal pdf, black line: combined signal-plus-background pdf.*
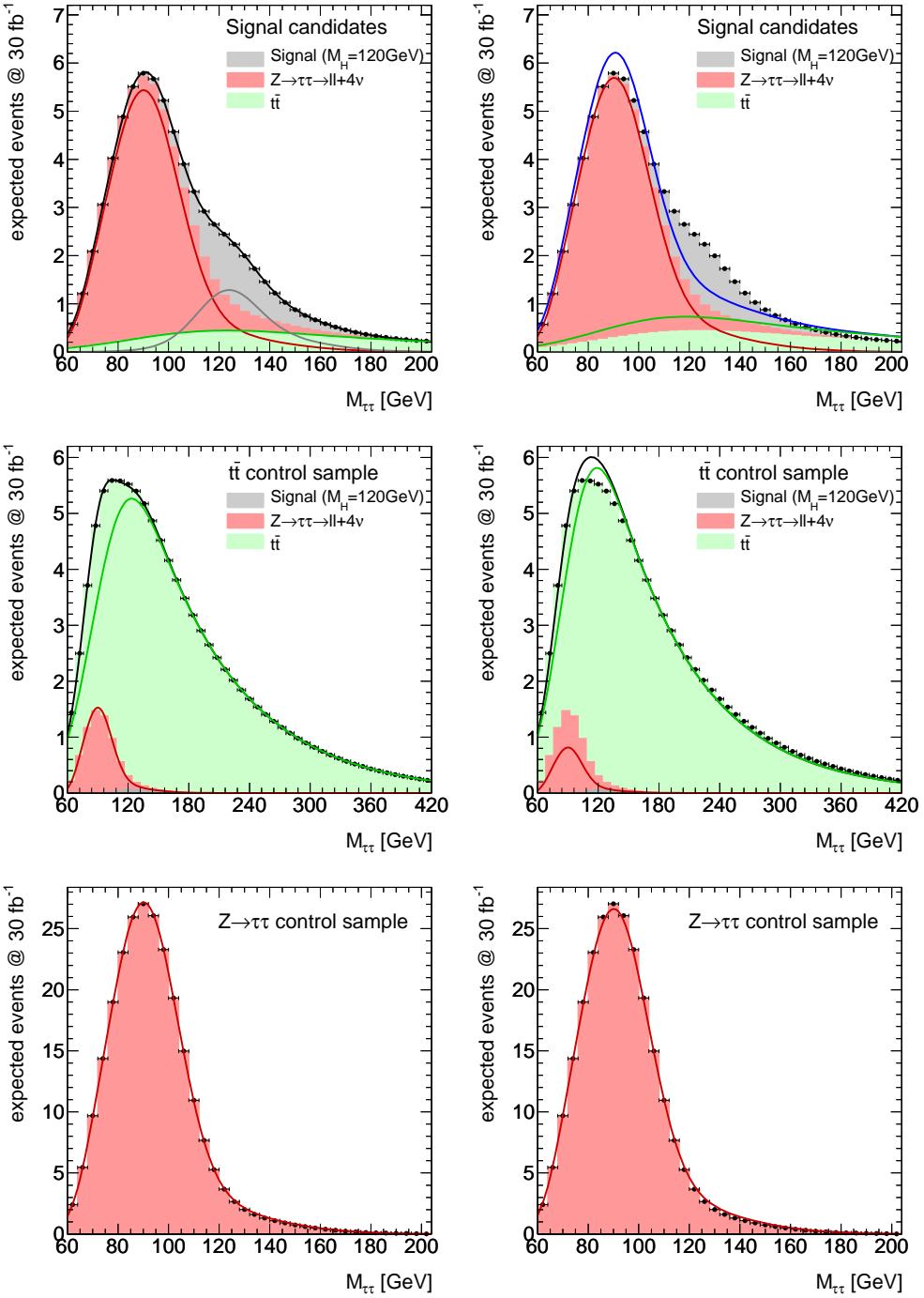
Figure A.6: *Likelihood fit to the signal and background expectation (Asimov data) for $M_H = 130\,\mathrm{GeV}$ with pile-up. Systematic uncertainties are not considered. The signal region and background control samples are fitted simultaneously. On the left: unconstrained fit, on the right: constrained fit with $f_H = 0$. Top: signal candidates, middle: $t\bar{t}$ control sample, bottom: $Z \to \tau\tau$ control sample. Red line: $Z \to \tau\tau$ pdf, green line: $t\bar{t}$ pdf, grey line: signal pdf, black line: combined signal-plus-background pdf.*

Bibliography

[1] G. Aad et al. [ATLAS Collaboration], Expected performance of the ATLAS experiment: detector, trigger and physics, CERN, Geneva 2009.

[2] S. L. Glashow, Nucl. Phys. **22** (1961) 579–588.

[3] S. Weinberg, Phys. Rev. Lett. **19** (1967) 1264–1266.

[4] A. Salam, in Elementary Particle Theory, (Almqvist and Wiksell, Stockholm, 1968).

[5] F. Halzen and A. D. Martin, Quarks and Leptons: An Introductory Course in Modern Particle Physics, (John Wiley & Sons Inc., 1984).

[6] M. Herrero, The Standard model, arXiv:hep-ph/9812242.

[7] G. 't Hooft, Nuclear Physics B **33** (1971) 173 – 199.

[8] G. 't Hooft, Nuclear Physics B **35** (1971) 167 – 188.

[9] K. Nakamura et al. (Particle Data Group), J. Phys. **G 37** (2010) 075021.

[10] P. W. Higgs, Phys. Lett. **12** (1964) 132–133.

[11] G. S. Guralnik, C. R. Hagen and T. W. B. Kibble, Phys. Rev. Lett. **13** (1964) 585–587.

[12] P. W. Higgs, Phys. Rev. **145** (1966) 1156–1163.

[13] J. Goldstone, Nuovo Cim. **19** (1961) 154–164.

[14] J. Goldstone, A. Salam and S. Weinberg, Phys. Rev. **127** (1962) 965–970.

[15] M. Spira and Peter M. Zerwas, Lect. Notes Phys. **512** (1998) 161–225.

[16] B. W. Lee, C. Quigg and H. B. Thacker, Phys. Rev. D **16** (1977) 1519–1531.

[17] R. Barate et al., Phys. Lett. **B565** (2003) 61–75.

[18] F. Abe et al., Nucl. Instr. Meth. **A271** (1988) 387–403.

[19] V. M. Abazov et al. [D0 Collaboration], Nucl. Instrum. Meth. **565** (2006) 463–537.

[20] CDF and D0 Collaboration, Combined CDF and D0 Upper Limits on Standard Model Higgs- Boson Production with up to 6.7 fb^{-1} of Data, arXiv:1007.4587 [hep-ex].

[21] The LEP Electroweak Working Group, http://lepewwg.web.cern.ch/LEPEWWG.

[22] S. Dittmaier et al., Handbook of LHC Higgs Cross Sections: 1. Inclusive Observables, arXiv:1101.0593 [hep-ph].

[23] L. Evans and P. Bryant, Journal of Instrumentation **3** (2008) S08001.

[24] ATLAS Collaboration, JINST **3** (2008) S08003.

[25] P. Giubellino et al. [ALICE Collaboration], Nucl. Instrum. Meth. **A344** (1994) 27–38.

[26] ATLAS Collaboration, ATLAS detector and physics performance: Technical Design Report, 1, (CERN, Geneva, 1999), Electronic version not available.

[27] CMS Collaboration, The CMS experiment at the CERN LHC, JINST 3 (2008) S08004.

[28] S. Amato et al. [LHCb Collaboration], LHCb technical proposal, CERN-LHCC-98-04.

[29] N. Andari et al., Higgs Production Cross Sections and Decay Branching Ratios, Internal Report ATL-PHYS-INT-2010-030, CERN, Geneva, Mar 2010.

[30] A. Djouadi, J. Kalinowski and M. Spira, Comput. Phys. Commun. **108** (1998) 56–74.

[31] A. Bredenstein, A. Denner, S. Dittmaier and M. M. Weber, Precision calculations for H -> WW/ZZ -> 4fermions with PROPHECY4f, arXiv:0708.4123 [hep-ph].

[32] U. Aglietti, R. Bonciani, G. Degrassi and A. Vicini, Physics Letters B **595** (2004) 432–441.

[33] G. Marchesini and B. R. Webber, Nucl. Phys. **B 310** (1988) 461.

[34] S. Jadach et al., Comput. Phys. Commun. **76** (1993) 361.

[35] Z. Was and E. Baberio, Comput. Phys. Commun. **79** (1994) 291.

[36] S. Asai et al., Cross sections for Standard Model processes to be used in the ATLAS CSC notes, Internal Report ATL-PHYS-INT-2009-003, ATL-COM-PHYS-2008-077, CERN, Geneva, May 2008.

[37] K. Melnikov and F. Petriello, Phys. Rev. Lett. **96** (2006) 231803.

[38] K. Melnikov and F. Petriello, Phys. Rev. **D74** (2006) 114017.

[39] T. Gleisberg, S. Höche, F. Krauss, A. Schaelicke, S. Schumann and J. Winter, J. High Energy Phys. **02** (2003) 056. 28 p.

[40] M. L. Mangano et al., J. High Energy Phys. **07** (2003) 001.

[41] M.L. Mangano, Exploring theoretical systematics in the ME-to-shower MC merging for multijet processm in Proceedings of Matrix Element/Monte Carlo Tuning Workshop, Fermilab, Nov. 15, 2002.

[42] J. M. Butterworth, J. R. Forshaw and M. H. Seymour, Z. Phys. **C72** (1996) 637–646.

[43] A. Schälicke, F. Krauss, R. Kuhn and G. Soff, JHEP **12** (2002) 013.

[44] S. Catani, F. Krauss, R. Kuhn and B. R. Webber, JHEP **11** (2001) 063.

[45] D. Adams et al., The ATLFAST-II performance in release 14 -particle signatures and selected benchmark processes-, Internal Report ATL-PHYS-INT-2009-110, CERN, Geneva, Dec 2009.

[46] R. Bonciani, S. Catani, M. L. Mangano, and P. Nason, Nucl. Phys. **B529** (1998) 424450.

[47] S. Frixione and B.R. Webber, JHEP **06** (2002) 029.

[48] S. Agostinelli et al., Nuclear Instruments and Methods in Physics Research Section A: Accelerators, Spectrometers, Detectors and Associated Equipment **506** (2003) 250–303.

[49] T. Sjostrand, S. Mrenna and P. Skands, JHEP **05** (2006) 026.

[50] W. Lampl et al., Calorimeter Clustering Algorithms: Description and Performance, Internal Report ATL-LARG-PUB-2008-002, ATL-COM-LARG-2008-003, CERN, Geneva, Apr 2008.

[51] S. Hassani et al., Nucl. Instrum. Meth. **A572** (2007) 77–79.

[52] G. C. Blazey et al., Run II jet physics, arXiv:hep-ex/0005012.

[53] I. Abt et al., Nucl. Instrum. Meth. **A386** (1997) 348–396.

[54] M. Lehmacher, b-Tagging Algorithms and their Performance at ATLAS, Internal Report ATL-PHYS-PROC-2008-052, ATL-COM-PHYS-2008-152, CERN, Geneva, Jul 2008.

[55] I. Rottländer, Studie zum Entdeckungspotential für ein Higgs-Boson aus Vektorbosonfusion mit leptonischem Zerfall für das ATLAS-Experiment am LHC, Diploma thesis, BONN-IB-2005-03.

[56] M. Groh, H. Kroha and S. Horvat, Study of the Higgs Boson Discovery Potential in the Process $pp \to Hqq, H \to \tau^+\tau^-$ with the ATLAS Detector, Ph.D. thesis, TU Munich, 2009.

[57] R.K. Ellis, I. Hinchliffe, M. Soldate and J.J. van der Bij, Nucl. Phys. **B297** (1988) 221.

[58] C. Ruwiedel, G. Gaycken and J. Kroseberg, Study of the Use of Jet-Vertex Association for the Suppression of Pileup Jets in the Central Jet Veto in VBF $H \to \tau^+\tau^- \to lh$, Internal Report ATL-PHYS-INT-2009-069, CERN, Geneva, Jul 2009.

[59] H. Nilsen, W/Z+Jets and W/Z+Heavy Flavor Jets at the Tevatron, arXiv:0906.0229 [hep-ex].

[60] C. Stute, Entwicklung einer Methode zur Abschätzung des Untergrundes der Topquark-Paarproduktion aus Daten für die Higgs-Suche im Kanal Vektorbosunfusion $H \to \tau\tau$, Master's thesis, University of Siegen, 2008.

[61] N. Möser, M. Schmitz, J. Kroseberg, M. Schumacher and N Wermes, Estimation of $Z \to \tau\tau$ Background in VBF $H \to \tau\tau$ Searches from $Z \to \mu\mu$ Data using an Embedding Technique, Internal Report ATL-PHYS-INT-2009-109, CERN, Geneva, Dec 2009.

[62] C. Isaksson, M. Flechl, N. Möser and M. Schmitz, Embedding Technique for the ttbar Background Estimation in Charged Higgs Boson Searches, Internal Report ATL-PHYS-INT-2010-041, CERN, Geneva, Apr 2010.

[63] T. Sjöstrand et al., CERN 89-08 **3** (1989) 143.

[64] M. Aharrouche et al., Nucl. Inst. Meth. **A 597** (2008) 178 – 188.

[65] K. A. Assamagan et al., Final report of the ATLAS AOD/ESD Definition Task Force, Internal Report ATL-SOFT-2004-006. ATL-COM-SOFT-2004-008. CERN-ATL-COM-SOFT-2004-008, CERN, Geneva, 2004.

[66] Talk by Thomas Schwindt, m-tautau Helmholtz Alliance Working Group Meeting, (3. Dec. 2010).

[67] G. Cowan, K. Cranmer, E. Gross and O. Vitells, Asymptotic formulae for likelihood-based tests of new physics, arXiv:1007.1727 [physics.data-an].

[68] S. S. Wilks, Ann. Math. Statist. **9** (1938) 60–62.

[69] L. Lyons, The Annals of Applied Statistics **Vol. 2, No. 3** (2008) 887–915.

[70] E. Gross and O. Vitells, Trial factors for the look elsewhere effect in high energy physics, arXiv:1005.1891v3 [physics.data-an].

[71] C. Ruwiedel, J. Kroseberg and N. Wermes, Formation of topological clusters in the presence of pileup using asymmetric cuts, Internal Report ATL-COM-PHYS-2009-556, CERN, Geneva, Oct 2009.

[72] C. Ruwiedel, personal communication.

[73] A. Elagin, P. Murat, A. Pranko and A. Safonov, A New Mass Reconstruction Technique for Resonances Decaying to di-tau, arXiv:1012.4686 [hep-ex].

[74] G. Aad et al. [ATLAS Collaboration], Higgs Boson Searches using the $H \to WW^{(*)} \to \ell\nu\ell\nu$ Decay Mode with the ATLAS Detector at 7 TeV, Internal Report ATLAS-CONF-2011-005, CERN, Geneva, Feb 2011.

Danksagung